Demonstrating High Transformer Ratio Beam-Driven Plasma Wakefield Acceleration

Dissertation

Zur Erlangung des Doktorgrades
des Fachbereiches Physik der Fakultät
für Mathematik, Informatik und Naturwissenschaften
der Universität Hamburg

Vorgelegt von

Gregor Loisch

Hamburg

2019

Gutachter/-innen der Dissertation:	Prof. Dr. Florian Grüner Dr. Anne Oppelt Prof. Dr. Massimo Ferrario
Zusammensetzung der Prüfungskommission:	Prof. Dr. Sven-Olaf Moch Prof. Dr. Florian Grüner Prof. Dr. Wolfgang Hillert Dr. Reinhard Brinkmann Dr. Anne Oppelt
Vorsitzender der Prüfungskommission:	Prof. Dr. Sven-Olaf Moch
Datum der Disputation:	02.09.2019
Vorsitzender des Fach- Promotionsausschussess PHYSIK:	Prof. Dr. Michael Potthoff
Leiter des Fachbereichs PHYSIK:	Prof. Dr. Wolfgang Hansen
Dekan der Fakultät MIN:	Prof. Dr. Heinrich Graener

„Vordenken ist besser als Nachdenken.“

— *C. T.*

Abstract

In this work, plasma wakefield acceleration with high transformer ratios, i.e. high ratios between acceleration of witness particles to deceleration of driver particles, is investigated experimentally.
Particle-beam-driven plasma wakefield acceleration (PWFA) is one of the prime candidates for future compact accelerator technologies. In this scheme, a high-brightness driver particle bunch enters a plasma and initiates oscillations of plasma electrons by expelling them from their equilibrium positions. Particles trailing the driver bunch can be accelerated in the electric field between regions of negative and positive charge excess formed in this oscillation. Acceleration gradients of up to several tens of GV/m have been demonstrated in experiment, exceeding the gradients of conventional technology by orders of magnitude. PWFA could thus allow to accordingly shrink the size of an accelerator, possibly reducing size and cost of an accelerator facility significantly.
One key aspect of a PWFA is the ratio between acceleration gradient behind the driver and deceleration gradient inside the driver bunch. This so-called transformer ratio defines the maximum acceleration achievable for a given driver energy and is closely connected to the achievable efficiency. In linear wakefield theory the transformer ratio is limited to 2 for longitudinally symmetric driver bunches, which typically emerge from conventional accelerators. One proposed method to achieve high transformer ratios (HTR) exceeding this limit is to employ driver bunches with lengths of multiple plasma skin depths and sawtooth-like, "triangular" current profiles. Due to the complexity of shaping such bunches and beam-plasma instabilities that can inhibit stable acceleration, HTRs had thus far not been achieved in PWFA.
In the course of the present work, the driving of HTR PWFA has been accomplished at the **P**hoto-**I**njector **T**est facility at DESY in **Z**euthen (PITZ). Existing bunch shaping capabilities at PITZ, based on photocathode laser pulse shaping, were extended to the production of HTR-capable driver bunches. An argon gas discharge plasma cell was built and optimised for providing the plasma acceleration medium for the PITZ electron beam parameters. A novel plasma density measurement method based on the self-modulation of long electron bunches was developed and validated, which enabled determination of plasma densities not accessible with established methods. Following these preparations, a transformer ratio of $4.6^{+2.2}_{-0.7}$ was observed experimentally and reproduced in numerical simulations.

Zusammenfassung

In dieser Arbeit wird die Beschleunigung von Elektronen in teilchenstrahlgetriebenen Plasmawellen (engl. *plasma wakefield acceleration*, PWFA) mit hohem Transformationsverhältnis, also hohem Verhältnis von Beschleunigung des Nutzstrahls zu Abbremsung des Treiberstrahls, experimentell untersucht.
PWFA ist eine der vielversprechendsten Technologien für zukünftige, kompakte Teilchenbeschleuniger. Hierbei erzeugt ein relativistisches Treiber-Teilchenpaket mit hoher Ladungsdichte bei Eintritt in das Plasma-Beschleunigungsmedium eine Oszillation der Plasmaelektronen. Zwischen den Bereichen mit positivem und negativem Ladungsüberschuss, die in diesen Oszillationen erzeugt werden, bestehen elektrische Felder, in denen nachfolgende (Nutz-)Teilchen beschleunigt werden können. Beschleunigungsfelder von mehreren 10 GV/m wurden experimentell nachgewiesen, was die Felder in konventionellen Beschleunigern um mehrere Größenordnungen übertrifft. Dies würde es erlauben die Beschleunigungsstrecke, die für eine bestimmte Endenergie des Nutzstrahls benötigt wird, und damit auch die Maße und Kosten einer Beschleunigeranlage, signifikant zu reduzieren.
Einer der wichtigsten Parameter von PWFA ist das Verhältnis von Beschleunigung des Nutzstrahls zu Abbremsung des Treiberstrahls. Dieses sogenannte Transformationsverhältnis bestimmt den maximalen Energiegewinn eines Nutzstrahls für gegebene Treiberstrahlenergien. Für konventionelle, longitudinal symmetrische Treiberstrahlen ist das Transformationsverhältnis in linearen Plasmawellen auf 2 begrenzt. Eine Methode um hohe Transformationsverhältnisse, also Werte über 2, zu erreichen besteht darin Treiberpakete mit einem dreieckförmigen Stromverlauf zu verwenden. Aufgrund der schwierigen Erzeugung derartiger Teilchenpakete und der Instabilitäten, denen sie beim Treiben von Plasmawellen unterliegen, konnten bisher keine hohen Transformationsverhältnisse experimentell nachgewiesen werden.
Im Rahmen dieser Arbeit wurden die Möglichkeiten zur Formung von Elektronenpaketen am Photoinjektor Teststand am DESY Standort Zeuthen (PITZ) auf die Erzeugung von dreieckförmigen Treiberpaketen erweitert. Eine Gasentladungsplasmazelle, die Beschleunigungsmedien für die Elektronenstrahlparameter von PITZ bereitstellt wurde entwickelt und optimiert. Basierend auf der Selbstmodulation langer Elektronenpakete in Plasmen wurde eine Methode zur Bestimmung der Plasmadichte in der Zelle entwickelt, welche die Messung von Dichten außerhalb des Messbereichs etablierter Methoden ermöglichte. Anschließend konnten erstmalig Plasmawellen mit einem Transformationsverhältnis von $4.6^{+2.2}_{-0.7}$ experimentell gemessen und in numerischen Simulationen reproduziert werden.

Contents

Part I

Plasma wakefield acceleration

In the following chapters the theoretical basis of the plasma wakefield accelerator and the acceleration of particle bunches in such wakefields with high transformer ratios, as well as the theoretical basis for the practical realisation of it will be described.
After a brief introduction to the applications of high brightness, high energy electron beams and the limits of state-of-the-art acceleration technology in Ch. 1, the concept of plasma wakefield acceleration, linear wakefield theory, the transformer ratio and methods to increase the transformer ratio are discussed in Chs. 2 and 3.
Section 4.1 is devoted to the instabilities that can appear in plasma wakefield acceleration, which would prevent stable operation of a high transformer ratio plasma wakefield accelerator.
The nonlinear regime of plasma wakefield acceleration is introduced in Sec. 4.2 and ways of mitigation of the instabilities are lined out.
Finally, Ch. 5 reviews the numerical simulation tools, which were used to understand in detail the dynamics of high transformer ratio plasma wakefield acceleration in general and particularly for the beam parameters of the PITZ facility.

Chapter 1

Conventional electron accelerators

Particle accelerators are a vital tool for studies in various fields of research and industry. To understand the need for novel accelerator technologies, first applications of high-energy and high-brightness electron accelerators as well as the limits of currently used acceleration technologies shall be introduced.

1.1 Synchrotron radiation sources

After the prediction [1] and first observation [2] of radiation from particles bent in the magnetic fields of an accelerator, synchrotron radiation has become one of the main diagnostics tools in various fields of science. Photons with wavelengths ranging from the Terahertz (THz) to the hard X-ray spectrum are facilitated for research in material and life sciences, biology, chemistry, plasma physics and others.
The radiation results from acceleration of charged particles. At rest and in uniform motion, the electric field of a charged particle is also at rest in a co-moving frame of reference. In case of an accelerated movement, the electric fields are changed and the information of that change spreads from the position of the particle with the (finite) speed of light. This distortion of the electromagnetic fields traveling with the speed of light is a photon, the wavelength of which depends on the acceleration of the source charge.
Today's synchrotron radiation sources exploit this effect for the production of short-pulse, tunable wavelength and high-intensity synchrotron radiation by acceleration of particles traveling with relativistic velocities transverse

to their direction of motion. Transverse acceleration is usually achieved by sending the particles through a magnetic dipole field, where they experience a transverse Lorentz-force

$$\mathbf{F} = q(\mathbf{E} + \mathbf{v} \times \mathbf{B}) \ , \tag{1.1}$$

with the particle's charge q, $\mathbf{E}$ the external electric field (which is equal to zero in the case of a purely magnetic bend), $\mathbf{v}$ the particle's velocity and $\mathbf{B}$ the externally applied magnetic flux. The total amount of power radiated in such a motion is expressed by [3]

$$P = \frac{q^4}{6\pi\epsilon_0 m^4 c^5} \mathcal{E}^2 B^2 \ , \tag{1.2}$$

where m is the mass of the radiating particle, $\mathcal{E}$ its energy, B the flux of the magnetic field, in which the particle is bent, ϵ_0 the vacuum permittivity and c the speed of light in vacuum. Due to the quadruple dependence on the particle's mass and their easy production, electron beams are usually used to produce synchrotron radiation.

The majority of synchrotron radiation sources is based on electron storage rings. Such facilities usually consist of an electron source, a linear accelerator (linac), possibly a synchrotron booster to increase the electron energies to the required level and an electron storage ring, at which the experimental stations are placed. The storage ring mainly consists of dipole magnets, which bend the beam to the circular beamline trajectory, higher-order magnetic devices (quadrupole, sextupole) for e.g. beam focusing or corrections, accelerating structures, which are used to compensate the loss of particle energy due to the emitted synchrotron radiation, and insertion devices like e.g. undulators, which force the particle beam on periodic, slalom-like trajectories, on which it radiates synchrotron radiation with tunable properties.

While this is the layout of most synchrotron radiation sources, machines of the so-called 4th generation are based on a linac only. A linac allows the production of electron beams of high brightness, i.e. high particle number per time, per energy, per area and per solid angle. Such bright, dense electron beams are sent to undulator magnet sections to emit synchrotron radiation in the so-called free-electron laser (FEL) process [4]. In such an FEL, the emission of electromagnetic radiation is coherent. This leads to a change of the intensity of the emitted radiation I from $I \sim N$ to $I \sim N^2$, with N the number of emitting electrons. Thus, the intensity of the emitted light is orders of magnitude higher than from storage-ring-based sources.

The drawback of such a machine is the limitation for the beam to pass the acceleration devices (as well as the undulator radiation section) only once before being dumped.
For synchrotron radiation at X-ray wavelengths (i.e. $\leq 10\,\mathrm{nm}$, $E_{ph} \geq 100\,\mathrm{eV}$) usually electron energies on the order of GeV are needed.

1.2 High energy physics

High energy particle physics is another field of application for high energy electron accelerators. In such accelerators particles are accelerated to very high energies and then either collided with counter-propagating particles or with fixed targets, to investigate fundamental particle physics processes. Research in modern particle physics demands for beam energies of several hundred GeV up to TeV. To efficiently reach such high energies, circular accelerators like synchrotrons would usually be employed, which allow to reuse the accelerating structures at every circulation of the particles. For electrons and positrons the maximum energy reachable in such circular machines is limited by the emission of synchrotron radiation, though, as described by Eq. (1.2). The particle energies in the Large Electron Positron collider (LEP), which was operated by the European Organization for Nuclear Research (CERN), were e.g. limited to below 105 GeV (maximum centre of mass collision energy $\sqrt{s} = 209\,\mathrm{GeV}$), even though as many acceleration structures as mechanically possible were fitted into the 27 km circumference synchrotron. Due to this limitation future electron positron colliders are proposed to be based on linear accelerators [5, 6] as circular machines can hardly reach centre of mass collision energies in the TeV range even with considerably larger circumference [7].

1.3 Radiofrequency acceleration

Acceleration of charged particles is based on the Lorentz-force [Eq. (1.1)] that particles experience when passing through an electric field. Generally an accelerating structure consists of two metal plates with central apertures, between which a high voltage U is applied. The resulting field between the plates is used for acceleration. As illustrated in Fig. 1.1 a), particles with charge Q pass through the apertures and are accelerated by $Q \cdot U$. The first particle accelerators were based on direct current (DC) high voltage generators. Among these were e.g. the "Cockcroft-Walton" [8] and the "Van de

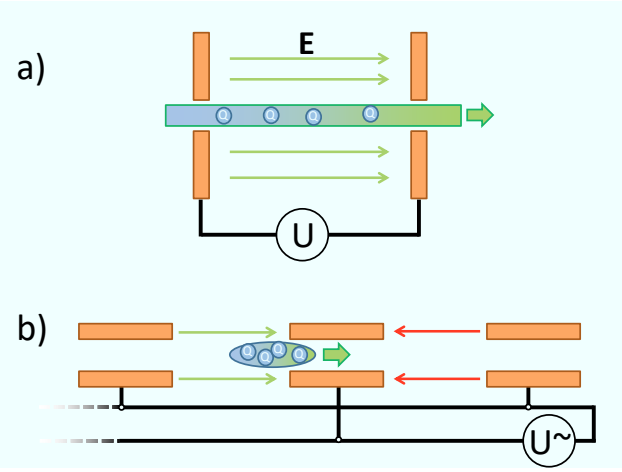

Figure 1.1: Illustration of particle acceleration in a DC voltage U (a) and an AC voltage U ∼ (b). Single particles with charge Q are accelerated in a constant stream (a) or in compressed particle bunches (b) in the electric field E, which in case (b) has accelerating phases (thin green arrows) and decelerating phases (red arrows).

Graaff" generator [9]. Particle energies of several MeV were reached with such accelerators.

As the DC high voltage is limited by electrical breakdown in the generators, the transmission lines between accelerator and generator and in the accelerating structure itself, a new technology was necessary to reach even higher particle energies. To circumvent the technical issues of high DC voltages, acceleration by alternating current (AC) radiofrequency (RF) voltages was introduced [10, 11]. In this scheme particles are passing e.g. through a series of hollow tubes, which shield the AC electric fields. The RF acceleration voltage is applied between these tubes and is experienced by the particles when they enter the drift space between two tubes. At correct timing, particles are inside the tubes during the voltage being decelerating and in between the tubes during the accelerating phases of the AC voltage. To allow for such a timing for all particles, they are compressed longitudinally to discrete packages, the so-called bunches. Depending on the type of particles and accelerator, the number of particles in such a bunch can range from several thousand to more than 10^{10} and the length can range from a few micrometer up to several centimeters. The concept is illustrated in Fig. 1.1 b).

Due to the changing sign of the accelerating voltage, arcs between the electrodes are less likely to develop, allowing much higher accelerating fields than at DC voltages. Additional advantages are the possibility to efficiently

generate high amplitude RF voltages in electron amplifier tubes (so called "klystrons") and amplification of the accelerating voltage by resonantly driving the AC voltage in the acceleration cavities. The latter is achieved by employing hollow metal structures, the inner surfaces of which form oscillatory electrical circuits. When the resonance frequency of this circuit matches the input RF frequency the fields in the cavity are amplified by resonant excitation. As in such cavities the phase velocity of the accelerating fields is zero (i.e. the extrema are always at the same positions within the structure) such cavities are called *standing wave* cavities. In the so-called *travelling wave* cavities the phase velocity of the accelerating fields matches the velocity of the accelerated particles which are thus experiencing a constant phase of the field during the whole acceleration process. Various different geometries exist for both types of cavities and modern acceleration structures are capable of supplying acceleration fields up to 100 MV/m [5, 12]. To allow for high accelerating fields and to reduce the scattering of beam particles due to collisions with residual gas particles, accelerators are usually operated under ultra high vacuum (UHV) conditions.

1.4 Linear beam dynamics

Besides the accelerating structures, additional beamline devices are essential for the operation of an accelerator to manipulate the particle beams. These include dipole magnets to bend beams, small dipoles for beam position correction (steerer magnets), quadrupole magnets to focus the beam and others. To describe the dynamics of the particles in these beamline elements, linear matrix theory is usually used. Even though this does not include nonlinear effects such as the space charge forces between the particles in a bunch, linear theory is useful to e.g. roughly optimise beam transport. It is especially applicable at high particle energies, when space charge forces between the beam particles are mostly compensated by the magnetic fields induced by the current of the beam itself. Due to the physical and mathematical similarities to the description of transport of light rays in linear optics, particle beam dynamics and the devices to manipulate the beam are also often referred to as beam optics. In the following, linear dynamics of single particles will be described, before collective parameters, which summarise the dynamics of entire particle bunches, will be introduced and examined.

1.4.1 Single particle linear dynamics

The movement of a particle is generally described by its 6D phase space (position and momentum) or trace space (position and divergence) positions. Physical particle position in three dimensions and the corresponding angular directions of motion, i.e. divergences, allow to locate a particle and to calculate its trajectory at any point of time [3, 13–16]. We will here mainly follow the notation of Wille [3].
Particle positions are given in the xyz-coordinate system. The origin of the coordinates is the position of the ideal trajectory through the accelerator beamline. This is defined by the design trajectory of a virtual reference particle through every beamline element. The longitudinal coordinate z describes the offset of a particle from ideal in the direction of acceleration, i.e. the main direction of particle movement. Horizontal and vertical offsets x and y from the reference trajectory, respectively. The divergences are described by $x' = \mathrm{d}x/\mathrm{d}z = p_x/p_z$, $y' = \mathrm{d}y/\mathrm{d}z = p_y/p_z$ and $\Delta p/p_{ref}$, with Δp the deviation of the particle's momentum p from the momentum of the reference particle p_{ref}.
As longitudinal dynamics do not play a major role in the linear accelerators of interest for this work (negligible longitudinal drift due to highly relativistic energies and no consideration of e.g. bunch compression), the linear beam optics is reduced to the 5D space of the two transverse dimensions plus the longitudinal divergence. The acceleration process at the particle source, in which (in the present work) the longitudinal dynamics mostly take place, is calculated numerically as described in Ch. 5.
A particle is thus represented by its trace space vector

$$\mathbf{X} = \begin{pmatrix} x \\ x' \\ y \\ y' \\ \frac{\Delta p}{p_{ref}} \end{pmatrix}. \tag{1.3}$$

To calculate the particle's trace space vector after a beamline section or element like a drift, the particle vector is multiplied with the corresponding transfer matrices M: $\mathbf{X} = M \cdot \mathbf{X_0}$. The transfer matrix of e.g. a drift of length

d is given by

$$M_{drift} = \begin{pmatrix} 1 & d & 0 & 0 & 0 \\ 0 & 1 & 0 & 0 & 0 \\ 0 & 0 & 1 & d & 0 \\ 0 & 0 & 0 & 1 & 0 \\ 0 & 0 & 0 & 0 & 1 \end{pmatrix} , \tag{1.4}$$

and of a horizontally focusing quadrupole of length l and magnetic gradient G by

$$Mquad = \begin{pmatrix} \cos\Omega & \frac{1}{\sqrt{|k|}}\sin\Omega & 0 & 0 & 0 \\ -\sqrt{|k|}\sin\Omega & \cos\Omega & 0 & 0 & 0 \\ 0 & 0 & \cosh\Omega & \frac{1}{\sqrt{|k|}\sinh\Omega} & 0 \\ 0 & 0 & \sqrt{|k|}\sinh\Omega & \cosh\Omega & 0 \\ 0 & 0 & 0 & 0 & 1 \end{pmatrix} , \tag{1.5}$$

where $k = \frac{e}{p_{ref}+\Delta p}G$ and $\Omega = \sqrt{|k|}l$.

1.4.2 Linear collective dynamics

When an assembly of beam particles (e.g. a particle bunch) is described, it is impractical to analytically calculate the vector for every particle. Instead, the shape of the area in the trace space, in which the described particles are distributed, is described by collective parameters. In an ideal case (Gaussian bunch distribution), the area occupied by the particles is elliptic. The parameters ϵ, α, β and γ, that are commonly used to describe the shape of these ellipses, are called Twiss-parameters [17] or also Courant-Snyder-parameters [18] and their definition is illustrated in Fig. 1.2.

The geometrically defined emittance in x-direction ϵ_x of a particle distribution is calculated by

$$\epsilon_x = \sqrt{\langle x^2\rangle\langle x'^2\rangle - \langle xx'\rangle^2} , \tag{1.6}$$

and analogously for the y-direction. To account for the change of the divergence (e.g. $x' = \frac{p_x}{p_z}$) at increasing longitudinal momentum during acceleration, the so-called normalised emittance

$$\epsilon_{x,n} = \beta_b\gamma_b\sqrt{\langle x^2\rangle\langle x'^2\rangle - \langle xx'\rangle^2}. \tag{1.7}$$

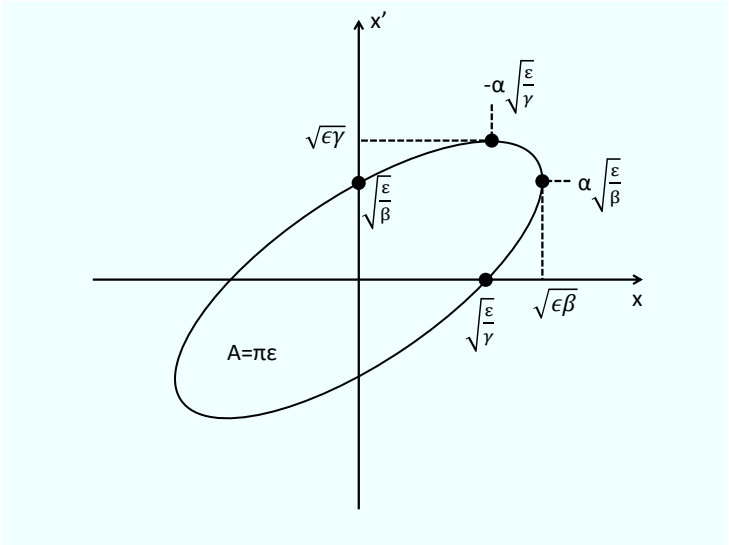

Figure 1.2: Exemplary illustration of the elliptic trace space area A occupied by an ideal (Gaussian) particle bunch and the definitions of the Twiss-parameters to describe it (cf. [3]).

is often employed, where $\beta_b = v/c$ and $\gamma_b = \frac{1}{\sqrt{1-\beta_b^2}}$ are the ratio of beam particle velocity v to speed of light c and the relativistic Lorentz-factor of a particle, respectively. The other Twiss-parameters are related to the emittance via

$$\beta = \frac{\sigma^2}{\epsilon} \,, \tag{1.8}$$

$$\alpha = -\frac{\beta'}{2} \,, \tag{1.9}$$

$$\gamma = \frac{1+\alpha^2}{\beta} \,, \tag{1.10}$$

where σ is the root-mean-square (RMS) size of the particle distribution in the considered plane and β' the derivative of β with respect to z.
Matrix optics can now be defined to propagate the Twiss-parameters through linear beamline optics, similar to the single-particle dynamics described in Sec. 1.4.1. For any linear manipulation of the trace space of a particle distribution and in general for any manipulation by a conservative force, the volume occupied by this distribution in the 6-dimensional trace space is constant, as asserted by the *Liouville's theorem* [19, 20].

1.5 High-gradient acceleration

In linear accelerators, the major part of the accelerator length is occupied by acceleration sections. The amplitude of the acceleration field (i.e. accelerating gradient) determines how much energy change a charged particle experiences per unit length. Therefore, the length of the accelerating structures to reach a certain particle energy, that is needed for an application, and thus the facility size, depends directly on the acceleration gradient. As stated in Sec. 1.3, the gradient of today's accelerating structures is limited. This is mainly due to electric vacuum breakdown in the metal cavities.
The high electric surface fields (especially at micro-protrusions/micro-tips on the surface, where the field can be enhanced even more) lead to field emission of electrons from the metal surfaces of the cavity walls. Those emitted electrons, which are accelerated into the beamline, are referred to as dark current and lead to increased radiation levels and potentially heating of surfaces at small apertures. If the current density of emitted electrons is sufficiently high to locally heat the surface at the emission point to high temperatures, thermal emission also starts to supply electrons. Adhered residual gas particles are set free from the hot surface and can be ionised in collisions. The charged particles, that are not accelerated into the beamline hit the metallic surfaces of the cavity, where they can cause secondary particle emission and surface heating on impact. When the temperature at particle emission points locally surpasses the melting point of the cavity metal surface, metal ions can be evaporated and a metal vapour arc can form between differently charged surfaces of the cavity [21–23]. As such an arc is electrically conducting, it changes the current distribution and thus the resonance conditions and field distribution in the accelerating cavity. In such a case most of the incoming RF power is reflected by the accelerating cavity and no defined (i.e. stable) acceleration of particles is possible anymore. Furthermore, the surfaces of the cavity can be damaged by the arc discharge if too much material is evaporated.
The formation of discharges is hindered by the usage of RF voltages, as mentioned in Sec. 1.3. Also reducing the duration of the applied RF voltage by using short pulses of RF power decreases the likelihood of breakdown as well as the average deposited heat on the cavity surfaces (and thus necessary cooling power). Above 100 MV/m the discharge forms such quickly though, that even the utilisation of nanosecond pulses at RF frequencies of up to several 10 GHz does not prevent breakdown sufficiently.

1.6 Novel particle accelerators

The difficulties to increase the gradient in conventional metal accelerating structures, as described in the previous section, has given rise to a broad research on a variety of novel, alternative particle accelerator schemes. These include

- the dielectric wakefield accelerator (DWA) [24, 25]
- the laser-driven plasma wakefield accelerator (LWFA) [26]
- the particle-beam-driven plasma wakefield accelerator (PWFA) [27] .

Different to metal accelerating structures, which are usually powered by a physically separated microwave generator, the abovementioned schemes rely on the collinear wakefield approach. In such collinear accelerators, a driver pulse (laser pulse in the case of LWFA or a particle bunch in the case of DWA/PWFA) excites wakefields in a structure or a medium, which travel at the speed of the driver. A witness particle bunch, trailing the driver bunch on the same axis ("collinearly"), can be accelerated in these wakefields. In beam-driven setups this has also been called the "Voss-Weiland scheme" [28]. Despite the similarity in physical principle, the realisation is different in these three most prominent schemes.

The DWA consists of a so-called dielectric-loaded waveguide (usually a tube of a dielectric material) which has a metal coating on its outside or is surrounded by metal walls. Space charge fields of a short ($\sim$ps), high current ($\sim$kA) particle bunch, that is passing through the dielectric tube, are delayed by the high-impedance dielectric material, reflected by the metal surrounding and thus reach the axis of the accelerator with a delay that is adjustable by the geometry of the DWA. Accelerating fields exceeding 1 GV/m have been demonstrated experimentally in a DWA [29].

Following preliminary work on particle acceleration in plasma wakes [30–32], laser-driven wake generation in a plasma to accelerate electron bunches was first proposed in 1979 by Tajima and Dawson [26]. A short laser pulse, which enters a plasma, pushes plasma electrons aside due to its Ponderomotive force and initiates a plasma electron oscillation. Due to these oscillations and the relative immobility of the much heavier plasma ions, cavities of negative and positive charge excess are formed. In between these regions

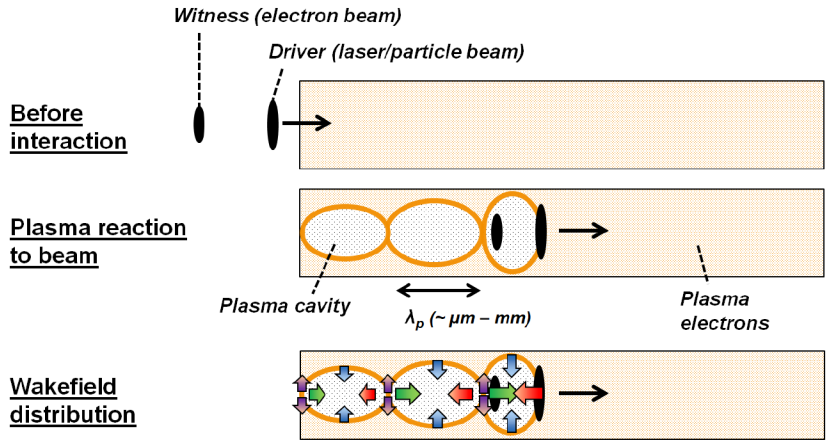

Figure 1.3: Illustration of driver and witness bunches before (top picture) and after (bottom pictures) entering the plasma acceleration medium. Orange dots represent plasma electrons, black dots excess plasma ions. Arrows illustrate the transverse focusing (blue) and defocusing (purple), and the longitudinally accelerating (green) and decelerating (red) forces.

of negative and positive net charge electric and magnetic (wake-)fields are present, which can be utilised to accelerate a witness beam. The scheme is shown in Fig. 1.3. Accelerating fields above 100 GV/m have been achieved experimentally [33, 34] and enabled by the fast development of laser technology — especially of femtosecond, TW-class pulsed lasers [35] — electron bunches of several GeV energy [36, 37] and bunch charges of up to several hundred picocoulombs have been produced by LWFAs in centimeter-scale plasmas to date. Despite the very promising results of LWFAs, several intrinsic drawbacks limit their applicability. First, the current energy limit of the drive laser pulse of up to several ten joules sets an upper limit to the energy gain of an accelerated bunch: the laser pulse deposits energy in the wake and therefore loses energy. After the so-called "depletion length" the pulse energy is too low to further drive a wake, i.e. accelerate [34]. A new driver pulse would be necessary to further increase the witness bunch energy. Second, the dephasing of drive pulse and the ultra-relativistic particle bunch, that is being accelerated, complicates maximisation of energy transfer from laser pulse to particle bunch: The group velocity of the laser pulse in the plasma medium is lower than the speed of light c, while the accelerated bunch quickly reaches velocities very close to c. Therefore, the accelerated bunch starts overtaking the wake, changing to decelerating phase

positions and eventually overtaking the driver [26, 38]. Third, the repetition rate of hundreds of TW and PW-class lasers (and therefore also of the high energy particle bunches produced with them) is currently limited to several ten pulses per second. Nevertheless, due to the high accelerating gradients and the comparably compact setup of the needed drive laser, LWFA could make high energy electron beams available for new applications [39, 40].
In PWFA, the plasma wake is driven by an intense particle bunch, which initiates plasma electron oscillations due to its space charge forces. Otherwise it follows the same principles depicted in Fig. 1.3. Among the main advantages of this acceleration scheme are the high accelerating fields up to tens of GV/m, that can be achieved [41] and the high possible energy gain in a single stage: As driver and witness bunches both travel at ultra-relativistic velocities ($\gamma_b \gg 1$), no significant dephasing takes place, which, in combination with possible driver energies up to hundreds of joules, enables high energy witness beams from single drivers. Furthermore, contrary to today's high power laser systems, particle driver repetition rates up to several MHz are possible due to the high average power output of state-of-the-art microwave amplifiers and superconducting accelerating cavity technology. At the same time the size of a PWFA driver beam accelerator is much bigger than that of a high power laser. Main applications of PWFA are therefore as an energy [42] and/or quality [43–45] booster or in a setup, where a witness bunch is accelerated in consequent PWFA stages by several driver bunches to higher energies than in a single stage with a similar driver bunch [46]. The driver bunches for the multiple stages can be supplied by a single conventional driver accelerator due to its high possible bunch repetition rate. All these schemes allow to either reach energies or beam qualities not accessible before with an existing machine, or to reduce the size of an accelerator for a target energy. In the following chapter, PWFA will be discussed in more detail to provide the theoretical basis which the present work is based upon.

Chapter 2

The Plasma Wakefield Accelerator

To provide a description of beam-driven wakefield acceleration in a plasma beyond the conceptual introduction given in Sec. 1.6 this chapter first discusses the basic phenomena in and the behaviour of the plasma medium, before a derivation of linear wakefield theory is given.

2.1 Plasma acceleration medium

Plasma is an at least partially ionised gas, that is macroscopically neutral and that exhibits collective behaviour [47]. The collective behaviour is caused by electromagnetic coupling between the free charge carriers (plasma ions and electrons). To describe a plasma usually parameters are employed, which allow to quantify this collective behaviour. These parameters are derived from the microscopic, single-particle movements by statistical averaging over particle ensembles [47]. In this macroscopic, statistical approach the plasma parameters can mostly be calculated from the physical quantities of the electron and ion densities ($n_{p,e}$ and $n_{p,i}$) and the plasma electron and ion temperatures (T_e and T_i). Due to the macroscopic neutrality it is usually assumed that in a singly ionised gas $n_{p,e} = n_{p,i}$. Therefore and due to the fact that the dynamics of the plasmas considered in this work are dominated by the plasma electrons, the electron/plasma density will further be referred to as n_e.
If energy transfer between plasma particles is dominated by collective effects and single-particle collisions can be neglected, the plasma is called *collision-*

less. A plasma is also called *cold*, if the thermal energies of plasma particles are negligible compared to electric potentials in the fields between plasma particles, i.e. collective effects dominate over thermal motion. All plasmas considered in this work are cold and collisionless.

To describe the physical processes in such a plasma, Maxwell's equations of electrodynamics

$$\nabla \cdot \mathbf{E} = \frac{\rho}{\epsilon_0} \ , \tag{2.1}$$

$$\nabla \cdot \mathbf{B} = 0 \ , \tag{2.2}$$

$$\nabla \times \mathbf{E} = -\frac{\partial \mathbf{B}}{\partial t} \ , \tag{2.3}$$

$$\nabla \times \mathbf{B} = \mu_0 \left(\mathbf{J} + \epsilon_0 \frac{\partial \mathbf{E}}{\partial t} \right) \ , \tag{2.4}$$

and the continuity and momentum equations of magnetohydrodynamics for cold, non-relativistic plasmas

$$\frac{\partial n}{\partial t} + \nabla(n\mathbf{v}) = 0 \ , \tag{2.5}$$

$$\frac{\partial \mathbf{v}}{\partial t} + (\mathbf{v} \cdot \nabla)\mathbf{v} = \frac{q}{m}(\mathbf{E} + \mathbf{v} \times \mathbf{B}) \ , \tag{2.6}$$

are employed [47–49]. Here ρ represents the charge density, ϵ_0 the vacuum permittivity, $\mathbf{J}$ the current density and $\mathbf{v}$ the velocity of the plasma fluid.

2.1.1 Debye-length

Due to the separation of charge carriers in a plasma, plasma particles rearrange their positions under the influence of external electric fields such, that the external field is compensated. This effect is called *Debye-shielding* and the characteristic length scale on which the field compensation takes place is called *Debye-length* λ_D. Debye-shielding is considered when the external field is static or its frequency is much lower than the plasma frequency (see next section). For frequencies comparable to the plasma frequency the plasma

skin-depth defines the penetration depth (see Sec. 2.1.3). The electron Debye-length is calculated by [47]

$$\lambda_{D_e} = \sqrt{\frac{\epsilon_0 k_B T_e}{4\pi n_e e^2}} \ , \tag{2.7}$$

where k_B is the Boltzmann constant and e the elementary charge. Similarly, an ion Debye-length can be calculated. The plasma ions are considered to be immobile compared to the much lighter plasma electrons, which hence re-arrange their positions much quicker to create net negative or positive space charges. It is therefore assumed that $\lambda_D \approx \lambda_{D_e}$. If the size of a system (i.e. plasma) is large compared to λ_D, the system can be considered macroscopically quasi-neutral, as the field of any concentration of charges is shielded within the system [48].
To classify plasmas the so-called plasma parameter

$$\Lambda = \frac{4\pi}{3} n_e \lambda_D^3 \ , \tag{2.8}$$

is introduced [47], which describes the number of plasma electrons within a Debye-sphere. Plasmas with $\Lambda \gg 1$ are also called *ideal plasmas*, as the inter-particle interaction is shielded and therefore weak compared to the thermal energy of the particles. The plasma can be treated approximately like an ideal gas. In other terms, Debye-shielding only takes place for such ideal plasmas, as otherwise no collective behaviour can provide the field compensation within one Debye-length.
As shown in Fig. 2.1, plasmas in the parameter range for PWFA are ideal plasmas and can be treated correspondingly. The separation between ideal and non-ideal plasma is definded as $\Lambda = 1$ [Eq. (2.8)].

2.1.2 Electron plasma frequency

If a plasma electron is displaced from its equilibrium position, it experiences a restoring force by the (immobile) positive ion background and excess of negative charges at the displacement position. Due to its inertia, the electron will not return to but overshoot the equilibrium position and the process repeats. The frequency of the consequent harmonic oscillation is called *plasma frequency*. This plasma frequency also defines the "reaction time" of the plasma to external influence. Electromagnetic radiation with a frequency higher than the plasma frequency is transmitted through the plasma,

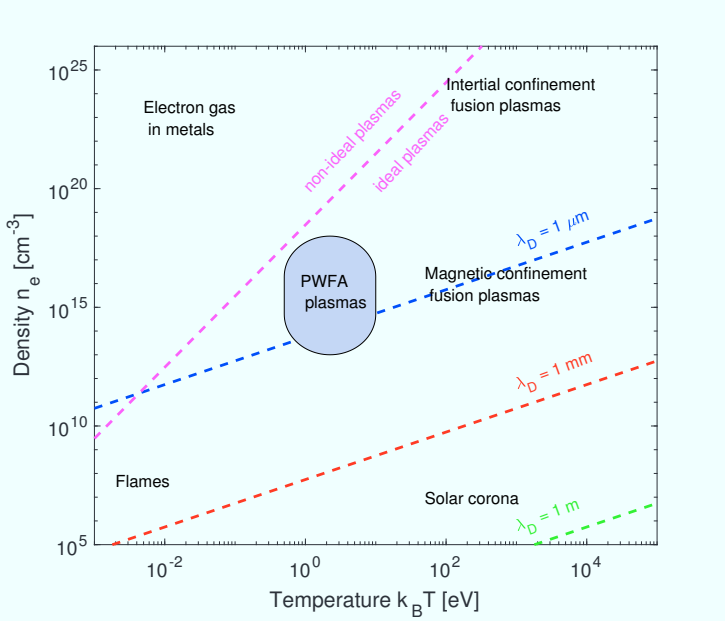

Figure 2.1: Classification of plasmas of different densities and temperatures (cf. [47]).

as the plasma electrons cannot react quickly enough to shield its fields. If the frequency of the radiation is lower than the plasma frequency the wave is shielded/reflected at the plasma boundary.
The plasma frequency f_p can be derived assuming that no time-dependent magnetic fields are present. Equation (2.3) reveals for this case, that $\mathbf{E}$ can be described as the gradient of a scalar electric potential ϕ

$$\mathbf{E} = -\nabla\phi \ . \tag{2.9}$$

Substituting this into Eq. (2.1) yields

$$\nabla^2\phi = -\frac{\rho}{\epsilon_0} \ , \tag{2.10}$$

which is called Poisson's equation of electrostatics.
Solving this equation for a cold plasma with fixed plasma ion background, no external magnetic field and assuming one-dimensional, linear motion yields [48, 50]

$$f_p = \omega_p/2\pi = \sqrt{\frac{n_e e^2}{4\pi^2\epsilon_0 m_e}} \ . \tag{2.11}$$

Here, ω_p is the angular frequency of the plasma oscillation (also sometimes referred to as plasma frequency).
Correspondingly, a plasma ion frequency can be calculated, which (due to the higher mass) is much lower and therefore negligible in all cases considered here.

2.1.3 Plasma wavelength and skin-depth

The relation [48]

$$\omega_w^2 = \omega_p^2 + c^2 k_w^2 \tag{2.12}$$

describes the dispersion of a transverse electromagnetic wave in a plasma, where ω_w is the angular frequency of the incident wave and k_w its wave number. Equation (2.12) can only be fulfilled for $\omega_w < \omega_p$ with imaginary k_w-values. This phenomenon is called *cutoff* and describes mathematically the shielding and reflection of electromagnetic waves from a plasma if their frequency is lower than the plasma frequency, as already mentioned above. The spatial component of an incoming, one-dimensional, plane electromagnetic wave traveling in x-direction in time t

$$E = E_0 \exp[i(k_w x + \omega_w t)] \tag{2.13}$$

becomes $\exp(-|k_w|x)$ for imaginary values of k_w, which corresponds to a spatially damped field distribution. As k_w^{-1} defines the length scale on which the wave is attenuated, it is also called skin-depth, in analogy to the extrusion of alternating currents (AC) from the inside of electric conductors by the skin-effect. For oscillations with the plasma frequency the so-called *plasma skin-depth* is therefore $k_p^{-1} = \frac{c}{\omega_p}$ [48]. The wavelength of a plasma oscillation is given by

$$\lambda_p = 2\pi/k_p = \frac{2\pi c}{\omega_p} \ . \tag{2.14}$$

2.1.4 Wakefield excitation in plasmas

One of the main advantages in employing a plasma as an acceleration medium compared to evacuated metal cavities is that no classical breakdown occurs. Vacuum breakdown arises from charge carriers (electrons) surpassing the boundary of the metal walls (by e.g. field emission) and consequent discharge formation (see Sec. 1.5). The charge carriers in a plasma are flowing unhindered. Therefore, the achievable electric field in a plasma wake is not

limited by field emission or other effects but given approximately by the cold plasma, non-relativistic wave-breaking limit [26]

$$E_{br} = \frac{m_e c_0 \omega_p}{e} \ . \tag{2.15}$$

This is derived by solving Gauss's law [Eq. (2.1)] for a one dimensional, plane plasma wave with the charge density $\rho = e \cdot \Delta n_e \cdot e^{ik_p z}$ [48] in the case of displacement of all plasma electrons ($\Delta n_e \sim n_e$). This can also be written as [48, 51]

$$E_{br}(V/m) \approx 96\sqrt{n_e \ [\mathrm{cm}^{-3}]} \ . \tag{2.16}$$

From this formula it can be seen, that at a moderate plasma density of e.g. $n_e = 10^{16}\,\mathrm{cm}^{-3}$ a field of nearly 10 GV/m can be reached, which already exceeds conventional technology limits by two orders of magnitude.
To excite such a plasma wake, the driver particle bunch has to initiate an oscillation of the plasma electrons. Hence, the bunch tail needs to be shorter or on the order of the plasma wavelength. Otherwise, the plasma electron displacements introduced by the driver beam will be smoothly shielded [27]. Even though the excitation of the wake is a radiative process, in which the space charge fields of the driver leads to emission of Čerenkov radiation [52, 53], the phase velocity of the excited wakefield corresponds to the velocity of the driver, which is usually higher than the group velocity of electromagnetic waves in the plasma. This is due to the wakefield resulting from an oscillation of plasma electrons, the phase propagation of which is not subject to the change in group velocity of electromagnetic waves in plasma. The group velocity of a linear wake is zero [49], i.e. the centres of the plasma electron oscillations do not propagate in the laboratory frame of the plasma medium. This will also be shown mathematically in the following derivation of linear wakefields in PWFA.

2.2 Linear wakefield theory

To calculate the fields excited by a relativistic driver beam of peak density n_b in a plasma we have to distinguish between different regimes of the interaction:

1. $n_b \ll n_e$: the driver introduces a small perturbation to the equilibrium plasma density

2. $n_b \geq n_e$: displacement of all plasma electrons.

Case 1. is also called the linear regime (as the plasma electrons respond linearly to the perturbation). Case 2. is divided into the quasi-nonlinear and the nonlinear regime, which will be discussed in Ch. 4.2.
Below, we will derive the wakefields of a point-like driver bunch moving with velocity v_b in z-direction in the linear, one-dimensional (1D) case [27, 49]. This is also sometimes referred to as the *wide beam limit* as it approximately applies to beams with transverse RMS sizes $\sigma_r > c/\omega_p$ [54].
From Eqs. (2.1) – (2.6) we can derive

$$\frac{\partial \delta n}{\partial t} + n_e(\nabla \cdot \mathbf{v}) = 0 \ , \tag{2.17}$$

$$\frac{\partial \mathbf{v}}{\partial t} = \frac{e\mathbf{E}}{m} \tag{2.18}$$

for a plasma density perturbation δn by using our assumption $n_b \ll n_e$ and keeping only first order, linear terms. From Eq. (2.1) we obtain

$$\nabla \mathbf{E} = \frac{e}{\epsilon_0}(\delta n + n_b) \tag{2.19}$$

for the considered case. Substituting Eq. (2.18) into the time derivative of Eq. (2.17) and using identity (2.19) yields

$$\frac{\partial^2 \delta n}{\partial t^2} + \omega_p^2 \delta n = -\omega_p^2 n_b \ . \tag{2.20}$$

The absence of a spatial derivative in Eq. (2.20) is the mathematical manifestation of the zero group velocity of the excited wake [49]. By substituting t with

$$\xi = v_b t - z \ , \tag{2.21}$$

and introducing the 1D bunch density distribution

$$n_b = \sigma \delta_D(\xi) \ , \tag{2.22}$$

Eq. (2.20) becomes

$$\frac{\partial^2 \delta n}{\partial \xi^2} + k_p^2 \delta n = -k_p^2 \sigma \delta_D(\xi) \ . \tag{2.23}$$

Here, σ is a homogeneous line number density, δ_D is the Dirac delta function and it is assumed that $v_b \approx c$. From Eq. (2.23) the impulse response of the plasma can be calculated [49, 55]:

$$\delta n = -k_p \sigma sin(k_p \xi)\Theta(-\xi) \ , \tag{2.24}$$

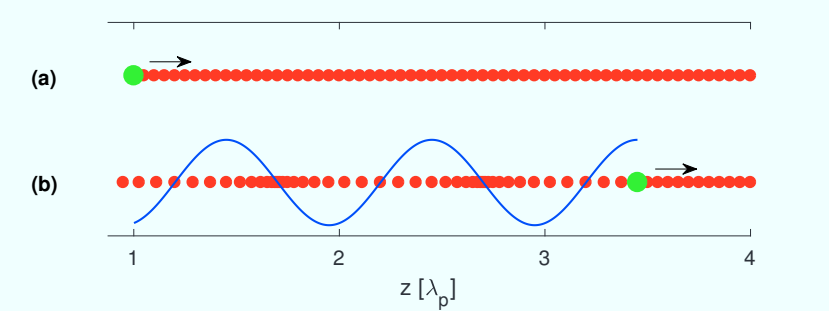

Figure 2.2: Idealised electron distribution in 1D wakefields. Plasma electrons (red dots) are homogeneously distributed prior to the entry of the driver (green dot) into the plasma (a). The driver bunch then initiates longitudinal oscillations of the plasma electrons (red) at passage (b). Periodic regions of enhanced and lowered plasma electron concentration form. The blue line shows the longitudinal electric field behind the driver.

with Θ being the Heaviside step function. Solving Eq. (2.19) for (2.24) yields

$$E = \begin{cases} -\frac{e}{\epsilon_0} n_b cos(k_p \xi) & \xi < 0 \\ -\frac{e}{2\epsilon_0} n_b & \xi = 0 \\ 0 & \xi > 0 \ , \end{cases} \tag{2.25}$$

or for a volume charge density $\rho(z)$ [55]

$$E = -\frac{1}{\epsilon_0} \int_{\infty}^{\xi} d\xi' \rho(\xi') cos[k_p(\xi - \xi')] \ . \tag{2.26}$$

The factor $1/2$ at $\xi = 0$ in Eq. (2.25), which results from $\Theta(0) = 1/2$, can also be derived from energy conservation: The energy $\mathcal{E}_W$ stored in the electrical field behind the bunch is

$$\mathcal{E}_W = 1/2\epsilon_0 |E_{peak}|^2 = \frac{e^2 n_b^2}{2\epsilon_0} \ , \tag{2.27}$$

with E_{peak} the maximum field amplitude behind the bunch. The energy lost by the driver bunch $\Delta\mathcal{E}_D$ is

$$\Delta\mathcal{E}_D = E(0) e n_b. \tag{2.28}$$

If the energy is conserved, Eqs. (2.27) and (2.28) yield the result shown in Eq. (2.25). Figure 2.2 visualises the 1D plasma particle motion in a plasma

wake driven by a point-like driver. Longitudinal plasma particle oscillations with the plasma frequency are initiated by the passage of the driver and lead to periodic areas of enhanced and lowered plasma electron density. The maximum wakefield amplitudes appear between the regions of maximum net charge excess.
Similarly, in two dimensions, the longitudinal wakefields of an infinitely short bunch of N electrons with parabolic surface charge density distribution $\frac{2N}{\pi a^2}(1 - r^2/a^2)$ moving with v_b can be calculated to be [49]

$$E_z(r,z,t) = \begin{cases} -\frac{2Ne}{\pi\epsilon_0 a^2}\left(1-\frac{r^2}{a^2}\right)\cos(k_p z - \omega_p t) & z < v_b t \\ -\frac{Ne}{\pi\epsilon_0 a^2}\left(1-\frac{r^2}{a^2}\right) & z = v_b t \\ 0 & z > v_b t \ , \end{cases} \tag{2.29}$$

to which the transverse fields behind the bunch are related via the *Panofsky-Wenzel theorem* $\partial E_z/\partial r = \partial(E_r - B_\theta)/\partial(z - ct)$ [34, 49, 56]:

$$(E_r - B_\theta)(r,z,t) = \frac{4Ne}{\pi\epsilon_0 a^2}\frac{r}{k_p a^2}\sin(k_p z - \omega_p t) \ . \tag{2.30}$$

Equations 2.25, 2.29 and 2.30 will be used in the following chapters to deduce different characteristics and beam transport issues in PWFA.

Chapter 3

High transformer ratio wakefield acceleration

Already the first publications on PWFA contain basic considerations on the maximum possible energy gain of the accelerated particles [49, 57]. This energy is acceleration gradient integrated along the acceleration length. Equations (2.25) and (2.29) show that the maximum gradient in the PWFA is defined by the properties (charge, spot size) of the driver bunch. The length over which this gradient can be maintained is given by the driver's energy and the decelerating field within the driver. By driving the plasma wake, the driver deposits energy in the oscillations of plasma electrons and is therefore decelerated. If the driver energy drops below ultra-relativistic energies ($\gamma_b \gg 1$), the assumption $v_b \approx c$ is not valid anymore and the highly relativistic witness bunch will slip to decelerating phases of the wake and finally overtake the driver. The wakefield behind the driver will also be perturbed if a part (i.e. slice) of the driver drops below ultra-relativistic energies so that no stable acceleration is possible anymore. Assuming that the energy at which dephasing has to be considered is negligible compared to the initial driver energy $\mathcal{E}_{driver,0}$, the maximum energy gain of the witness is given by

$$\Delta\mathcal{E}_{witness} \approx \frac{E_{acc}}{E_{dec}} \cdot \mathcal{E}_{driver,0} = R \cdot \mathcal{E}_{driver,0} \ , \tag{3.1}$$

where E_{acc} is the maximum accelerating field behind and E_{dec} the maximum decelerating field within the driver. R is called the *transformer ratio* (in the following text abbreviated as TR). It defines either the reachable final witness beam energy for a given $\mathcal{E}_{driver,0}$ or the needed $\mathcal{E}_{driver,0}$ (i.e. length of the driver beam accelerator) for a targeted final witness energy. This

concept was already known from structure-based wakefield acceleration and transferred to the PWFA [49, 57, 58]. The following sections will give an introduction to the limits of the transformer ratio in linear wakefields for conventional particle bunches, as well as an overview of the concepts how to overcome these limits. Finally the relation between transformer ratio and the efficiency of a PWFA is discussed.

3.1 Symmetric bunches in linear wakefields

From Eqs. (2.25) and (2.29) one can see that the ratio between maximum accelerating field behind (cosine equal to 1) and decelerating field within a point-like driver bunch results in a transformer ratio of 2. This can be visualised by a strongly simplified model [59]: As a particle is only subject to the wake of the preceeding charge, a point-like driver bunch only witnesses half of its own wakefield. The witness behind the driver on the other hand sees the full wakefield and thus the TR is 2.
This is also the upper limit of the TR for finite-length driver bunches with symmetric current distribution $I(\tau)$ (e.g. Gaussian) as was found in simulations [60] and derived theoretically in the so-called *fundamental theorem of beamloading* [58, 61]: Particles at a position t in a driver bunch which extends from a time $-T$ to a time T and traveling with velocity -c experience a longitudinal wakefield potential

$$\begin{aligned} U_{dec}(t) &= -\int_{-T}^{t} I(\tau)\cos[\omega_p(t-\tau)]\mathrm{d}\tau = \\ &= -\cos(\omega_p t)\int_{-T}^{t} I(\tau)\cos(\omega_p\tau)\mathrm{d}\tau - \sin(\omega_p t)\int_{-T}^{t} I(\tau)\sin(\omega_p\tau)\mathrm{d}\tau \end{aligned} \quad (3.2)$$

according to Eq. (2.25). Similarly, the potential behind the driver follows

$$U_{acc}(t) = \cos(\omega_p t)\int_{-T}^{T} I(\tau)\cos(\omega_p\tau)\mathrm{d}\tau + \sin(\omega_p t)\int_{-T}^{T} I(\tau) sin(\omega_p\tau)\mathrm{d}\tau\ . \quad (3.3)$$

In case of a symmetric driver bunch the integral in the second term in Eq. (3.3) is zero. If the maximum value $U_{dec,max}$ of U_{dec} appears at $t = 0$ then $|U_{dec,max}|$ is half of the maximum value behind the driver $U_{acc,max}$, as the first integral of Eq. (3.2) integrates over half of the symmetric current distribution and the second term is zero. The TR is $\left|\frac{U_{acc,max}}{U_{dec,max}}\right| = 2$. If $U_{dec,max}$ does not appear at $t = 0$, this value is by definition bigger than $U_{dec}(t = 0) = -U_{acc,max}/2$ and therefore the TR is lower than 2.

For Gaussian driver bunches, the maximum TR of 2 is reached if the longitudinal RMS-length σ_z fulfills $k_p\sigma_z = \sqrt{2}$ [54]. Bunches which deviate from this optimal length produce lower TRs. This is also shown in Fig. 3.1, where (a) depicts the normalised 1D linear wakefields of a bunch matching this condition and (b) the fields driven by a bunch with $k_p\sigma_z \approx 0.3$.
Due to this limitation of the transformer ratio for symmetrical driver bunches, a TR above 2 is considered high (i.e. *high transformer ratio*, HTR).

3.2 Asymmetric bunch distributions

The *fundamental theorem of beamloading* is derived for longitudinally symmetric bunches which excite wakes in single mode structures. Even though considerations on using multi-mode structures have yielded that HTRs are possible in such devices [58], the only possibility to achieve HTR in a linear wake in a plasma as a single-mode medium is to introduce asymmetric

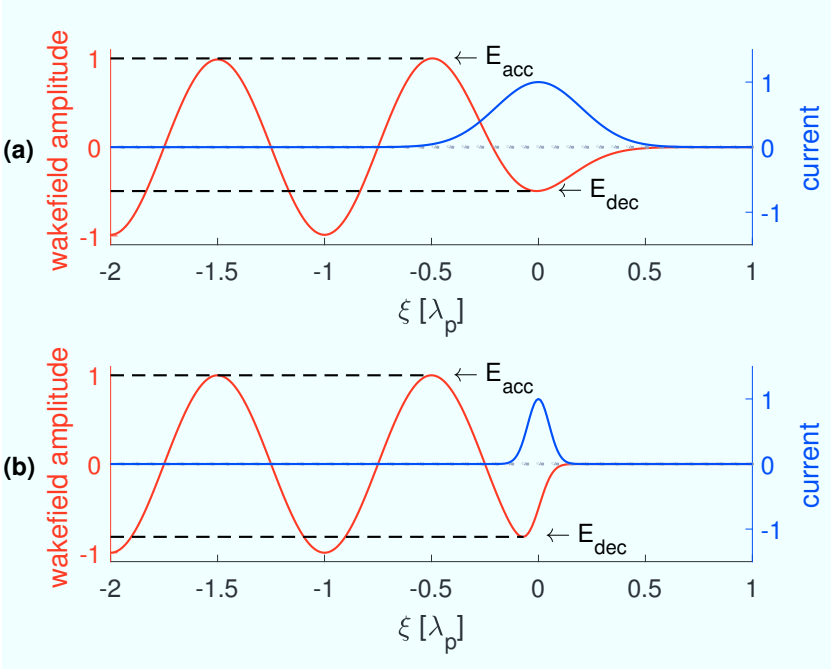

Figure 3.1: Linear wakefields according to Eq. (2.25) (red lines, normalised units) driven by Gaussian driver bunches of matched (a) and short (b) lengths (blue lines show normalised current profiles) traveling to the right, with the maximum acceleration E_{acc} behind and maximum deceleration E_{dec} within the drivers (cf. [58]).

current distributions to drive the wake.

3.2.1 Single shaped bunches

Single asymmetric driver bunches were first proposed to overcome the TR limit [58, 62] and the concept was transferred to PWFA shortly after [57, 63]. One of the proposed bunch shapes is the so called "triangular" bunch [Fig. 3.2 (a)] which exhibits a current profile of

$$I(\xi) = \begin{cases} 0 & \xi < 0 \\ \frac{I}{\lambda_p}(L_b - \xi) & 0 < \xi < L_b \\ 0 & \xi > L_b \ , \end{cases} \tag{3.4}$$

where I is the maximum current of the bunch, λ_p the plasma wavelength and L_b the total length of the bunch [57]. The TR of a triangular bunch can be derived from calculating the maximum amplitude of the longitudinal wakefields within (E_{dr}) and behind (E_w) the bunch from Eq. (2.26). In the simplified case of bunch lengths equal to an integer number of plasma

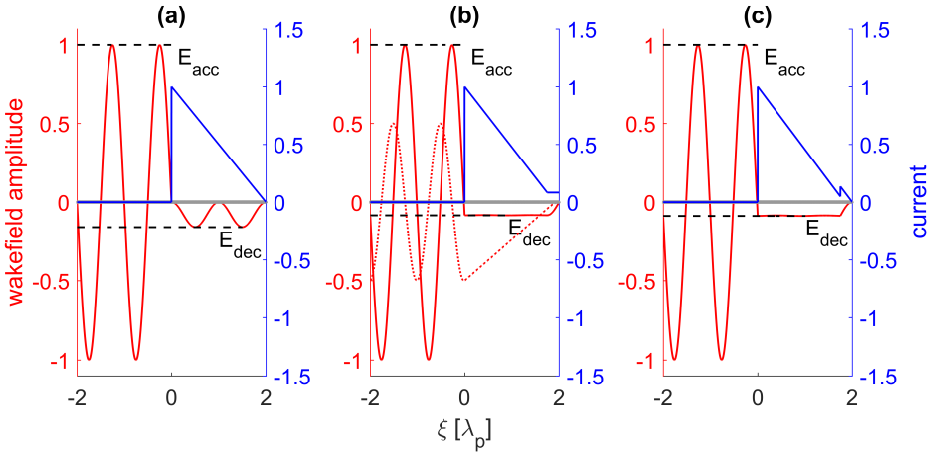

Figure 3.2: Linear longitudinal wakefields for different asymmetric bunch current distributions calculated according to Eq. (2.25). Blue curves show the normalised driver bunch currents, solid red lines the normalised longitudinal wakefields and the dotted red line in (b) the transverse wakefields in arbitrary units, which will be further discussed in Sec. 4.2.2 (cf. [57]).

wavelength ($L_b = N \cdot \lambda_p$, $N \in \mathbb{N}$) we can derive

$$E_{dr}(\xi) = \frac{I}{\epsilon_0 \lambda_p} \int_{\xi}^{L_b} (L_b - \xi') \cos[k_p(\xi - \xi')] d\xi' = \frac{I}{\epsilon_0 \lambda_p} \frac{1}{k_p^2} (\cos[k_p(\xi - L_b)] - 1) \quad (3.5)$$

and

$$E_w(\xi) = \frac{I}{\epsilon_0 \lambda_p} \int_{0}^{L_b} (L_b - \xi') \cos[k_p(\xi - \xi')] d\xi' = \frac{I}{\epsilon_0 \lambda_p} \frac{L_b}{k_p} \sin[k_p(\xi)], \quad (3.6)$$

which yields a transformer ratio R of

$$R = -\frac{E_{w,max}}{E_{dr,max}} = \pi \frac{L_b}{\lambda_p} = \pi N \ . \quad (3.7)$$

Analogously, it can be derived that triangular bunches with a precursor, which is usually one quarter plasma wavelength long, can drive wakefields with TRs up to [57]

$$R \simeq 2\pi \frac{L_b}{\lambda_p} \ . \quad (3.8)$$

The precursor in this scheme displaces plasma electrons such, that at the end of the precursor the displacement rate of plasma electrons is balanced by the incoming, linearly rising current of the triangular part of the bunch [64]. Among the proposed bunch profiles are the so-called "doorstep" [triangular with rectangular precursor, Fig. 3.2 (b)] [57], the "double-triangle" [triangular with a triangular precursor, Fig. 3.2 (c)] [65], cosine-like bunches [66] and various others [67, 68]. The optimal bunch profile, i.e. achieving the highest TR, would be the one which produces wakefields which are constant along the whole driver bunch [57, 64]. A triangular bunch with a δ-function as a precursor was shown to provide this [57].
As it is impossible to produce bunches with infinitely sharp edges experimentally, approximations of these profiles have to be considered [69]. The impact of such non-ideal bunch profiles on the TR is negligible as long as the distortions are within a certain range [65, 69]. This means that e.g. the falling edge at the bunch tail should be shorter than $\lambda_p/2\pi$ to keep the TR at 90 % of the ideal [69].
It should be noted that increasing the TR of a driver bunch can significantly reduce the wakefield gradient at constant driver bunch charge [54, 68]. This

is caused by the lower peak current and thus also peak particle density of the bunch at longer length and can be counteracted by increasing the driver bunch charge.
HTR concepts based on single driver bunches promise higher TRs than other proposed schemes (see e.g. Sec. 3.2.2) but are complex to realise experimentally (see also Sec. 4.1 and Ch. 7). Only recently HTR acceleration using single shaped bunches was reported in a structure-based wakefield accelerator [70].

3.2.2 Asymmetric bunch trains

Due to the complex production of single asymmetric, HTR-capable bunches, schemes based on trains of symmetric driver bunches were proposed [71–75]. A series of N driver bunches is injected into a wakefield structure or medium such that their self-wakefield and the wakefields of preceding driver bunches add to a constant decelerating field in all driver bunches. Hence, the field within the m-th bunch according to Eq. (2.26), which has to be identical to the self-wakefield of the first bunch, is given by

$$E_m = -\frac{e}{2\epsilon_0} n_{bN} + \left(\sum_{m=1}^{N-1} -R_m \frac{e}{2\epsilon_0} n_{bm} \cos k_p(\xi - \xi_m) \right) \equiv -\frac{e}{2\epsilon_0} n_{b1} \tag{3.9}$$

under the assumption of point-like driver bunches. Here n_{bm} is the 1D bunch density distribution (which is directly correlated with the bunch charge Q_m), R_m is the transformer ratio and ξ_m the position of the m-th bunch. The wakefield behind the train of bunches according to Eq. (2.26) is given by

$$E(\xi) = \sum_{m=1}^{N} -R_m \frac{e}{2\epsilon_0} n_{bm} \cos k_p(\xi - \xi_m) \ . \tag{3.10}$$

For point-like driver bunches the transformer ratios of the single bunches R_m are equal to 2. The transformer ratio of the train is given by the maximum of $\frac{-E(\xi)}{E_1}$. Utilising Eqs. (3.9) and (3.10) the phases (i.e. positions) and the charges of the driver bunches which maximise the transformer ratio can be defined. Two schemes were proposed, which are shown in Fig. 3.3. The first scheme [Fig. 3.3 (a)], also called "ramped bunch train (RBT)", employs a train of N driver bunches with constant bunch-to-bunch distance $(n+0.5)\lambda_p$, $n \in \mathbb{N}_0$, but rising charge of $Q_m = Q_1(2m-1)$, where Q_1 is the charge of the first driver bunch. The TR of such a train of bunches is [71–76]

$$R_{RBT} = 2 \cdot N \ , \tag{3.11}$$

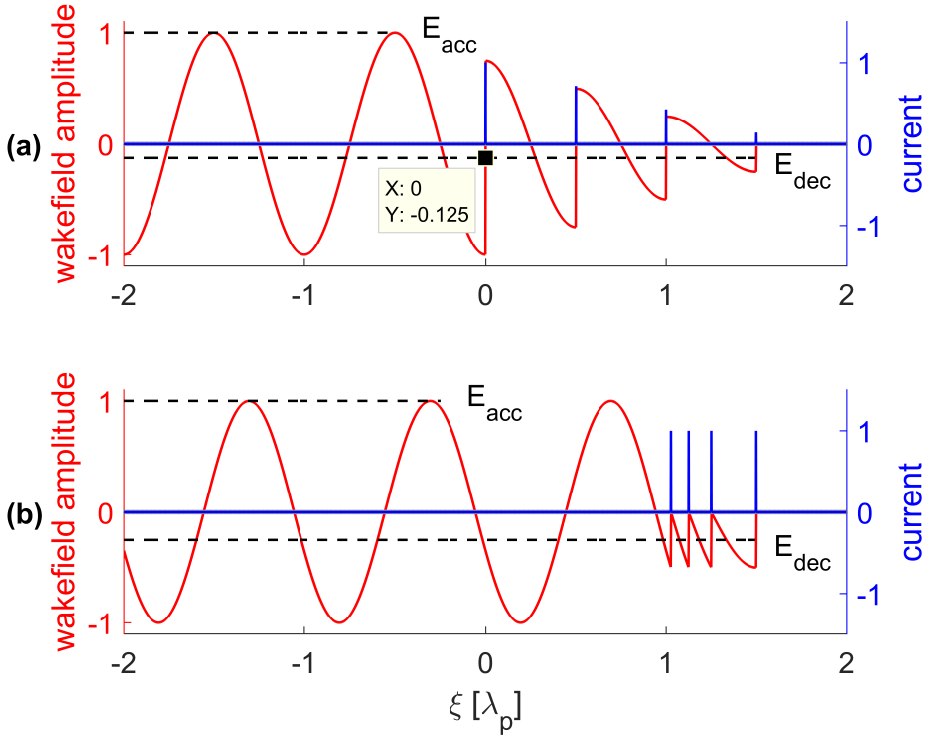

Figure 3.3: Normalised linear wakefields according to Eq. (2.25) (red lines) for the two HTR schemes based on trains of driver bunches with rising bunch charge and constant bunch separation (a) and with constant bunch charge and varying bunch separation (b). Blue lines show the normalised driver currents. In (a) the homogeneity of the wakefields within the driver bunches is illustrated by the annotation.

which can be seen for a train of 4 driver bunches in Fig. 3.3 (a), where $R_{RBT} = 1/0.125 = 8 = 2 \cdot 4$. Wakefields are constant within the driver bunches as illustrated in Fig. 3.3 (a) by the annotation, which shows the wakefield amplitude at the position of the last driver bunch.
The second scheme [Fig. 3.3 (b)] utilises again a train of N driver bunches but with constant bunch charges and bunch-to-bunch delays $\tau_m = \frac{1}{\sqrt{m}\omega_p}$. A TR of $2\sqrt{N}$ can be achieved using this method [71–75]. Due to this significantly lower achievable TR the latter method was not pursued experimentally.

Even though a train of small bunches seemed to ease the demands for the bunch shaping capabilities of the driver beam accelerator compared to

single, shaped bunches, the concept suffers from several experimental issues especially in a plasma medium:

1. Equation (3.11) only holds for optimal matching of all individual driver bunches to the wake, i.e. the TR of every single bunch has to be 2. This is difficult to achieve for bunches of significantly different charges as space charge effects can change the bunch length significantly (see also Ch. 7). A lower single bunch TR complicates the relations for the bunch charges and bunch positions and rapidly diminishes the TR of the bunch train [77, 78].

2. It can be challenging to transport bunches of significantly different charges through the same beam optics to the wakefield accelerator. Especially if the bunch shaping is done at low energies, space charge forces influence the bunch parameters. Bunches of different charges will have different Twiss-parameters and therefore also e.g. different focus points (see also Chs. 7 and 9).

3. Despite various illustrations of bunch train HTR schemes, wakefields are not necessarily purely decelerating within an optimally matched longitudinally symmetric bunch distribution as e.g. Gaussian (see also Fig. 3.1). This leads to saturation and even decrease of the achievable TR [79].

4. The linear transverse fields in a PWFA within the driver bunches exhibit a quadratic dependence on the number of preceding driver bunches, while the longitudinal fields are constant [76]. This means that all driver bunches will experience different focusing fields in the linear interaction regime and therefore the beam charge density within the bunches will not be directly correlated to the bunch charge. As the wakefield amplitude depends on the beam charge density, the concept of linearly increasing the bunch charge to linearly increase the accelerating field behind the driver bunch train while keeping the wakefields within the driver bunches constant is not valid without further tailoring of the bunches (e.g. adjusting individual bunch emittances). This issue might be overcome by operating in a quasi-nonlinear regime of the PWFA (see also Ch. 4.2) [80–82].

The RBT concept was implemented experimentally at the Argonne Wakefield Accelerator at Argonne National Laboratory, where collinear acceleration in a structure-based wakefield with enhanced [83] and high trans-

former ratios [84] were reported for the first time. It was also proposed for PWFA experiments at the **P**hoto-**I**njector **T**est facility at DESY in **Z**euthen (PITZ) [85, 86], which was the starting point of the present work. After preliminary wakefield calculations and due to the limitations listed above, implementation of the RBT concept at PITZ was discontinued in this work in favour of single shaped bunch concepts.

3.3 Efficiency in PWFA

The efficiency η of a PWFA (or other collinear wakefield accelerators) is the amount of energy transferred from the driver bunch to the witness bunch, which is given by

$$\eta = \frac{W_{gain}}{W_{dep}} \ . \tag{3.12}$$

For an idealised case of constant fields in driver and witness bunches $W_{gain} = N_{wit} \cdot L \cdot E_{acc}$ is the total amount of energy gained by the $N_{wit} = Q_{wit}/e$ particles of the witness bunch accelerated in the longitudinal field E_{acc} in a plasma of length L. Analogously $W_{dep} = N_{drive} \cdot L \cdot E_{dec}$ is the total energy loss of $N_{drive} = Q_{drive}/e$ driver bunch particles in a decelerating wakefield E_{dec}. As $\eta \leq 1$ and the TR is defined as $R = \frac{E_{acc}}{E_{dec}}$, Eq. (3.12) can also be written as

$$\eta = R \cdot \frac{Q_{wit}}{Q_{drive}} \ , \tag{3.13}$$

which implies a dependency of the TR on the driver and witness charges if Q_{wit} approaches Q_{drive}.

3.3.1 Beamloading in PWFA

Beamloading is known from conventional accelerators and describes the reduction of the accelerating field due to extraction of energy by accelerated particles. A similar phenomenon is also present in plasma accelerators [55,87]. The resulting wakefield at a certain position is the superposition of the wakefields of the total preceding charge [see also Eq. (2.26)]. Therefore, if the wakefield of the witness bunch is not negligible compared to the driver bunch, the wakefield behind and within the witness will be modified by its self-wake. This can be employed to reduce the energy spread in PWFA by flattening the wakefields inside the witness bunch [55,87,88], which could solve one of the limitations for the application of PWFA. By loading the wake

with even more witness charge, the wakefield behind the witness bunch can be reduced to zero, which maximises the efficiency of the PWFA at the expense of increasing the energy spread of the witness bunch. In both cases the accelerating field and consequently the TR are reduced by the beamloading.

3.3.2 Transformer ratio and maximum efficiency

Even though TR, accelerating field and efficiency can only be traded against each other, depending on the demands on the final witness beam parameters, TR and efficiency maximisation are nevertheless closely connected.
To maximise the overall energy transfer from a driver to a witness bunch, first the energy extraction from the driver has to be maximised [89, 90]. Assuming again that acceleration is possible as long as all driver particles have an energy >0 (i.e. the homogeneous initial driver particle energy is much bigger than the energy at which particle velocities cannot be assumed equal to c anymore) the maximum amount of energy can be extracted if all driver particles experience the same decelerating field. This is identical to the prerequisite for achieving the maximum TR [57] (see also Sec. 3.2). Maximising the TR of the wakefield of a driver bunch hence is the first step in maximising the efficiency of a PWFA. Therefore, even though maximisation of the energy extraction by the witness bunch via beamloading means that the TR is reduced, maximisation of the transformer ratio of a driver bunch enables maximisation of the efficiency of a PWFA.

Chapter 4

Instabilities and nonlinear PWFA

4.1 Beam-plasma instabilities

It was described in Ch. 3 that achieving maximum transformer ratios and enabling maximum efficiencies in a PWFA requires the utilisation of long, shaped driver bunches. Numerical simulations revealed that transport of such bunches through a plasma — and thus also stable acceleration of a witness bunch — can be severely affected by beam-plasma instabilities [64,69,91–95]. These instabilities can arise from noise and typically have growth lengths which are much smaller than typical PWFA lengths. The following sections will briefly discuss the nature and possible mitigation strategies of the most severe instabilities.

4.1.1 Current filamentation

The current filamentation instability (CFI) describes the transverse breakup of a relativistic beam in a plasma into several separate filaments [69,91,96–98]. This effect is also often referred to as Weibel- or Weibel-like instability [96,99,100]. It is caused by non-uniformities in the counterflowing beam and plasma currents, which lead to net magnetic fields. The space charge of an electron bunch that penetrates a plasma exerts a force on the plasma electrons. Depending on the position of the plasma electrons with respect to the bunch trajectory, this force has varying longitudinal and transverse components. Plasma electrons are therefore also displaced longitudinally and transversely from their equilibrium positions, leading to plasma electron (re-

turn) currents in longitudinal direction (see also the pure longitudinal plasma electron movement in the 1D limit in Fig. 2.2). As the bunch and plasma return currents are repelling each other due to their opposing magnetic fields, a transverse inhomogeneity leads to local compression and unstable enhancement of the seed perturbation.
CFI was observed and characterised [101] in plasma wakefield accelerators and mitigation is well understood. The instability is suppressed when the transverse RMS-beamsize σ_r fulfills $k_p\sigma_r < 1$ [91] ($k_p\sigma_r < 2.2$, determined empirically [101]). While it effectively limits the maximum plasma density that can be used in a PWFA for a given transverse beam size, this requirement coincides with the conditions for mitigation of other instabilities in the present study (see also Ch. 9).

4.1.2 Hosing instability

When a bunch travels in the focusing channel of a plasma wake it is focused by the positive and negative net charges of the plasma particles. If a slice of the bunch is subject to a transverse offset from the propagation axis, it feels a restoring force [Fig. 4.1(b), red arrows] [102]. At the same time, the centroid offset leads to a distortion of the plasma wake behind the displaced slice, which exerts a displacing force on consequent slices [Fig. 4.1(b), red arrows]. If all particles within a slice have the same betatron frequency, the slice will start oscillating with this frequency within the plasma wake [102]. If the betatron frequencies of all slices match, an unstable amplification leads to growing oscillation amplitudes along the bunch up to beam breakup [Fig. 4.1(c)] [93], which is called *hosing* or *electron hose instability*. This instability was found in analytical calculations and three-dimensional numerical sim-

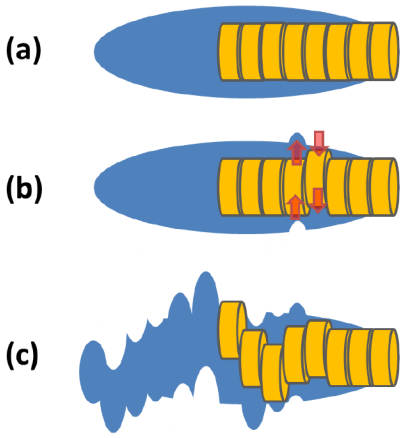

Figure 4.1: Illustration of the hosing instability evolution. A symmetric bunch creates a symmetric plasma response (a). Transverse offsets lead to initiation of betatron oscillations by transverse forces (b). Oscillations of identical frequency grow unstably (c).

ulations of PWFA for various parameters and suggested severe limitation of the PWFA lengths [93,102–106]. It was found to be the prevailing instability in the nonlinear regime, where $n_b > n_e$ due to the homogeneous focusing fields and thus homogeneous betatron frequencies (see also Ch. 4.2). Even though predicted by numerical simulations [106], the hosing instability has not been observed in high energy PWFA experiments [41,107,108].

Mitigation of the hosing instability was investigated in detail recently [109] and is based on the condition that for growth of the instability bunch slices have to oscillate at the same frequency. Any type of sufficient decoherence in the oscillations can lead to saturation and even damping of the instability by phase mixing of the oscillating particles [109]. Such decoherence can be provided by e.g. uncorrelated energy spread, a correlated energy spread along the bunch or by oscillation of bunch particles in wake regions of different transverse field [110,111].

4.1.3 Self-Modulation instability

While the hosing instability is also a type of transverse two-stream instability (TTS) [105], this section discusses axisymmetric modes of the TTS, in PWFA also referred to as *self-modulation instability* (SMI) [95,112]. These instabilities occur in bunches with lengths on the order of or longer than one plasma wavelength which therefore may partially fall into defocusing phases of the plasma wakefield driven by the bunch itself.
SMI has received much attention after it was proposed as a means to exploit the high energy of synchrotron-accelerated proton bunches to drive PWFAs over long distances and thus achieve high-energy witness bunches in a single acceleration stage [112,113].
The instability is caused by initial inhomogeneities in the focusing field of the plasma wake in the driver bunch. These lead to density modulations by inhomogeneous focusing, which amplify the field inhomogeneities, resulting in subsequent unstable growth [94,95]. After sufficient growth, the plasma electron current is flowing through the bunch, thereby creating large net negative charges, which subsequently defocus beam electrons, as illustrated in Fig. 4.2.

Growth and evolution of the instability were studied in detail analytically [112,114–117] and in numerical simulations [115,118,119]. It was found for longitudinally flat-top bunches that an initial seed perturbation is growing

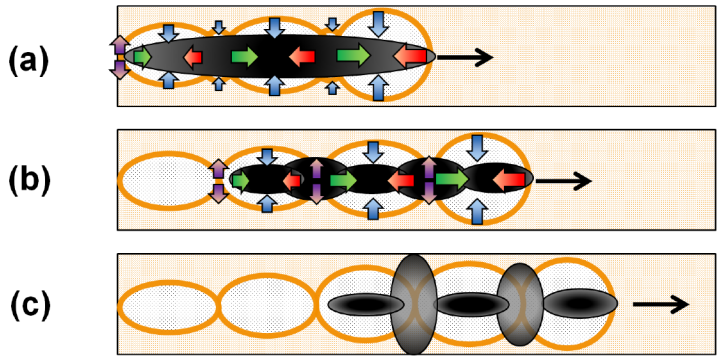

Figure 4.2: Schematic of the interaction of a long bunch with a plasma in the TTS-/SMI-regime. A long driver bunch (black) is driving a plasma wake with longitudinal (left/right arrows) and transverse (up/down arrows) forces (a). Inhomogeneities in the transverse forces (a) lead to inhomogeneous focusing (b). Plasma electrons (orange dots) are forming net negative charges within the bunch, where the bunch is defocused and focused bunchlets remain on axis (c).

exponentially with the number of e-foldings [117]

$$N = \frac{3^{3/2}}{4}(2|\zeta|k_\beta^2 z^2)^{1/3} \ , \tag{4.1}$$

where ζ is the longitudinal coordinate in the co-moving frame ($\zeta = z - ct$, i.e. position in bunch where SMI is observed) normalised to the plasma skin depth, z the longitudinal coordinate in the laboratory frame (i.e. distance traveled in the plasma) and k_β the wave number of the betatron oscillation of the beam electrons:

$$k_\beta = \frac{4\pi \frac{n_b}{n_e} e^2}{m_e c^2 \sqrt{2\gamma_b}} \ , \tag{4.2}$$

where n_b is the beam particle density, n_e the plasma electron density, m_e the electron mass, c the speed of light and γ_b the beam Lorentz factor. As the betatron oscillation length is usually on the order of mm to cm in a PWFA, the length of the accelerator would be severely limited by the SMI, as found in simulations [69,93,94]. Controlled seeding of the instability [95] would still lead to the loss of a substantial part of the driver particles and a reduction of the transformer ratio.

To mitigate the growth of the axisymmetric transverse instabilities in long bunches in a plasma, the bunch density has to exceed the unperturbed plasma density [67, 93, 120]. As this has major implications on the beam-plasma

interaction, first the nonlinear regime of PWFA will be introduced in the next section, before the beam transport of long driver bunches will be discussed further.

4.2 The nonlinear regime of PWFA

When the density of a driver bunch in a PWFA n_b exceeds the unperturbed plasma electron density n_p, linear theory does not correctly describe the wakefields anymore [54,120,121]. In the following sections the characteristics of the nonlinear regime of PWFA will be summarised and the implications on the transport of HTR-capable bunches will be discussed.

4.2.1 Characteristics

Nonlinear interaction in PWFA [120, 121] is separated further into two different regimes:

- the highly nonlinear, *bubble* or *blowout regime*
- the *quasi-nonlinear regime*.

To distinguish between the two, the normalised driver beam charge can be utilised, which was introduced to distinguish the highly nonlinear regime from the linear [122, 123]

$$\tilde{Q} = 4\pi k_p r_e N_b = \frac{N_b k_p^3}{n_e} \ , \tag{4.3}$$

where k_p is the plasma wave number, r_e the classical electron radius, N_b the number of bunch particles and n_e the plasma electron density. It describes the ratio of driver bunch electrons to plasma electrons in a cube with edge length of the plasma skin-depth.
If $\tilde{Q} \gg 1$ interaction is set in the blowout regime. Here all plasma electrons are expelled transversely by the driver bunch and a so-called bubble is formed, which is completely rarefied of plasma electrons. Due to the fields by the remaining, evenly distributed, positive ions, the transverse forces in the wake for electrons $F_r(r) = -2\pi e^2 n_e r$ [124] are linearly focusing and independent of the longitudinal position inside the bubble. No dependency of the accelerating fields on the transverse position is present, as opposed to

Eq. (2.29). Plasma electrons in nonlinear PWFA can reach relativistic velocities. These high energy plasma electrons oscillate at different frequencies than the plasma frequency due to the relativistic mass increase [compare mass dependence in Eq. (2.11)]. This first leads to the change of the wakefield shape from sinusoidal to sawtooth-like and second to a dependence of the length of the plasma bubble on the amplitude of the wakefield and thus the driver density (driver current in the strong blowout). Another feature of the bubble regime is the so-called wave-breaking and trapping of plasma electrons in the plasma wake [125,126]. The acceleration of plasma electrons, which reach velocities close to the phase velocity of the wake, allows to form bunches from plasma electrons and production of short, high-brightness electron beams [127] but can also lead to dark current [128]. In PWFA this is mainly an issue in cases of strong longitudinal plasma density inhomogeneities due to the wake phase velocity, i.e. the driver velocity, being close to c .
Various analytical descriptions of the nonlinear regime have been presented [121, 129, 130] whereas many can only be solved numerically for arbitrary driver bunch shapes. A simple approach is to assume the plasma to be a multi-mode medium, with a frequency spectrum depending on the density perturbation n_b/n_e [131, 132]:

$$E(\zeta) = n_e \frac{e}{\epsilon_0} \int_0^{\zeta} \sum_{m=1}^{\infty} \frac{m^m}{2^{m-1} m!} \left(\frac{n_b}{n_e}\right)^m cos(m k_p \zeta') d\zeta' \ . \tag{4.4}$$

From this point of view it is also evident, that the fundamental theorem of beamloading, derived in Sec. 3.1 under the assumption of a single-mode medium, does not apply to the nonlinear regime interaction. Hence, TRs above 2 are possible for symmetrical bunches in the nonlinear regime [54,121] but have not been measured to date [133].
The blowout regime has been shown to provide very high acceleration gradients [41, 108, 134] and is considered the favourable regime for a PWFA for electrons, due to the linear focusing fields and transverse homogeneous acceleration.

If $\tilde{Q} \lesssim 1$ but $n_b > n_e$ the interaction is set in the quasi-nonlinear regime [80]. In this regime favourable characteristics of the bubble-regime (e.g. linear focusing) are maintained, while the fields behind the driver bunch do not exhibit a strong nonlinearity or wave-breaking. Therefore, resonant excitation of wakefields is possible, which is not the case in the blowout regime. Operation in the quasi-nonlinear regime was hence proposed to solve

certain issues of bunch train driver scenarios for high transformer ratio PWFA discussed in Sec. 3.2 [80].

4.2.2 Beam transport in the nonlinear regime

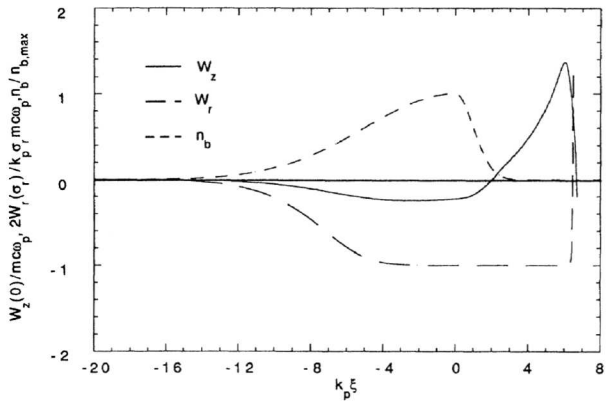

Figure 4.3: Numerical solution of on-axis wakefields in the nonlinear regime for a HTR capable bunch. Particles are moving to the left. The small dashed line shows the particle density, the long dashed line the transverse fields and the solid line the longitudinal fields [120]

Figure 4.3 shows a calculation of wakefields in the nonlinear regime of PWFA. The maximum beam density is equal to the plasma density and the length of the driver beam is $\sim \lambda_p$. Transverse fields W_r show that the full bunch is in the focusing phase of the wakefields and in the second half of the bunch the transverse fields are constant. This is different to the linear regime [compare Fig. 3.2(b)] and prevents variations in the wakefield strength which can lead to instability (see Sec. 4.1.3). Therefore the bunch can be transported through the plasma stably even though its length exceeds the length of the focusing phase of the plasma wake, which is $\lambda_p/2$.
The linear character of the transverse fields allows to preserve the beam quality of a witness bunch, as no nonlinearities are introduced to its phase space. As already mentioned, the length of the wake can depend on the driver density. This can lead to phase variation at the witness beam position when e.g. betatron oscillations within the driver cause driver density variations along the plasma. As the maximum accelerating fields are at the back of the wake, close to the strongly defocusing phase of the transverse fields, this can quickly lead to loss of the witness bunch [135].

Chapter 5

Numerical simulations

Previous chapters have discussed analytical and phenomenological descriptions of classical accelerators and PWFA. As the complex particle dynamics in the longitudinal and transverse fields in accelerators can only be described analytically for certain ideal cases, usually numerical simulations are employed. These allow to accurately calculate the dynamics of realistic field and particle distributions. Every simulation code is based on an idealised physical model and makes certain assumptions to solve the equations associated with this model. To achieve reliable results, choosing the right codes, i.e. not violating the assumptions the codes are based upon with the physics of the processes under study, is essential.
In classical accelerator physics various simulation codes have been developed. Among the most commonly used are MAD-X [136], elegant [137] and ASTRA [138]. While the former ones are not considering collective, i.e. interparticle effects like space charge forces between bunch particles, the latter also models these effects and is therefore most suitable for the rather low beam energies and high bunch charge densities encountered in the present work. An introduction to ASTRA will be given in the next section.
For modeling PWFA, a variety of simulation codes has evolved throughout the last years. Widely used codes are Warp [139], OSIRIS [140, 141], LCODE [142, 143], QuickPIC [144] and HiPACE [145]. Due to its fast performance and efficient parallelisation the latter was used for the PWFA simulations conducted during the course of the presented studies. A brief introduction to the theoretical background of HiPACE will therefore also be provided in one of the following sections.

5.1 Particle tracking with ASTRA

A space charge tracking algorithm (ASTRA) [138] is a code developed for modeling low energy beam transport in photo-injector linacs (see also Ch. 6). It is a so-called particle tracking code, i.e. it numerically solves the differential equations of motion for individual particles for given external transverse and longitudinal magnetic and electric field distributions. To reduce the amount of necessary numerical calculations beam particles are summarised in so-called macroparticles. Each macroparticle represents e.g. 10^3–10^5 electrons and their use is justified by the assumption that particles which are close to each other will experience similar forces and therefore have similar trajectories in the phase space.
In addition to external fields ASTRA also involves routines to calculate the space charge forces between the particles in a bunch. This is done by subdivision of the volume occupied by beam particles into a grid of sub-cells. The grid can either be 2D or 3D, depending on whether only rotationally symmetric forces are expected or not. Fields induced by the space charge of the (macro-)particles are calculated on this grid for the sum of all particles in each grid cell: the system is Lorentz-transformed into the average rest frame of the bunch, fields on the grid are calculated by solving the Poisson equation and the system is transformed back to the laboratory frame. The resulting map of the space charge fields is then included into the equations of motion of the macroparticles.
As input for the simulation an initial particle distribution, field maps and parameters for all accelerating cavities and magnets, parameters of the calculation (e.g. space charge grid parameters) and the parameters for data output are needed. In the present work, usually $5 \cdot 10^5$ macroparticles were used. 2D space charge calculation was used until after the last accelerating cavity, where the first quadrupole magnets are located (see also Ch. 6). As these have non-rotationally symmetric magnetic fields, 3D space charge calculation was used for modeling the rest of the linac. The grid size for space charge calculation was defined in convergence studies as 64×16×16 cells (z-x-y).

5.2 HiPACE PWFA simulation

Numerical simulations have become an indispensable tool for understanding and developing plasma accelerators. In addition to the complex dynamics, which make simulations an essential tool for conventional particle

accelerators, plasma wakefield accelerators are much more difficult to access with diagnostics experimentally. To model beam-plasma interaction, usually the PIC method is applied.
In this approach, the simulated system is divided into a 3D grid of sub-cells. The differential equations of motion of the simulated particles are solved for fields which are calculated on this grid. This is done for the beam macroparticles as well as for the plasma macroparticles. In plasma wakefield applications usually no external fields are included in the calculation, as they are not present or negligible compared to the field strengths in the plasma wake.
In the calculation loop of one time step of the simulation first the current densities of the macroparticles are distributed between the closest grid points. After the current density on the grid is calculated, conventional (also called *fully-explicit*) PIC codes numerically solve the time-dependent Maxwell equations [Eqs. (2.3) and (2.4)]. Magnetic and electric fields are calculated on the faces and edges of the grid cells, respectively, for full and half integer time steps [146]. Afterwards the fields at the particle positions are interpolated between the field calculation points and the equations of motion can be solved. The numerical stability of this method depends on the time step size via the Courant-Friedrich-Lewy condi-

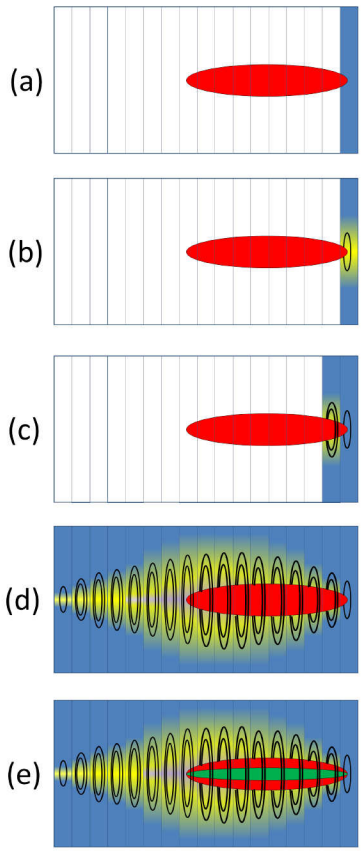

Figure 5.1: Illustration of quasi-static PIC time step: a slice of plasma (blue/yellow) is introduced to the beam (red) (a)]. Fields (black lines) are calculated and plasma particles evolved (b). Plasma slices are moved (c) and process is repeated until the full field map is acquired (d). Finally the beam particles are pushed (green) (e) and the next beam time step can be calculated.

tion [146, 147]: $\Delta t = C_{CFL}\frac{\sqrt{\Delta x^2+\Delta y^2+\Delta z^2}}{c}$ where $C_{CLF} < 1$, i.e. no particle may cross more than one grid cell diagonally. By this condition the maximum time step size is fundamentally linked to the grid cell size. In simulations of PWFA the features that have to be resolved (e.g. wakefield structure) can be very small, while the length of a PWFA can span up to meter sizes. Due to the maximum time step limitation this leads to PIC simulations which consume large amounts of computational resources.
To resolve this issue, the so-called *quasi-static* approach was introduced to PWFA simulations [148, 149]. When the driver beam does not evolve significantly during the transit of a plasma electron, one can decouple the plasma and beam time scales. This is equal to the betatron wavelength λ_β of the beam being much larger than the plasma wavelength λ_p, e.g. $\lambda_\beta = \sqrt{2\gamma_b}\lambda_p$ [150] in the linear focusing of nonlinear PWFA with usually $\gamma_b \gg 10$. This typically allows orders of magnitude longer simulation time steps and corresponding reduction of calculation time. Instead of evolving the fields from time step to time step by explicitly solving Maxwell's equations, the field maps are constructed self-consistently in each time step by moving a slice of plasma along the beam and evolving the particles and corresponding fields in this slice. The process is illustrated in Fig. 5.1. On the one hand this means that the entry into a plasma and plasma density inhomogeneities on length scales similar to the bunch length cannot be simulated (as in every time step the beam is initialised fully surrounded by plasma constructed from one plasma slice). On the other hand it e.g. allows to import beam particle distributions from other PIC codes for further simulation.
HiPACE (*Highly efficient Plasma ACelerator Emulation*) is based on this quasi-static approach. It also employs fast Poisson-solvers for field calculation to reduce simulation time even further. Fields at the boundaries of the simulation box are assumed to be zero, i.e. perfectly conducting walls. The size of the time steps can automatically be adjusted depending on the beam particle energies and maximum plasma density perturbation. Typical simulations in this work were conducted with a z-x-y grid of $512\times256\times256$ cells, which was determined by checking the convergence of the simulation results with increasing grid cell number for the simulation boxes of around $11\times1.5\times1.5\,\mathrm{mm}^3$ size (depending on exact beam parameters and plasma densities). Such a simulation usually finished within a few hours using 32 or 64 parallel processors. This rather short run time even allowed for limited parameter scans to conduct error studies and to reconstruct measurement results (see also Sec. 8.4 and Ch. 10).

Part II

High transformer ratio plasma wakefield acceleration at PITZ

After introducing the theoretical basis of high transformer ratio PWFA in the first part, this second part will now give details about the experimental environment at PITZ and present the results that have been achieved in the course of this work.
It is structured as follows:

- In Ch. 6 the PITZ facility, where experiments have been conducted, will be introduced.
- Chapter 7 describes the work that has been done on production of HTR-capable electron bunches via photocathode laser pulse shaping and prospects of the method.
- Gas discharge plasma physics and the gas discharge plasma cell, that was developed for the HTR PWFA experiments, are introduced in Ch. 8.
- The beam dynamics simulations, that have been carried out to identify favourable electron beam and plasma parameters for experiment are described in Ch. 9.
- Chapter 10 finally concludes with the description of the first observation of and further experimental results on HTR PWFA which have been achieved in the course of this work.

Chapter 6

The PITZ facility

The experimental work for the demonstration of high transformer ratio PWFA has been carried out at the **P**hoto-**I**njector **T**est facility at DESY in **Z**euthen (PITZ) [151, 152]. In the following sections, the general principle of photoinjectors will be introduced before a detailed description of the PITZ electron source and the beamline layout will be given.

6.1 Photoinjection radio frequency accelerators

Various applications of high energy electron beams like X-ray free-electron lasers and PWFA demand for high beam brightness. The brightness is defined as

$$\mathfrak{B} = \frac{I}{\epsilon_{n,x}\epsilon_{n,y}\epsilon_{n,z}} \ , \tag{6.1}$$

where I is the bunch current and $\epsilon_{n,x/y/z}$ are the normalised emittances of the particle bunch in all three dimensions [153]. To produce bunches with $\mathfrak{B} \sim 100\,\frac{A}{(mm\,mrad)^2}$ usually electron sources based on the extraction of electrons from a cathode via the photoelectric effect [154] are employed. The cathode is illuminated with a high intensity ($\sim \frac{10kW}{mm^2}$), short ($\sim$ ps), ultraviolet (UV) laser pulse. Due to their space charge, the extracted electrons repel each other, which leads to divergence and blow-up of the extracted bunch both transversely and longitudinally. To reduce the bunch quality degradation due to the space charge forces, the photocathode is placed inside an RF accelerating cavity, also called electron gun. Bunch electrons are accelerated immediately after extraction by the cavity fields. The quicker the electrons

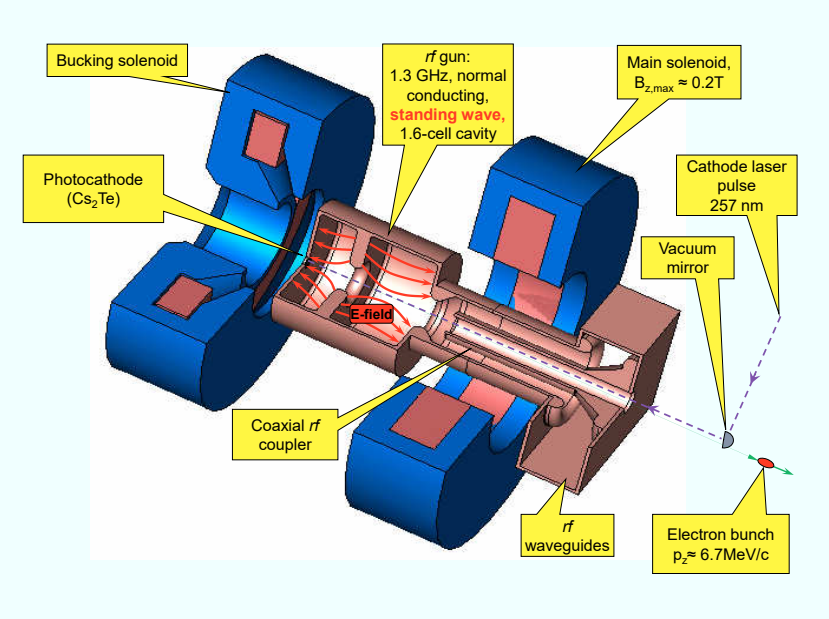

Figure 6.1: Schematic of the PITZ photoelectron gun.

reach relativistic energies (i.e. the higher the accelerating fields at the cathode) the lower the contribution of the space charge to the bunch emittance. To focus the divergent bunches, solenoid focusing magnets are placed around the electron gun. This also allows to compensate the emittance growth due to varying rotation of longitudinal bunch slices in the transverse phase space during acceleration [155]. The intrinsic emittance that the electron bunches exhibit due to the transverse spot size of the photocathode laser pulse and the (arbitrarily directed) momentum caused by the difference between the work function of the photocathode material and the laser photon energy is referred to as *thermal emittance*.

6.2 PITZ facility layout

The PITZ accelerator was built for development and commissioning of the electron sources for the FEL user facilities FLASH [156] and European XFEL [157]. Therefore, the electron gun is the core part of the $\sim 20\,\mathrm{m}$ long beamline.

6.2.1 PITZ electron gun

The PITZ gun cavity is a normal conducting, standing wave, 1.6 cell RF cavity, with a resonance frequency of 1.3 GHz (L-band). Its nominal RF time structure is the same as the pulse time structure of the aforementioned European XFEL user facility: 1.3 GHz RF pulses of up to 650 µs length with a repetition rate of 10 Hz. The cavity cell at the photocathode is 0.6 half RF wavelengths long, to increase the electric field at the cathode during electron emission and to compensate the phase slippage of the electron bunches during acceleration at low particle energy after emission. To provide high bunch charges at moderate photocathode laser pulse energy, a central spot of 5 mm diameter of the molybdenum photocathode is coated with Cs_2Te. This material has been shown to provide high quantum efficiency (QE), i.e. a few percent electron yield per incident UV photon, at low thermal emittance (thermal energy $E_{k,th} \approx 0.55$ eV [158]). Due to the long RF pulse length the input RF power is limited by the average thermal load on the cavity and vacuum breakdown. At the nominal power of 6.5 MW a maximum electric field of 60 MV/m is reached at the photocathode. Bunches accelerated at the maximum mean momentum gain (MMMG) phase leave the gun with a mean momentum of about 6.7 MeV/c.
The cavity that was installed during the experiments conducted in this work was Gun 4.6. A schematic drawing of the gun setup is shown in Fig. 6.1.

6.2.2 MBI photocathode laser

The photocathode laser that was used for the present studies was developed and supplied by the Max Born Institute (MBI) [159]. A schematic layout is shown in Fig. 6.2. It consists of a mode-locked, ytterbium-doped potassium gadolinium tungstate (Yb:KGW) laser oscillator, which supplies Gaussian laser pulses of 1032 nm wavelength with an RMS length of ~ 0.4 ps at a repetition rate of 54 MHz. Every 54th pulse is transported to the pulse shaper, which is discussed in detail in Ch. 7. After shaping, the low energy pulses are amplified by a factor of $\sim 10^5$ in the ytterbium-doped yttrium aluminium garnet (Yb:YAG) regenerative amplifier. Due to the lower spectral bandwidth of this gain medium the Gaussian laser pulse length is increased to ~ 0.8 ps RMS and the central wavelength is shifted to 1030 nm. Subsequently, the final infrared (IR) pulse energy of ~ 20 µJ is reached after further amplification in the two-stage Yb:YAG booster amplifier. In the downstream lithium triborate (LiB_3O_5, "LBO") and barium borate (BaB_2O_4, "BBO") crystals

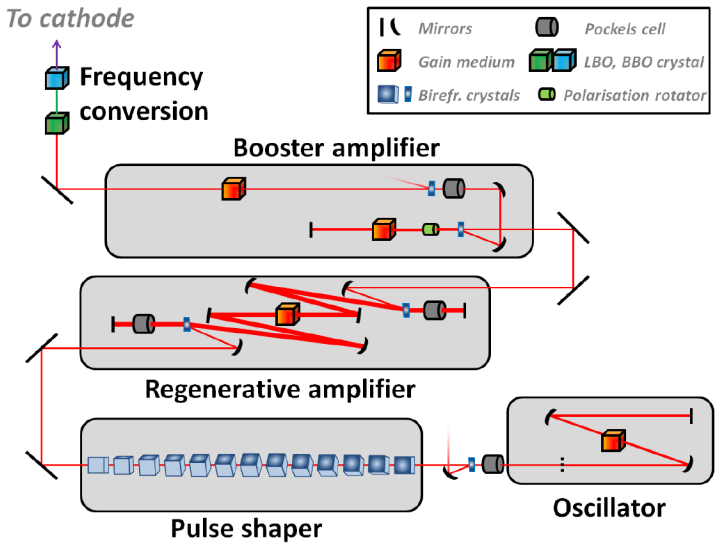

Figure 6.2: Schematic layout of the MBI photocathode laser system at PITZ.

the IR pulses are frequency-doubled twice to provide UV laser pulses with a pulse energy of up to 4 µJ.
Before the laser pulses reach the cathode, a variable transverse beam shaping aperture (BSA) allows to adjust the transverse spot size of the pulses on the photocathode, i.e. initial transverse bunch size. A camera placed at an optically equivalent position is used to observe the transverse distribution on the cathode.

6.2.3 PITZ beamline

The layout of the PITZ beamline is depicted in Fig. 6.3. Downstream of the photoelectron gun the PITZ beamline contains various beam transport elements, diagnostics, a second accelerating and a deflecting cavity, which allow for flexible manipulation and detailed characterisation of the PITZ electron beams.

Charge measurement

Bunch charges can be measured using Faraday cups upstream of the booster cavity. As this method of collecting the bunch electrons in a massive copper block is invasive and difficult to realise at high energies due to the long penetration depths, parasitic bunch charge measurement using Integrating

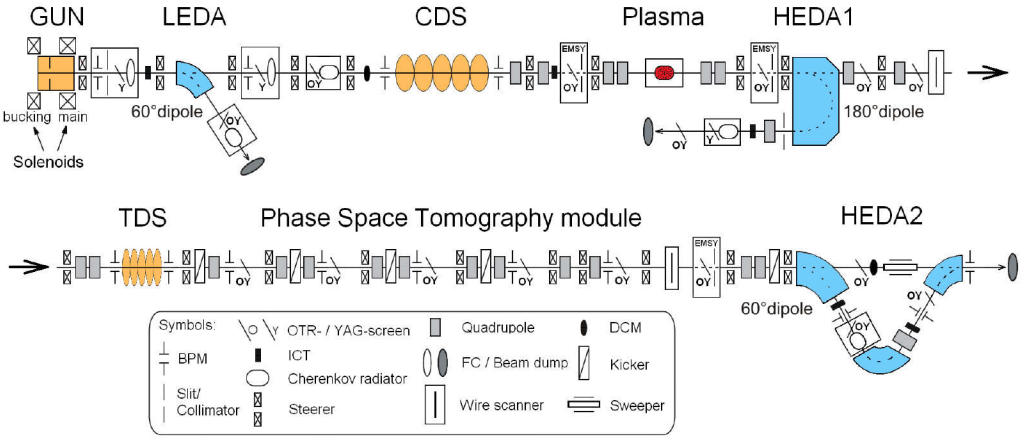

Figure 6.3: Schematic of the PITZ beamline [161].

Current Transformers (ICT) [160] are available at low and high beam energies.

Screen stations

At various positions, scintillator screens can be inserted into the beamline to observe the transverse profile of the electron beam. The standard scintillator material at PITZ is cerium-doped yttrium aluminium garnet (Ce:YAG). Preparatory experiments for high transformer ratio measurements revealed that the low charge witness bunches are hardly resolvable on these screens due to their low light yield. For higher light yield, cerium-doped lutetium yttrium orthosilicate (LYSO) scintillators were installed at few screen stations for this work. Charge coupled device (CCD) cameras are used to record the light emitted from the scintillator screens.

Booster cavity

To increase particle energies and thus reduce space charge effects within the bunches, a second accelerating cavity is installed at PITZ. It is a standing wave, normal conducting, 1.3 GHz structure, based on the cut-disk design [162]. The booster cavity accelerates the electron bunches up to ~ 25 MeV final energy.

Transverse deflecting structure

Screen stations in the beam path only allow to measure time projected values of the bunch particle distribution. Information such as bunch length, energy distribution along the bunch or the phase space of single longitudinal slices are not accessible using simple scintillators. Therefore, a transverse deflecting structure (TDS) was included into the PITZ accelerator [163, 164]. This cavity accelerates particles in transverse direction to the beam axis, i.e. deflects them depending on their longitudinal positions: when the bunch centre passes the cavity close to the zero crossing phase of the RF wave, bunch particles experience a nearly linear correlation between their longitudinal position within the bunch and the experienced transverse deflection. On a subsequent screen, the longitudinal position of incident electrons can then be deduced from the transverse position of the particles in the deflection plane. At PITZ the TDS is a normal conducting, traveling wave cavity with an RF frequency of 2.997 GHz, which deflects in the vertical plane. The higher RF frequency compared to the other PITZ cavities results in an increased time dependence of the deflection gradient close to the zero crossing phase and thus higher longitudinal resolution at constant maximum field amplitude.
Several sources of systematic errors have to be considered in TDS measurements:

- A momentum spread is induced on the deflected bunch due to the longitudinal fields being non-zero at off-axis positions in the cavity.
- The deflection is chromatic, i.e. the deflection angle depends on the longitudinal momentum of deflected particles, which has to be corrected for beams with high energy spreads.

A maximum achievable temporal resolution of 100 fs was simulated for the PITZ parameters [165].

Dipole spectrometers

Dipoles and adjacent dispersive sections with screen stations are used to measure the energy of the electron bunches. Three such sections are installed at PITZ: the low energy dispersive arm (LEDA) directly after the gun, and two high energy dispersive arms (HEDA1 [166], HEDA2 [167]) downstream the booster cavity. While the first two dispersive sections are deflecting the beam vertically, HEDA2 is deflecting in the horizontal plane. Together with

the vertically deflecting TDS cavity this allows for single-shot longitudinal phase space measurements of the electron bunches.

Chapter 7

(Sub-)Picosecond electron bunch shaping

One of the main prerequisites for the demonstration of HTR PWFA at PITZ was the production of HTR-capable electron driver bunches. As longitudinal bunch shapes in photo-injectors are usually symmetric, dedicated bunch shaping is necessary to produce bunches similar to those introduced in Sec. 3.2. In the following sections, existing bunch shaping methods are briefly reviewed and the method that was employed in the course of the present work is described in detail. The description is based on the results published in Ref. [168].

7.1 Established bunch shaping methods

As introduced above, achieving high transformer ratios in wakefield accelerators at high acceleration field amplitudes necessitates high peak-current driver bunches of femtosecond to picosecond lengths with triangular longitudinal profiles. Several methods have been developed to produce such bunches, each method having advantages and drawbacks.

Masked dispersive transport lines

In the context of creating trains of short-spaced microbunches, it was proposed to absorb parts of an electron bunch in a dispersive section [169]. For that purpose, a linear correlated energy spread (*chirp*) is introduced to the bunch by off-crest acceleration (bunch timing offset to the phase of maximum

energy gain) of the bunch in a linac. At a low-beta-function position in a

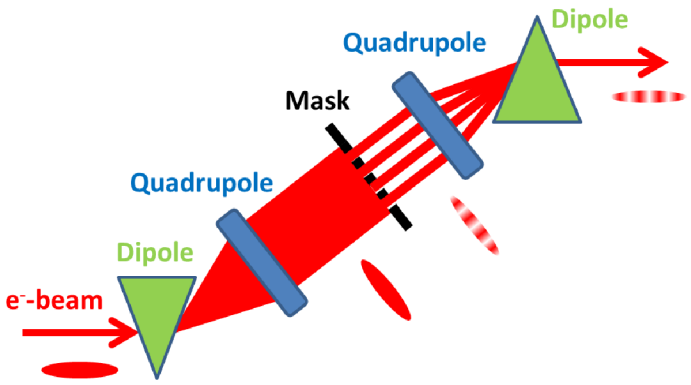

Figure 7.1: Schematic of the dispersive masking technique (cf. [170]).

magnetic chicane beamline, a bulk metal mask then either decelerates and scatters or even absorbs part of the energy spectrum of the bunch. Due to the time-energy correlation this leads to longitudinal shaping of the bunch when the dispersion is closed again downstream of the chicane, as illustrated in Fig. 7.1. This method was verified experimentally [170] and extended to creating triangular bunches [171].
Nevertheless, the method only allows to produce a set of fixed shapes with low degree of freedom in dispersion, energy spread and beta-function at the mask position. Depending on the desired parameters, a major part of the original bunch charge is lost in the shaping process. Hence, very high initial bunch charges would be necessary to reach the target peak currents, setting further constraints on the electron source and possibly leading to high radiation levels around the shaping chicane.

Nonlinear chromatic shaping with sextupoles

Another successfully demonstrated method of longitudinal bunch shaping is based on manipulation of quadratic and higher order correlations between energy and longitudinal position in a magnetic chicane using sextupole magnets [172]. A nonlinear energy correlation is introduced to the longitudinal phase space of the bunch in an upstream accelerating cavity. The bunch is then injected into a chicane similar to the one shown in Fig. 7.1 (also referred to as *dogleg*), which additionally includes two sextupole magnets. These sextupoles allow to eliminate the second order coefficient in the transfer matrix

between particle energy and longitudinal position. Since the linear term can be non-zero, the chicane can be employed for compression of the bunches simultaneously. Despite the successful demonstration of the method [173] its application suffers from the fact that the transverse phase space is coupled to the longitudinal phase space in the longitudinal shaping process, thereby distorting the transverse bunch profile. Furthermore, the method again only allows limited tunability of the produced bunch shapes.

Dual frequency linac bunch shaping

Based on a similar principle, it was demonstrated that longitudinal shaping can be achieved by introducing nonlinearities to the longitudinal phase space of an electron bunch and consequently compressing such a bunch in a magnetic chicane [174]. The magnetic bunch compressor was also suggested to be substituted by velocity bunching [175] to circumvent distortion introduced by interaction of the bunch in the magnetic compressor with its own coherent synchrotron radiation (so-called *CSR effects*).
Bunch shapes are limited to different ramped profiles with some degree of freedom on the exact parameters by tuning the amplitudes and phases of the two linac components of different frequencies. A higher harmonics cavity has to be installed in the beamline for this method to be applied.

Shaping by self-wakefields

Similarly, the high harmonic frequency contribution to the longitudinal phase space of the bunches can be provided by the bunch interacting with its own wakefield in a dielectric waveguide [176]. As the longitudinal phase space modification is imprinted purely passively, this method has a significantly reduced footprint. Nevertheless the shapes are also limited to ramped profiles with limited tunability.

Transverse-to-longitudinal emittance exchange

Exchanging the transverse and longitudinal phase space was proposed as a method to provide electron bunches with reduced transverse emittances compared to the direct utilisation of bunches from photo-injectors [177, 178]. To achieve this phase space exchange, a transverse deflecting cavity surrounded by two identical dogleg chicanes is utilised.
By shaping the transverse profile via masks or collimators upstream of the

emittance exchange (EEX) beamline, this technique can also be employed for longitudinal bunch shaping [179, 180]. Successful demonstration [181] and subsequent application of the method led to the first demonstration of high transformer ratio acceleration using asymmetric driver bunches in a dielectric wakefield accelerator [70].
EEX shaping enables some flexibility in the produced bunch current distributions but is still limited to the installed transverse masks. Transverse distortions have also been reported, which are caused by transverse-to-longitudinal correlations originating upstream of the mask [181]. An EEX beamline is complex due to the deflecting cavity that is an integral part of the method. Furthermore, additional effort has to be made to control space charge and higher order effects in the EEX beamline, in order to reduce distortions in the longitudinal bunch profile [182, 183]. This increases the complexity and size of the EEX setup further. The involved transverse shaping also again leads to high charge losses and potentially high radiation levels, especially at high bunch repetition rates.

7.2 Photocathode laser based bunch shaping

Due to the constraints at the PITZ facility, where none of the established shaping concepts is available, an alternative bunch shaping method was developed. Shaping of bunch current profiles by shaping the photocathode laser pulses was already considered and partially realised in multiple studies on photo-injectors [159, 184–186]. First considerations on using this method for ramped bunch profiles were conducted without studying experimental implementations [68]. In the course of the present study, high transformer ratio capable bunches were produced for the first time with photocathode laser based bunch shaping by extending the existing bunch shaping capabilities of PITZ [159].

7.2.1 Triangular pulse shaping by Šolc fan filter

Working principle and implementation

Photocathode laser pulse shaping at PITZ is currently based on a so-called *Šolc fan filter* [159]. This setup consists of an input polariser, a series of N birefringent crystals and an output polariser of the same polarisation direction as the input. The n-th birefringent crystal is rotated by an angle θ

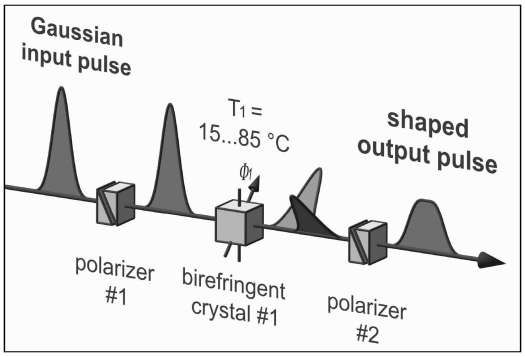

Figure 7.2: Illustration of Šolc fan filter shaping [159].

of

$$\theta = 45°/N \cdot (2n-1) \ , \tag{7.1}$$

to the polarisation direction of the incoming laser pulse [187]. A short, linearly polarised, Gaussian laser pulse is delivered to the pulse shaper by the laser oscillator (the MBI laser oscillator at PITZ e.g. delivered a laser pulse with ~ 0.4 ps RMS length during the course of this work, which was stretched to ~ 0.8 ps RMS in the amplifier and frequency conversion stages of the laser system downstream of the pulse shaper; see also Sec. 6.2.2, Figs. 6.2 and 7.5). This pulse is split into 2^N Gaussian pulses in the Šolc fan filter. These (virtual) pulses add up to a laser pulse of flexible temporal shape. Fine-tuning of individual crystal angles allows to change the pulse shape to almost any combination of $N+1$ virtual Gaussian pulses. The technique is illustrated in Fig. 7.2.

A Šolc filter comprising 13 YVO_4 birefringent crystals of 2.7 mm length was implemented at PITZ for emittance optimisation [152]. Crystal orientation can be controlled remotely within a $\pm 10\,°$-range. Every crystal introduces an additional delay of 2 ps to the extraordinary polarisation direction. This delay and the resulting phase of the output pulses was fine tuned once by temperature adjustment of every crystal between 15 °C and 85 °C in a single crystal setup. Nevertheless, it was found experimentally that the delay of certain virtual pulses is influenced by rotation of adjacent crystals in a multi-crystal arrangement, which might indicate improper phase matching of the crystal lengths. Experimental validation of the crystal temperatures may resolve this issue in future measurements.

As described in [159] the pulse shaping inherently leads to significant losses

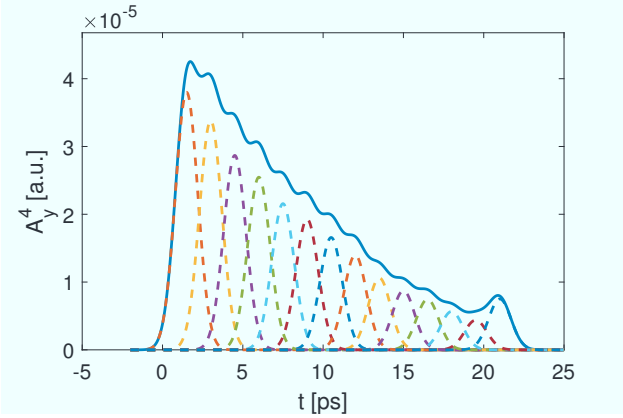

Figure 7.3: Simulated double-triangular laser pulse shape resulting from the PITZ Šolc fan filter. The dashed lines of varying colour show the single Gaussian pulses, which form the overall pulse shape (solid blue line).

of laser pulse energy, as the pulse is shaped by filtering the spectrum of the short Gaussian input pulse to the spectrum of a long output pulse. Losses can exceed 90 % of the input laser pulse energy. A regenerative amplifier after the pulse shaper is used to compensate for these losses in the PITZ photocathode laser system.

Bunch shaping simulations

To assess the capabilities of the existing PITZ pulse shaper, the output of the shaping process was calculated numerically with the following simplified model. Every pulse is represented by a vector $\mathbf{V}$ with entries of its position p in the macropulse, its crystal of origin O (first crystal that contributes to the pulse position) its intensity in ordinary and extraordinary polarisation direction $A_{y/x}$ (w.r.t. the input polariser) and the relative phase of the extraordinary polarisation direction ϕ:

$$\mathbf{V} = \begin{pmatrix} p \\ O \\ A_x \\ A_y \\ \phi \end{pmatrix}. \tag{7.2}$$

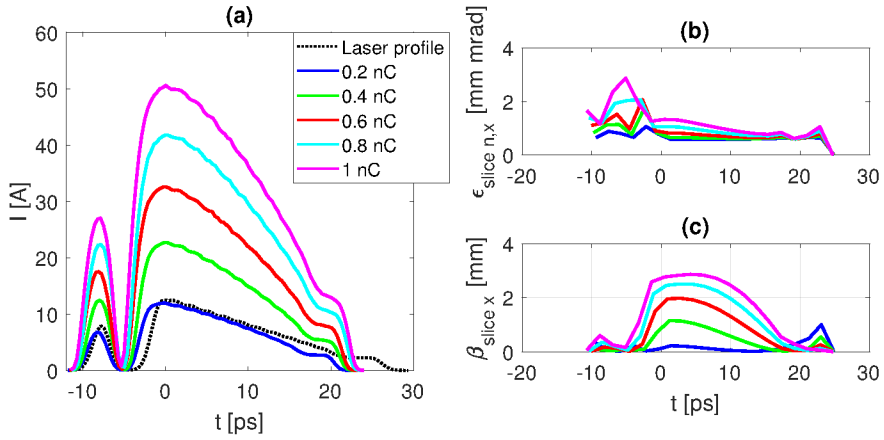

Figure 7.4: Simulated bunch current (a), normalised slice emittances (b) and slice-β parameter for a doorstep-like laser pulse profile and different total bunch charges at the PITZ plasma cell entrance.

The influence of every of the N crystals is calculated for every virtual pulse position, starting at crystal number O by

$$\mathbf{V}' = \begin{pmatrix} 1 & 0 & 0 & 0 & 0 \\ 0 & 1 & 0 & 0 & 0 \\ 0 & 0 & cos(\theta) & -sin(\theta) & 0 \\ 0 & 0 & sin(\theta) & cos(\theta) & 0 \\ 0 & 0 & 0 & 0 & 1 \end{pmatrix} \times \begin{pmatrix} p \\ O \\ A_x \\ A_y \\ \phi \end{pmatrix} + \begin{pmatrix} 0 \\ 0 \\ 0 \\ 0 \\ \Delta\phi \end{pmatrix}, \tag{7.3}$$

where $\Delta\phi$ is the phase difference introduced by the crystal to the extraordinary polarisation direction, which is ideally zero. The resulting ordinary polarisation pulse intensity A_y distribution is quadrupled to account for the two frequency-doubling stages of the photocathode laser (compare Fig. 6.2), which both exhibit an approximately quadratic dependence of output to input intensity.
A simulation of an approximately double-triangular pulse is shown in Fig. 7.3. The maximum deviation from the ideal Šolc angles given in Eq. 7.1 is 7 ° and the calculated pulse energy loss for the shown pulse shape is approximately 80 %, which can easily be compensated by the regenerative amplifier.
ASTRA simulations were conducted to quantify the distortions of the current profile of a bunch extracted with such a laser pulse due to external and space charge related fields in the accelerator. As shown in Fig. 7.4 (a), bunches with a triangular bunch shape were found to be achievable at the plasma cell

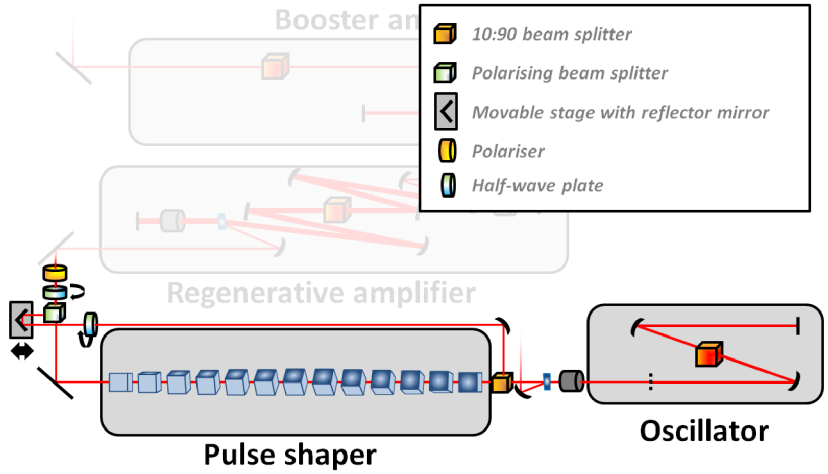

Figure 7.5: Layout of the witness bunch bypass beamline at the PITZ photocathode laser (compare to Fig. 6.2).

position. The reduced length of the electron bunches compared to the laser pulse profile results from velocity bunching at low particle energies.

Witness bunch addition

To be able to measure the wakefields created by the triangular driver bunches, a witness bunch had to be supplied at the plasma cell. This witness bunch was created directly at the photocathode by splitting the Gaussian laser pulse of the laser oscillator with a 10:90 beam splitter and recombining the two beams downstream of the pulse shaper. The beamline layout is shown in Fig. 7.5. Changing the relative path-lengths of the two beams with a remote-controlled, movable stage in the witness bypass line allowed to adjust the delay between driver and witness bunches. A half-wave plate in the witness beamline was used to align the polarisation of the witness pulse such that it is reflected onto the driver pulse trajectory by the recombining, polarising beam splitter. After recombination, the polarisations of the pulses are rectangular to each other. Utilising another half-wave plate, the fraction of light that is not absorbed in the final polariser, i.e. the charge ratio of driver and witness bunches, can be adjusted by rotating the polarisations of the two pulses with respect to the polarisation direction of the polariser.
Relevant offsets between the two bunches at the cathode due to misalignment of the laser beams are excluded, first by the long path-length from the point of

realignment to the cathode of several ten meters with several apertures of only a few ten micrometers diameter in between and second by equal transverse cutting of the beams at the beam shaping aperture, which is imaged to the cathode.

Experimental results

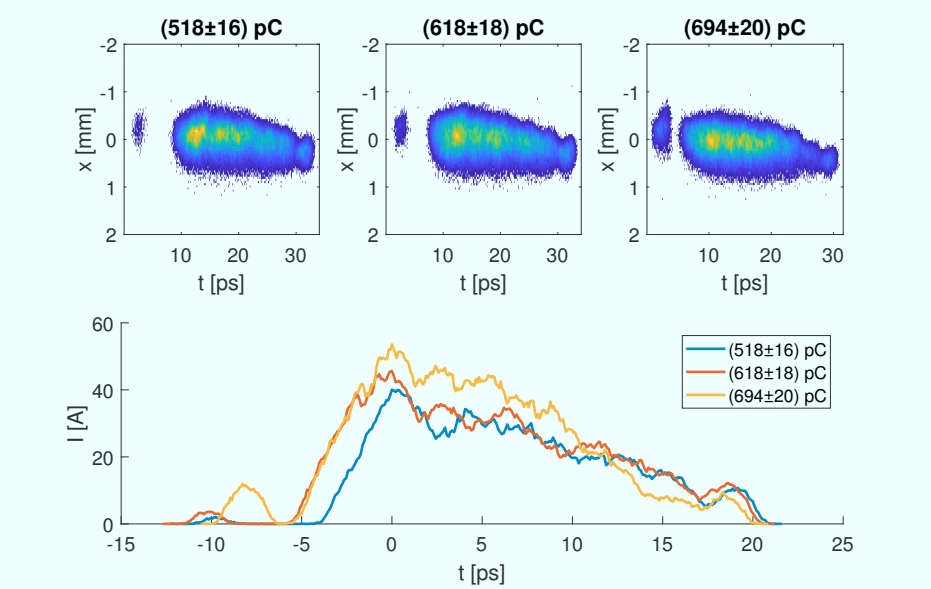

Figure 7.6: Measurement of three different triangular bunches with varying total charge, pulse shaper settings and driver-witness delay.

Due to the non-availability of longitudinal laser pulse diagnostics during the time of this work, shaping parameters were adjusted directly on the electron bunch shape, which was measured in the high energy section of PITZ using the transverse deflecting cavity and a subsequent scintillator screen. Bunch charges were kept at around 100 pC to reduce bunch shape distortions by space charge, while keeping a good signal to noise ratio for the longitudinal bunch shape measurement. Pulse shaper parameters were tuned manually and utilising a multi-dimensional optimisation routine based on the Nelder-Mead algorithm [188]. The difference between the measured and the target bunch profile was used as a goal function, which was minimised by the algorithm through variation of the crystal angles. Manual tuning was still necessary as the algorithm often terminated in local minima of the bunch profile optimisation and furthermore tended to suppress virtual

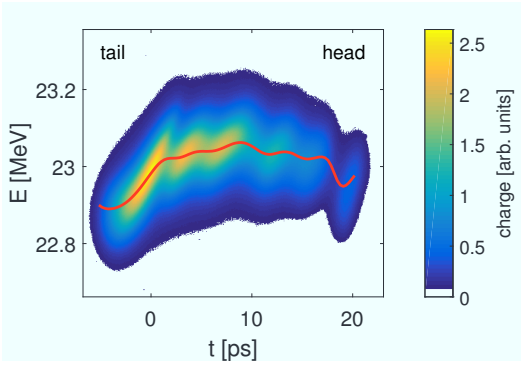

Figure 7.7: Exemplary longitudinal phase space of the triangularly shaped bunches. The red line shows the slice mean energy.

pulses at head and tail of the profile when they were of initially low intensity. Figure 7.6 shows three exemplary measured bunch shapes with approximated double-triangular profiles. While some deviations from the ideal bunch shape are apparent (e.g. current dip next to current maximum in the 518 pC case) the measurements show the capability of the applied method. Nearly linear ramps are achieved and the ramp shape and precursor amplitude are tunable. No transverse distortions of the bunch are present, which have been measured with several other bunch shaping techniques. The slight tilt in the x-t projections of the bunches (Fig. 7.6 top) was presumably caused by an off-axis trajectory through the PITZ booster cavity. Trains of such shaped bunches have been produced with MHz repetition rate at PITZ.

A measured longitudinal phase space for triangular bunches with similar parameters as the 518 pC case in Fig. 7.6 is shown in Fig. 7.7. The overall curvature in the phase space, which is also apparent in the simulation results in Fig. 7.10 (a), bottom left, is caused by the sinusoidal accelerating voltage. Slightly different bunch phase in the booster cavity caused the different slope of the longitudinal phase spaces in simulation and experiment. Due to the increase in energy spread caused by the transverse deflecting cavity and the transverse size of the bunches at the measurement screen, the depicted slice energy spread cannot be compared to simulations directly. The modulations that are apparent in the slice energy curvature are caused by non-ideal laser pulse shapes at the photocathode: Due to not fully optimised crystal orientations, the triangular profile of the laser pulse is not smooth but contains peaks. These peaks are smeared out in the bunch current profile by space

charge effects at low energies, but the energy difference which leads to the smooth bunch profile is still apparent in the longitudinal phase space.

Limits of Šolc-filter-based pulse shaping

Every crystal of the Šolc fan filter not only influences the virtual pulse which it adds to the macropulse, but also every pulse that originates from preceeding crystals. Macropulse shapes are therefore very sensitive to changes of single crystals and an analytical treatment of the shaper is impractical. Furthermore, experimental tuning of the pulse shape was found to be much more complicated than in simulation. While in simulation arbitrary pulse shapes can be achieved from arbitrary initial longitudinal distributions within minutes, tuning of the experimental setup could take up to several hours. This discrepancy is not fully understood but so far addressed to improper phase matching (i.e. crystal temperatures) of the shaper and other deviations of the crystal parameters from ideal (crystal cut, transmission, etc.). Continuous tuning of the crystal angles was required as drifts of the bunch shapes were observed on a day's timescale.
As already shown above, space charge forces distort the bunch shapes at low energies. Especially distortions like a changed slope of the bunch current ramp (e.g. Fig. 7.4 (a), 1 nC case) can be pre-compensated by modification of the input laser pulse. Large transverse spot sizes of the laser at the photocathode also reduce space charge forces but ultimately the bunch charge that can be extracted while preserving a certain bunch shape accuracy is limited. Figure 7.4 (a) shows the simulated longitudinal profiles of triangular bunches with different total charges. At 1 nC bunch charge the longitudinal profile is already distorted significantly in the PITZ case. This limit might be different for other electron gun setups (i.e. different gradient at photocathode, laser pulse length, laser spotsize, etc.).
Another limitation of the Šolc fan filter bunch shaping is shown in Fig. 7.8: Due to a constant transverse spot size of the photocathode laser pulse, slices of significantly different charge exhibit different Twiss-parameters. When tightly focused, the different slice β-functions [see also Fig. 7.4 (c)] lead to significantly differing transverse slice sizes at the focal plane. As the plasma wakefield amplitude depends on the bunch electron density [see Eq. (2.30)], very dense slices drive much higher wakefields than others. Such inhomogeneous transverse wakefields can lead to transverse instabilities of the bunch. Furthermore, a particle ensemble that does not fulfill the matching condition

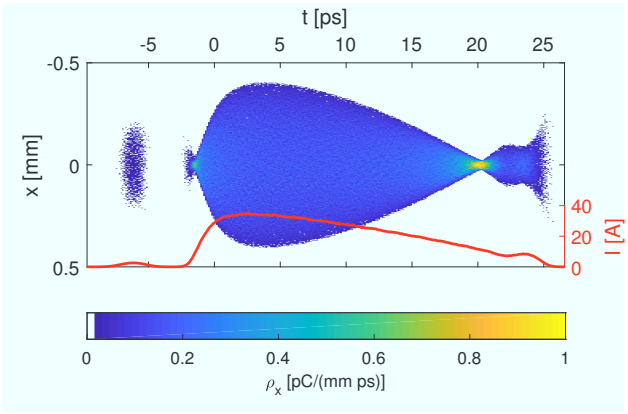

Figure 7.8: Simulated x-t charge density ρ_x of a 600 pC double-triangular bunch at the PITZ plasma cell entrance. The current profile of the bunch is shown in red.

for the transverse RMS bunch sizes in a plasma ion channel [34, 189]

$$\sigma_{x/y} = \sqrt[4]{\frac{1}{\gamma_b}}\sqrt{\frac{\epsilon_{n,x/y}}{k_p}} \ , \tag{7.4}$$

undergoes envelope oscillations. Due to the strongly varying transverse size and a rather constant slice emittance [see Fig. 7.4 (b)] this condition cannot be fulfilled for the Šolc filter shaped bunches in the current setup at PITZ. Therefore, even if transverse instabilities are mitigated by operation in the nonlinear regime, envelope oscillations can lead to beam transport issues. This is discussed in further detail in Ch. 9.
An aspect of laser-based pulse shaping that has not been investigated in the course of this work is that bunches have to be compressed to reach densities suitable for high gradient plasma wakefield accelerators. Even though linear compression is normally pursued, which would allow to preserve the bunch shapes created in the injector, effects like coherent synchrotron radiation (CSR) are known to dilute the final bunch quality. Future studies have to reveal whether this inhibits the utilisation of photocathode-laser-based bunch shaping in high energy PWFA. Nevertheless, the triangular bunch shapes might coincide with bunch shapes that were predicted to mitigate CSR effects in magnetic chicanes [190].

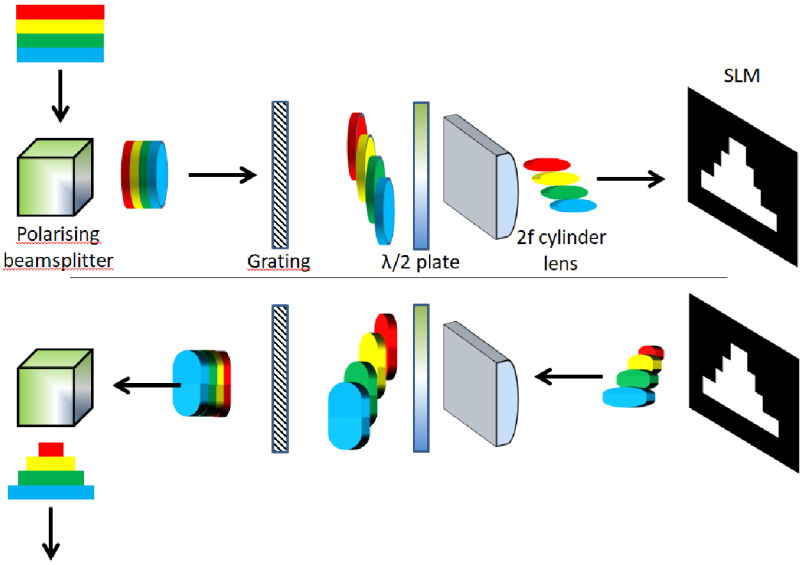

Figure 7.9: Schematic of the SLM-based laser pulse shaping. An incoming chirped laser pulse is dispersed and partially masked on the SLM (upper part). The slices of the outgoing pulse are aligned again and the pulse is reflected to the second shaping stage (lower part).

7.2.2 Prospects of advanced photocathode laser pulse shaping

To overcome the limitations of bunch shaping utilising a Šolc fan filter, laser pulse shaping by spatial light modulators (SLMs) is proposed [168, 191]. A sketch of the SLM-based shaping is given in Fig. 7.9. A laser pulse with a time-wavelength correlation (spectral chirp) is dispersed with an optical grating. The vertical axis now represents the spectrum of the dispersed pulse (i.e. time t for a linear time-wavelength correlation), the horizontal (x-)axis remains the same. Further downstream the laser pulse is focused in the plane which represents time and reflected on an SLM. As the SLM is programmable, arbitrary masks can be applied to the x-t plane of the laser pulse. After shaping, the laser pulse is sent back and reflected by the polarising beamsplitter to a second SLM shaping section which is rotated by 90 ° with respect to the laser pulse orientation, to achieve shaping in the y-t plane. Due to the fact that shaping of the x-t and y-t planes is decoupled, transverse shapes are always rectangular. Furthermore, the temporal (mask) shape is modified the more the final pulse length approaches the bandwidth

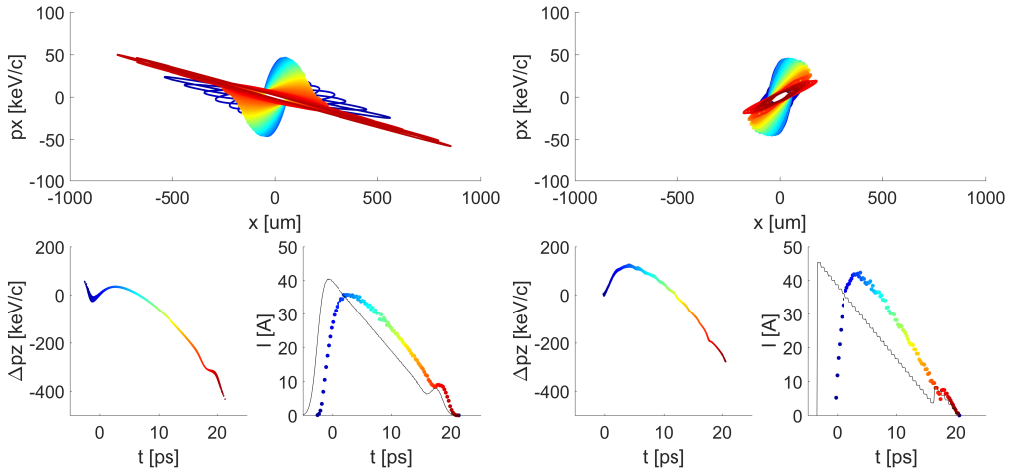

(a) Šolc fan filter ***(b) SLM-based shaping***

Figure 7.10: Simulated transverse slice phase spaces (top), longitudinal phase spaces (bottom left) and bunch current profiles (bottom right) at the plasma entrance position of the PITZ beamline for double-triangular bunches with different photocathode laser pulse shaping methods. The black lines in the bunch current profiles resemble the input particle distributions at the cathode and colours represent longitudinal slice positions.

limit of the shaped spectrum.
Nevertheless, utilising such a scheme, photocathode laser pulses can be shaped longitudinally and transversely in parallel with high flexibility. ASTRA simulations of a bunch shaped to a longitudinal double-triangle with a Šolc fan filter and of a bunch shaped to a similar longitudinal profile with SLMs are shown in Fig. 7.10. While the transverse phase space of the Šolc-shaped bunch shows significant mismatch between different bunch slices, the mismatch is only small in the SLM-shaped case. The transverse shape of the Šolc bunch is homogeneous (i.e. transverse flattop) and transverse size is constant along the bunch. In the SLM case the transverse shape is also flattop but the transverse slice size $\sigma_{tr,slice}$ varies with

$$\sigma_{tr,slice} = \sigma_{max} \cdot \left(\sqrt{\frac{Q_{slice}}{Q_{slice,max}}} \right)^{\kappa} , \tag{7.5}$$

where σ_{max} is the given, maximum transverse slice size, Q_{slice} is the slice charge, $Q_{slice,max}$ is the maximum slice charge in the bunch and κ is a factor

that was varied between 0.5 and 1.5. The distribution shown in Fig. 7.10 (b) corresponds to $\kappa = 1.1$.
Further optimisation of the input photocathode laser pulse might improve the slice matching with the SLM-based shaping method. Nevertheless, the already achieved bunch parameters are much more favourable than the Šolc fan filter results in terms of shape accuracy and slice mismatch. The direct correlation between SLM mask and laser pulse shape also promises better flexibility and shorter tuning time. Among others due to the rectangular transverse laser pulse shapes, which cannot be simulated with the rotationally symmetric treatment of space charge at the photocathode in ASTRA, experimental validation of the simulated bunch parameters has to reveal the actual potential of the SLM-based shaping technique.

Chapter 8

Low density gas discharge plasma cell

The PITZ electron bunches are not dense enough to provide sufficiently high space charge forces for ionisation of a neutral gas medium [192]. Therefore, another prerequisite for demonstrating high transformer ratio acceleration in plasma wakes was a plasma source, which can supply reproducible plasma acceleration media at 10 Hz repetition rate with tunable electron densities of up to several $10^{15}\,\mathrm{cm}^{-3}$. In the course of the presented studies a discharge plasma cell was conceived, developed, built and characterised for PWFA experiments. This work is described in the following sections. Additional measurement data on the discharge plasma cell are given in Appendices A, B and C. The description is largely based on the results published in Ref. [193] and Ref. [194]. Vacuum test results of the polymer foil windows utilised in this work are published in Ref. [195].

8.1 Gas discharge plasma physics

Electric discharges in gases are one of the most common principles of plasma formation, occurring e.g. in lightning, lighting or high voltage switchgear, to only name a few. Such plasmas form due to collisional ionisation of neutral gas particles by thermal movement of plasma particles or by charged particles which were accelerated in an externally applied electric field. While the principle may be similar, various types of gas discharges with significantly different dynamics and physical effects exist. These different types of gas discharges are commonly distinguished by their characteristic discharge voltage

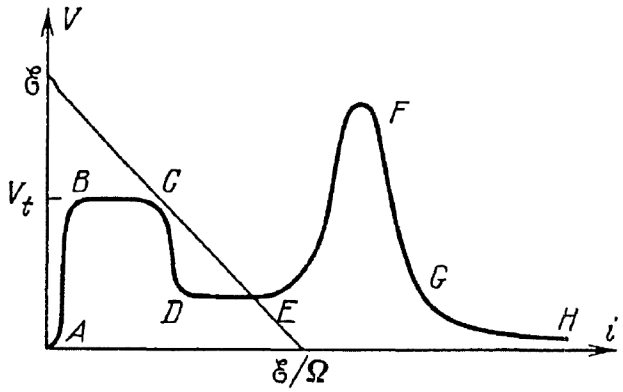

Figure 8.1: Schematic of discharge voltage V to discharge current i characteristic for different types of discharges: non-self-sustaining discharges A-B, Townsend dark discharges B-C, normal glow discharges D-E, abnormal glow discharges E-F, glow discharge to arc transition F-G and arc discharges G-H [196].

and discharge current. Typical voltage-to-current characteristics are shown in Fig. 8.1.

To initiate a gas discharge between two electrodes, a voltage that exceeds the ignition potential of the gas has to be applied. In homogeneous electric fields this potential U_{br} is described by [196, 197]

$$U_{br} = \frac{B \cdot p \cdot d}{ln\left(\frac{A}{ln(1/\gamma+1)}\right) + ln(p \cdot d)} \ , \tag{8.1}$$

where A and B are gas species dependent constants, p the gas pressure, d the electrodes' distance and γ the third Townsend-coefficient, which describes secondary electron emission from the electrodes. The relation between U_{br} and $p \cdot d$ is called *Paschen curve*. Examples of Paschen curves for various discharge media are shown in Fig. 8.2. The curves all exhibit a characteristic minimum, the Paschen minimum, which represents the transition between high pressure and low pressure discharges. At this point the mean free path of ionised particles approximately corresponds to the distance in which ionised particles gain enough energy to ionise neutral atoms on collision. If either the pressure or the electrodes' distance is reduced (left hand branch), the mean free path becomes longer with respect to the electrode distance. Hence the probability of a collision per particle is reduced and the particle energy (and thus the electrode voltage) has to be increased to ensure ionisation in any interaction. If the pressure or electrodes' distance is increased (right hand branch), the mean free path gets smaller than the optimum distance of

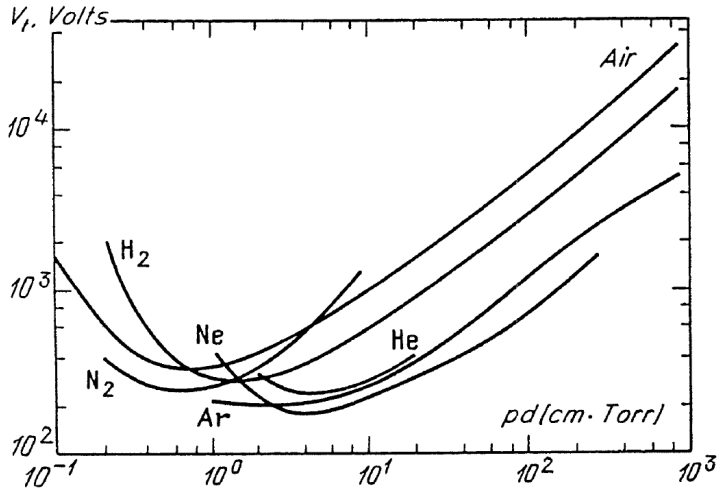

Figure 8.2: Paschen curves for different discharge gases [196].

energy acquisition and therefore ionised particles tend to lose energy before being energetic enough to further ionise neutral atoms. Again the breakdown voltage has to be increased to compensate for this.
To generate the required plasma electron densities of up to several $10^{15}\,\mathrm{cm}^{-3}$ the discharge gas has to be heated to temperatures of a few eV, as will be shown lateron. A PWFA plasma cell therefore has to be operated in the arc regime, to enable the high current densities to provide sufficient heating of the discharge gas. The high temperatures enable collisional ionisation by thermal energy, not only due to energy gained in the external electric field. Current-carrying electrons are nevertheless mostly supplied by emission from the cathode, which results from thermionic, field and combined emission processes [196]. To establish an arc discharge, these processes have to be initiated. As heating of the cathode requires complex setups, local heating of the cathode surface by the discharge current itself is pursued. In a DC discharge, this local heating quickly leads to macroscopic erosion of the electrodes. Furthermore, the power consumption of a DC arc discharge would be high as usually currents of several hundred Amperes are required at discharge voltages of several 10 V. Pulsed discharges are therefore employed. A simplified analytical description of the arc plasma was used to estimate the necessary amplitude and pulse length of the discharge current. The analytical model is based on self-consistent, iterative numerical calculation of

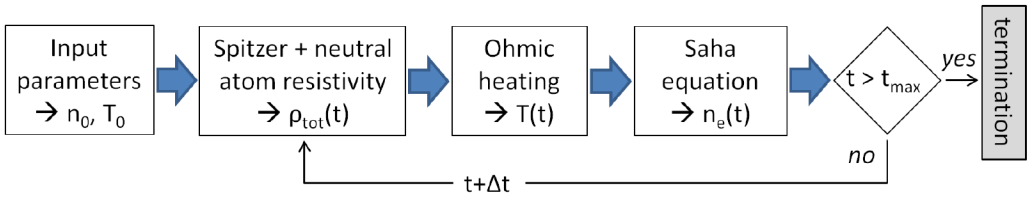

Figure 8.3: Schematic of the numerical discharge modeling.

the Spitzer formula of plasma resistivity [196]

$$\eta_{Spitzer} = \frac{\pi Z e^2 m_e^{1/2} \ln \Lambda}{(4\pi\epsilon_0)^2 (k_B T)^{3/2}} \ , \tag{8.2}$$

where Z is the ionisation degree of the plasma, m_e the electron mass, $\ln \Lambda$ the Coulomb logarithm [196, 198], k_B the Boltzmann constant and T the plasma temperature, and the Saha ionisation equation [47]

$$\frac{n_{i+1} n_e}{n_i} = 2 \sqrt{\frac{2\pi m_e k_B T}{h^2}}^3 \frac{g_{i+1}}{g_i} exp\left(-\frac{\mathfrak{E}_{i+1} - \mathfrak{E}_i}{k_B T}\right) \ . \tag{8.3}$$

Here, n_e is the plasma electron density, n_i is the density of ions in the i-th ionisation degree, g_i is the statistical weight, also called *degeneracy* or *multiplicity*, of the i-th state ($g = 2l + 1$ with l the total spin angular momentum) and $\mathfrak{E}_{i+1} - \mathfrak{E}_i$ is the ionisation energy of the $i + 1$-st state. Temperature development of the gas was modeled by ohmic heating of the gas for the given resistivity and discharge current [199]. The Spitzer formula takes only electron-ion collisions into account and hence predicts negligible resistivity for very low ionisation degrees. To avoid this unphysical result, the resistivity due to electron-atom collisions

$$\eta_{ea} = \frac{m_i}{n_e e^2} \frac{n_n \pi r_a^2 p}{n_{n0} m_e^{1/2}} (k_B T)^{-1/2} \ , \tag{8.4}$$

where m_i represents the ion mass, n_n the density of neutral atoms, r_a the Bohr radius, p the gas pressure and n_{n0} the initial neutral density [199], is added to the Spitzer resistivity to calculate the total resistance of the plasma

$$\rho_{tot} = (\eta_{Spitzer} + \eta_{ea}) \cdot \frac{l_p}{A_p} \equiv \rho_{Spitzer} + \rho_{ea} \ , \tag{8.5}$$

where l_p is the length and A_p the cross sectional area of the plasma. The numerical loop is illustrated in Fig. 8.3. It is calculated until the time t reaches

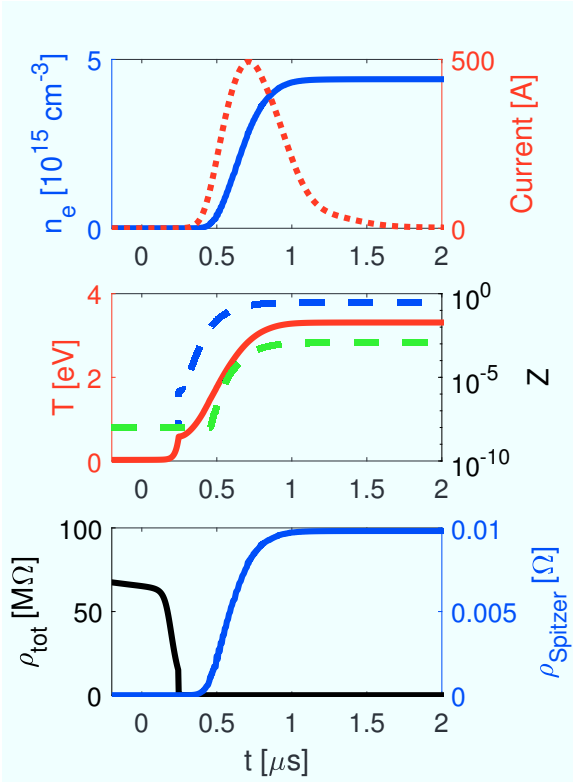

Figure 8.4: Calculated plasma parameters for a pulsed discharge current (top, red). Shown are plasma electron density (top, blue), temperature (centre plot, red), first (centre plot, dashed blue) and secondary (centre plot, dashed green) ionisation degrees and the total and Spitzer resistivities (bottom) of the discharge.

the maximum time of the input current pulse t_{max}, which is generated in SPICE [200] using a simplified model of the discharge circuit (Fig. 8.11). Results of this calculation are plotted in Fig. 8.4. A pulse of less than one microsecond FWHM length with an amplitude of a few hundred Amperes is calculated to be sufficient to create a plasma of the targeted maximum density when temperatures exceed $(2-3)$ eV. The accuracy of the analytical model is limited as e.g. the Saha equation only applies to plasmas in *thermodynamic equilibrium* (TE) or *local thermodynamic equilibrium* (LTE), i.e. when plasma electron temperature and plasma ion temperature at a certain position in the plasma coincide. This is not necessarily fulfilled, especially during discharge formation. Radiative cooling and thermal losses at the surfaces of the electrodes and the discharge vessel are also neglected. Nevertheless, the approximated discharge parameters allow to design a plasma

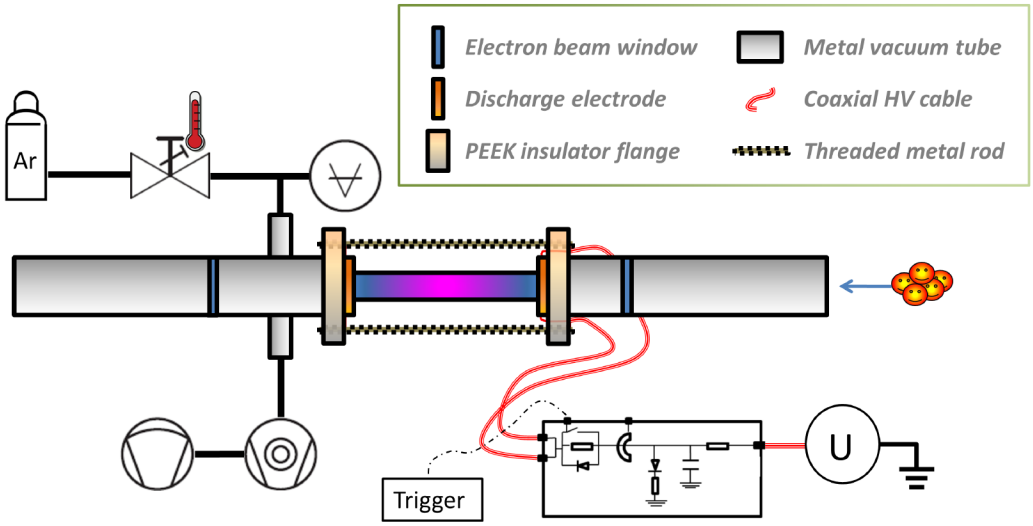

Figure 8.5: Schematic layout of the PITZ gas discharge plasma cell. The PITZ electron beam (orange dots) enters from the right through a polymer window to interact with the plasma (blue/purple, cell centre).

cell, the exact electron densities of which can be determined experimentally.

8.2 Plasma cell design

Cell layout

A simple setup of two opposing electrodes with central holes for the electron beam was chosen for the PITZ gas discharge plasma cell (GDP), partially based on previous designs, developed for heavy ion beam experiments [201]. One electrode is connected to the high voltage output of a driver circuit, the other to the ground of the same circuit. To reduce the parasitic inductance of the cell, a coaxial design was chosen. The discharge current is fed to the high voltage electrode by a coaxial transmission cable, then flows through the plasma to the other electrode and finally back to the outer conductor of the transmission cables via metal rods. The four threaded metal rods, which are placed on a circle around the plasma, also provide mechanical stability of the cell. An illustration of the setup is shown in Fig. 8.5.

The discharge gas atmosphere is established in a cylindrical tube of quartz-glass between the two electrodes. Argon was chosen as a discharge gas,

primarily for its low ionisation threshold (see Fig. 8.2). Furthermore, Argon is available at low cost and easy to handle due to its inert nature as a noble gas. It is also detectable with residual gas analysers with high sensitivity (to detect gas leakage to the accelerator beamline) and readily available in gas mixtures with hydrogen, which enables several diagnostics methods (see Sec. 8.4).
To allow fast ignition of the plasma arc discharge, a DC glow discharge is maintained in the discharge gas. This ensures that a sufficient number of ionised particles is present and further collisional ionisation by fast, ionised argon can be triggered without delay. A pulsed high voltage is then applied between the electrodes. The high current driven by this voltage locally heats the cathode and thus initiates the transition to an arc discharge. The discharge electronics circuit is discussed in detail below.

The length of the discharge vessel of 100 mm was chosen such that bunch energy changes are well detectable with the PITZ bunch diagnostics for the expected wakefield amplitudes in the plasma. Due to the spatial constraints in the PITZ beamline, the overall length of the setup was limited to less than 480 mm. This maximum overall length led to the decision to use electron windows for separation of the cell's gas atmosphere from the accelerator beamline vacuum instead of a differential pumping system. The inner diameter of the discharge vessel is 11 mm, which allowed a maximum electrode aperture of 10 mm. This minimises beam particle losses at the end of the cell (where the transverse bunch size is big due to the typical beam focus point at the plasma entrance) while maintaining a direct line of sight (i.e. discharge path) between the electrodes. Vacuum sealing between glass and electrodes is realised with indium gaskets. The indium is pressed onto the discharge tube by compressing it between glass and adjacent metal flange surfaces. With this arrangement leakage rates compatible with ultra-high vacuum (UHV) requirements have been achieved (He leakage current $< 10^{-10}\ \frac{\text{mbar}\cdot\text{l}}{\text{s}}$).

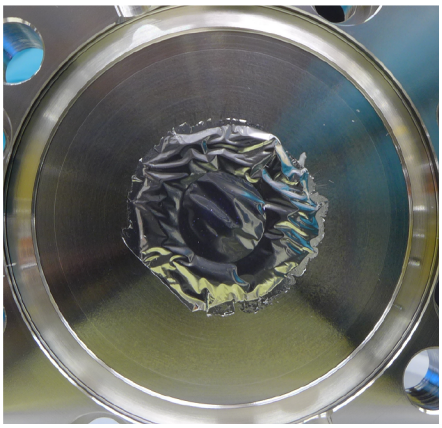

Figure 8.6: Polymer foil window glued over the 10 mm central aperture of a modified DN40 Conflat vacuum flange.

Initially, a sealed-off operation of the cell (single gas fill prior to experiments) was pursued to minimise the amount of equipment that would have to remain in the accelerator tunnel during operation. Due to the reasons described in the next section, this was replaced by continuous gas exchange as shown in Fig. 8.5 (temperature controlled valve and pressure gauge on top and vacuum pumps on bottom of left hand side of cell).

Electron windows

Thin polymer foils, already applied in other setups at PITZ [202], were used as electron windows for separation of the beamline vacuum from the discharge gas atmosphere. They provide low gas permeation (permeation constant $< 10^{-13}\,\mathrm{m}^2/\mathrm{s}$) with average scattering angles for 23 MeV electrons of $0.1\,\mathrm{mrad} - 0.2\,\mathrm{mrad}$ at $0.9\,\mu\mathrm{m} - 1.9\,\mu\mathrm{m}$ thicknesses [202]. For beamline installation, the foils are glued onto a DN40 Conflat vacuum flange with a central aperture of $5\,\mathrm{mm} - 10\,\mathrm{mm}$ diameter, using a vacuum compatible epoxy resin. An exemplary window is shown in Fig. 8.6. As the existing foil material showed significant quality variations between different samples, Al-coated polyethylene terephthalate (PET) capacitor foil material by Birkelbach Kondensatortechnik GmbH was introduced in the course of this work. To prove the applicability of these windows, gas permeation through the capacitor foils was investigated for thicknesses of $0.9\,\mu\mathrm{m}$, $1.9\,\mu\mathrm{m}$ and $4\,\mu\mathrm{m}$. Tests were

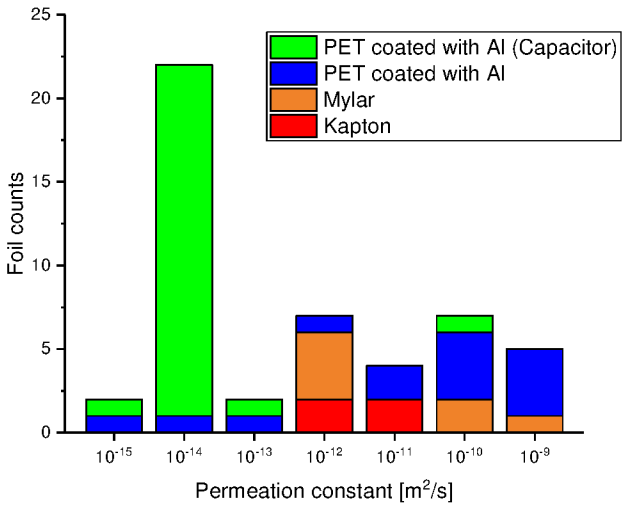

Figure 8.7: Measured gas permeation constants for different foil materials and specimens.

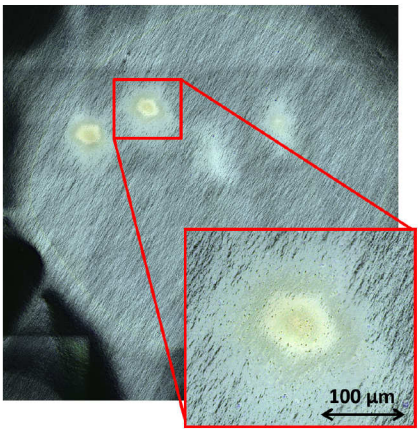

Figure 8.8: Overlay of optical and laser microscope pictures of a single-sided metalised polymer foil window of 1.9 μm *thickness, which was exposed to* $2\,mC \pm 0.5\,mC$ *of* $\sim 23\,MeV$ *electrons. The foil is viewed from the non-metalised side. The zoom shows an alleged position of beam passage.*

conducted by separating an evacuated test volume from a gas volume filled with 130 mbar of helium gas by the foil specimen. A leak tester was used to monitor the helium gas current on the evacuated side. Gas permeation constants K_p were calculated from these measurements by

$$K_p = \frac{\dot{Q} \cdot d}{\Delta p \cdot A} \,, \tag{8.6}$$

where $\dot{Q}$ is the measured gas current, d is the foil thickness, A the permeation area and Δp the pressure difference between the two test volumes. The results are plotted in Fig. 8.7. Due to the much better reproducibility of the permeation, beam measurements presented in this work were conducted with 1.9 μm-thick single-sided metalised PET foil windows mounted to the gas discharge cell, which corresponds to a mean scattering angle of the beam electrons of (0.19 ± 0.05) mrad at 23 MeV [195].
After exposure to the PITZ electron beam with an integrated charge of $\sim (2 \pm 0.5)$ mC, an increased gas permeation to the accelerator beamline was detected and alterations to the foils were found after dismounting. These alterations are documented in Fig. 8.8. Several spots are visible by a tempering-like colour change as well as by their elevation of several μm, which is revealed by the laser microscope height scan. These changes are addressed to local heating of the foil due to energy deposition by scattered beam electrons.
Thermal conduction through the foil material was calculated to be negligibly

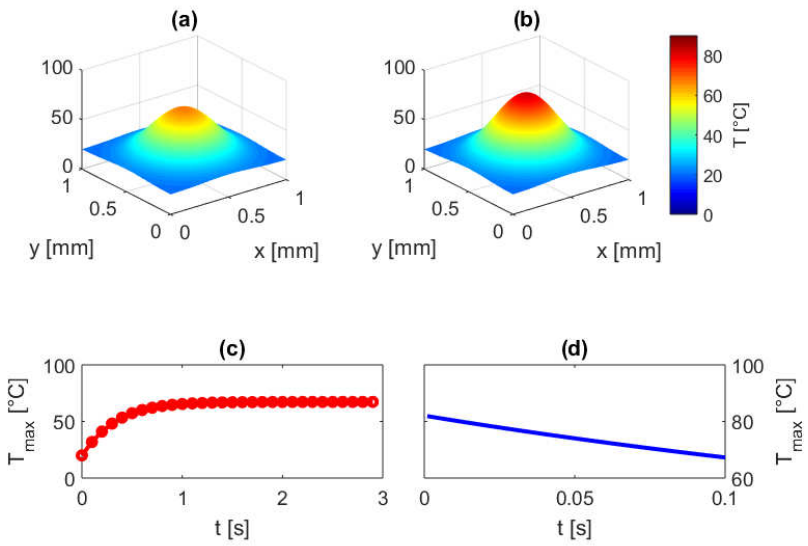

Figure 8.9: Calculated temperature rise in the polymer foil during continuous bunch passage. (a) shows the temperature distribution directly before passage of the 30th bunch within a 10 Hz train, (b) the temperature distribution directly after passage of the 30th bunch in a 10 Hz train. The development of the maximum foil temperature during a 10 Hz train of bunches (red dots) is shown in (c). The maximum foil temperature between two bunches is plotted in (d).

small. Also convective heat transfer does not contribute significantly to the foil temperature, as the discharge gas on the pressurised side of the foil has a small density. The radiative heat transfer was estimated by numerically calculating the temperature rise at a position where a 23 MeV, 0.2 mm RMS size transverse Gaussian bunch with a charge of 1 nC passes the foil. Heat deposition due to the scattering of bunch electrons was calculated to be $\sim 10^{-5}$ W at 10 Hz bunch repetition rate. The results of this calculation are shown in Fig. 8.9. A quasi-equilibrium between radiated heat and foil temperature is reached after passage of ca. 15 bunches ($t = 1.4$ s), as shown in Fig. 8.9 (c). The temperature distributions [Fig. 8.9 (a,b)] correspond to the transverse Gaussian profile of the electron bunches. Neither is the melting temperature ($\sim 250\,^{\circ}$C) reached, nor is the temperature drop between two bunches such high that it may cause mechanical stress in the foil [Fig. 8.9 (d)]. Nevertheless, the maximum temperatures after the passage of a bunch exceed the glass transition temperature of PET ($\sim 70\,^{\circ}$C) [203]. This might cause a change

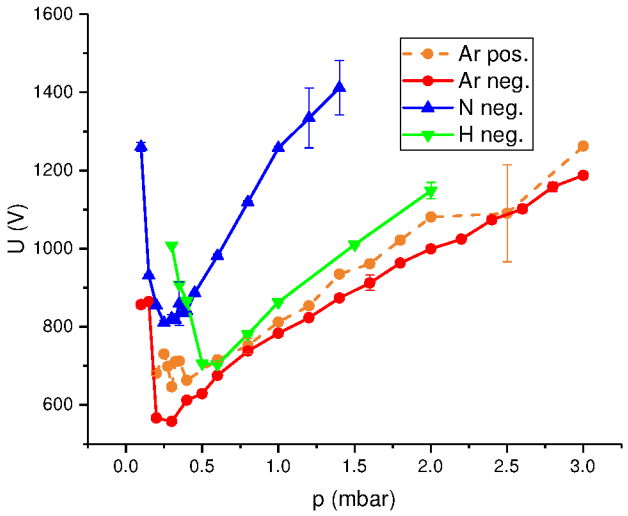

Figure 8.10: Measured breakdown voltages for different gas species. Positive and negative polarity high voltage measurements are shown for argon.

of mechanical stability at the point of bunch passage, which is supported by the fact that the foil has gained elevation towards the evacuated beamline volume. An expansion towards one direction forced by the pressure difference over the foil might spread the PET in glass phase thin, which increases gas permeation and can lead to microscopic and ultimately macroscopic window breaking.

Discharge electronics

A negative polarity was initially chosen for the discharge voltage to exploit hollow cathode effects during the transition from glow to arc discharge [204]. Even though the hollow electrodes were finally replaced by a less complex, plane electrode design, the negative voltage was kept, as it provides minimum breakdown voltages in argon, as shown in Fig. 8.10.

To supply the low DC current for maintaining a glow discharge and the pulsed, high voltage and high current for the arc discharge, a pulse electronics circuit as sketched in Figs. 8.11 and 8.5, bottom right, was set up, which is connected to the discharge cell via coaxial transmission cables. The inner conductor of the coaxial transmission cables is connected to one electrode, the outer conductor to the other discharge electrode via the outer metal rods. Capacitor C in Fig. 8.11, which has a capacitance of several μF, is charged via a charging resistor R1 to a voltage well above the breakdown voltage

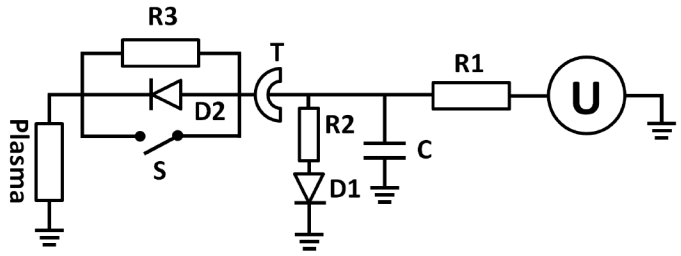

Figure 8.11: Electrical layout of the discharge electronics. Negative polarity of the charging voltage U was used in the final setup.

of the discharge medium (usually -2.4 kV, see also next section). As soon as the breakdown voltage is exceeded, a glow discharge plasma forms. The current of several mA is delivered through the high ohmic resistor R3 past the pulse switch S. When the switch is closed, the capacitor is discharged within a few μs into the plasma load. Due to the capacitance C and the parasitic inductances of the transmission cables and the plasma cell, the discharge current would oscillate sinusoidally. To avoid an oscillating current of decreasing amplitude, the reverse current is dumped in the damping resistor R2 through D1 after the first, negative half wave of the discharge current. D2 is protecting the high power thyristor switch from reverse voltages. The discharge current is measured with the Rogowski coil current transformer T.
To insulate the cell's electrodes from the beamline components, they are embedded in insulator flanges made of polyether ether ketone (PEEK), as depicted in Fig. 8.5. Initially discharges to the grounded foil window flanges were prevented by minimising the distance between window flange and discharge electrode to 2 mm, which places this discharge path on the left branch of the Paschen curve. While this method demonstrated reliable insulation in a limited pressure range, the window flanges were finally set on floating potential, to allow for higher flexibility in the discharge parameters.

8.3 Discharge jitter mitigation

During the first PWFA experiments with the discharge plasma cell, severe jitter in the discharge current timing, amplitude and waveform were encountered. Figure 8.12 shows five exemplary discharge current traces which exhibit all types of observed jitters. While the first pulse nearly corresponds to an unperturbed, damped sine wave, the other pulses show a step in the current rise. Furthermore several pulses start with varying delays compared

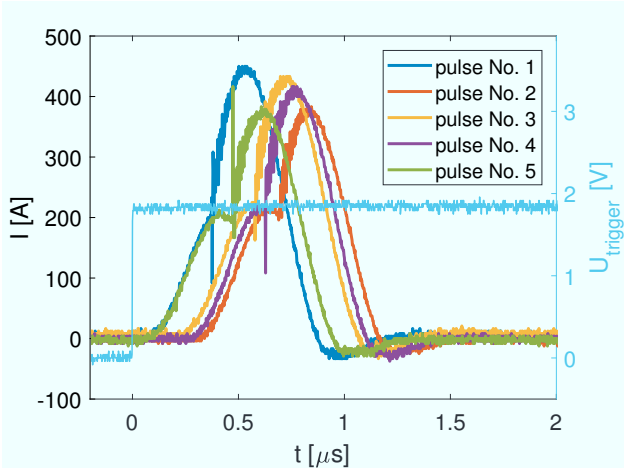

Figure 8.12: Discharge current waveforms for five consequent discharges. The trigger voltage signal for all five pulses is similar [193].

to pulse No. 1 and also have different maximum current amplitudes. Similar effects have also been observed on other plasma cells that operate in a similar parameter range [205]. Such variations in the timing and development of the discharge affect the plasma density at any point of time with reference to the discharge trigger. This inhibits reproducible PWFA experiments.
To find the source of the discharge jitter several changes of the cell design and the discharge parameters were done while monitoring the discharge current waveform and spectrum. Ceramics were used instead of the PEEK insulators, the indium gaskets were changed to Viton, the discharge gas was changed to nitrogen and hydrogen, the electrode layout was changed from hollow electrodes to plane electrodes with central apertures, consequent cell runs with and without gas exchange were monitored, and various other tests. The final setup that resulted from these investigations is described in the previous section. A typical development of the discharge spectrum in a sealed-off cell (initially filled with ~ 1 mbar of pure argon) during continuous run at 10 Hz is shown in Fig. 8.13. While initially the hydrogen line is barely visible, its intensity rises quickly and dominates the spectrum after the two and a half hours run time. Discharge jitters were observed from ca. one hour on.
A new gas fill with pure argon was measured to mitigate discharge jitters for a short time, whereas this was not reproducible in all cases. The origin of the discharge jitter was finally attributed to two phenomena:

1. degradation of stainless steel electrodes in the discharge (layers of pre-

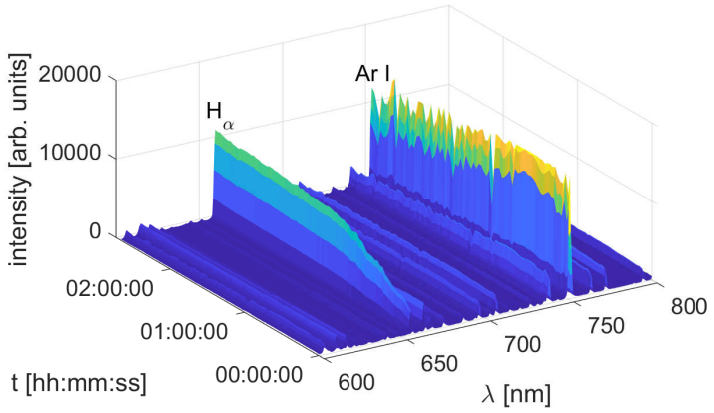

Figure 8.13: Time development of a cutout of the discharge spectrum during continuous 10 Hz pulse operation. Shown are the most prevalent spectral lines of hydrogen (H_α, 656.3 nm) and argon (750.3 nm) [193].

sumably hydro-carbons formed on the surface of the electrodes),

2. a change of the discharge gas composition due to release of hydrogen from the cell walls by high temperature ion impact.

As shown in Fig. 8.5, a small, continuous gas flow through the cell was therefore established. The 1.4429 electroslag remelted (ESR) stainless steel electrodes were exchanged with copper ones. Copper has several positive effects on the discharge formation. Corrosion, as seen on the steel surfaces, does not occur. The higher conductivity and the resulting smaller skin depth enhance local heating and thus thermal emission of conduction electrons. Furthermore its melting point is significantly lower. This can lead to enhanced local release of metal ions at the cathode which produce large amounts of secondary electrons when they impinge on the cathode again.

These changes completely mitigated the current waveform jitters and largely reduced the ignition timing jitters. To further reduce the timing jitter, gas pressure, pulse capacitance, length and number of parallel pulse transmission cables, maximum capacitor voltage and several other parameters like e.g. glow discharge current amplitude and repetition rate were varied. While the two latter parameters did not have measurable influence on the discharge performance, the former were found to have significant impact on the ignition timing jitter. The argon pressure was varied for every change of the electronics parameters and the minimum measured RMS jitter of 100 consequent discharges at 5 Hz was taken into account for comparison between

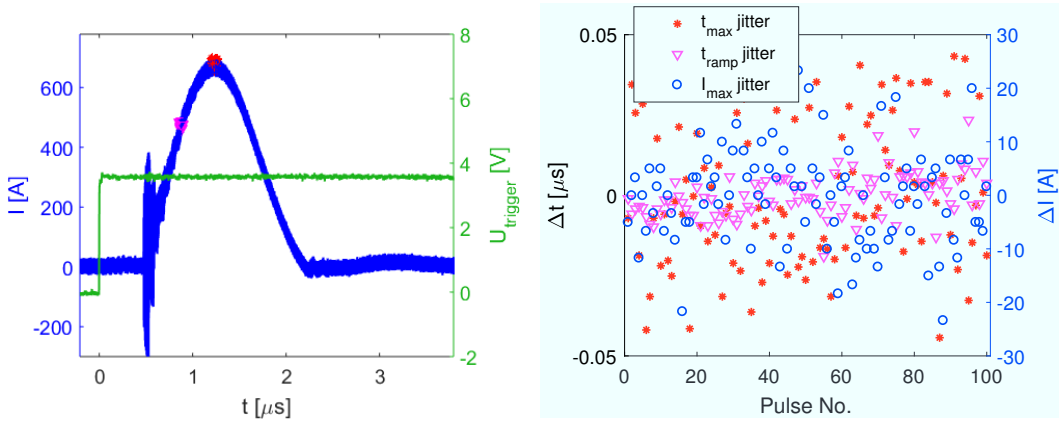

(a) (b)

Figure 8.14: Current traces of 100 consequent discharges at 2.6 kV initial capacitor voltage and 0.6 mbar argon pressure (a). The variation of the maximum current timing (t_{max}), the timing of 60 % maximum current (t_{ramp}) and of the maximum current amplitude (I_{max}) from their mean values are shown in (b).

different setups.
Figure 8.14 shows such a measurement. As the time of maximum current is prone to signal noise, the time when the current reaches 60 % of its maximum was used as a figure of merit (Fig. 8.14, magenta triangles). This current level is usually well above the noise at the front of the pulse, which is caused by the high current rise rates during plasma ignition. Putting the measurement time to the current ramp also helps to automatically identify pulses which exhibit a similar maximum current timing but have a current rise of changed shape.

The results of measurement sequences for different inductance L and capacitance C configurations of the discharge electronics are plotted in Fig. 8.15. A roughly linear dependence of the timing jitter on the LC product of the discharge electronics is observed. As the absolute LC is not determined, numbers are given relative to the original configuration L_0C_0. Parasitic inductances of the plasma cell and within the electronics circuit are neglected. The reduction of ignition time jitter is attributed to a longer period of high voltage applied between the electrodes: The voltage between the electrodes immediately after closing the pulse switch corresponds to the capacitor charging voltage, due to the high resistance of the initial glow discharge plasma (see Fig. 8.4, bottom plot). The voltage then decreases as the plasma cur-

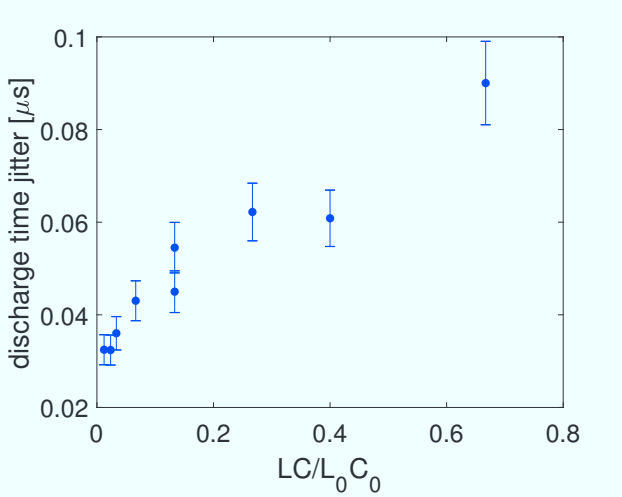

Figure 8.15: Discharge timing jitter for varying discharge pulse electronics inductance and capacitance products.

rent rises after the fast initial voltage increase and with decreasing plasma resistance. This voltage decrease can be delayed by several 10s to 100s of nanoseconds with lower values of LC, as revealed by SPICE [200] simulations incorporating the dynamic discharge resistance. The "Equal-area Criterion", known from high voltage engineering, predicts a constant time integral for the voltage at the electrodes from the time of application of the voltage until breakdown, i.e. full build-up of an arc discharge [206]. Accordingly, a delayed voltage decrease between the electrodes corresponds to shorter breakdown delays and thus also to smaller breakdown time jitters. Further jitter reduction via minimisation of the LC value is limited by parasitic impedances and the minimum energy needed to form an arc discharge, i.e. minimum current densities in the plasma and on the cathode.

Consistently, a similar result can be achieved by increasing the maximum capacitor voltage as shown in Fig. 8.16. In contrast to LC-reduction, the voltage can be increased without theoretical limit and it is expected that the discharge jitter would drop further. This assumption is also based on the Equal-area Criterion. An initially higher voltage reduces the time delay until the integral voltage has reached the constant breakdown value and thus the jitter is reduced. Even though this is a valid and far more common method of reducing discharge ignition jitters, it can quickly result in major effort in terms of insulation, power supply and electronics equipment, while the previously applied means rather result in simplification and reduction of

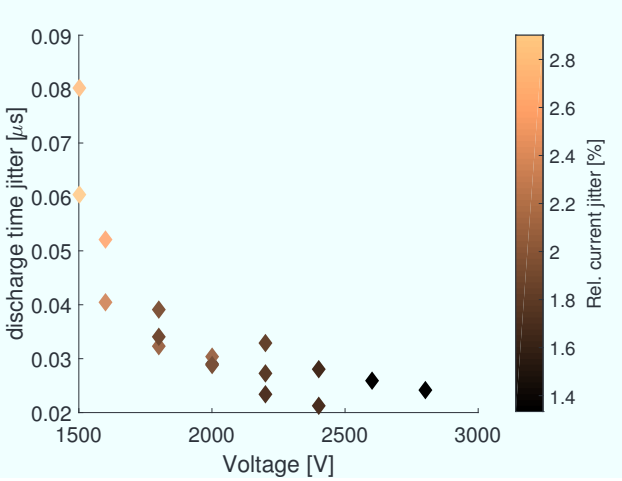

Figure 8.16: Discharge timing and current amplitude jitter for varying discharge pulse capacitor voltage [193].

components.
The minimum achieved RMS timing jitter is 21 ns at a pulse duration of ~ 1 µs FWHM, as shown in Fig. 8.16. Multiplication of this jitter value with the time derivative of the spectroscopically measured density evolution implies a corresponding relative plasma electron density jitter of $\sim 0.5\,\%$ directly after the discharge current termination (compare Fig. 8.22), which translates into an RMS plasma wavelength jitter lower than $0.25\,\%$.
A voltage of -2.4 kV was chosen for the operation of the cell during PWFA experiments as this reduces the stress on the discharge electronics and still provides sufficient reproducibility.
To validate the electronic jitter measurements, direct determination of the plasma density measurements based on the wakefield interaction of the PITZ electron beam with the discharge plasma were performed. As described in Sec. 4.1.3, bunches with lengths on the order of or longer than the plasma wavelength can be subject to the self-modulation instability when they interact with a plasma. The periodicity of such a self-modulated electron bunch directly depends on the plasma density [112] and thus can be taken as a measure for the discharge stability. Even though the suitability of this parameter for absolute density measurements is discussed in the next section, a change in plasma density unambiguously affects the periodicity of the bunchlets of a self-modulated bunch. The bunch arrival timing jitter, which is on a ps-scale, can be neglected as the plasma density evolves on a time scale at least three

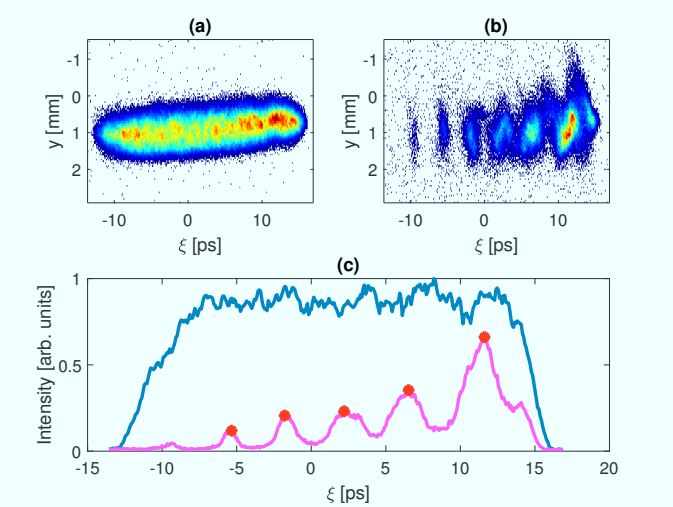

Figure 8.17: Time resolved bunch transverse-longitudinal projections in the co-moving coordinate ξ=z/c-t without (a) and with (b) interaction with the cell plasma. (c) shows the corresponding bunch current profiles (blue without and purple with plasma interaction) and the microbunches that are taken into account (red asterisks) [193].

orders of magnitude longer.
Figure 8.17 shows the transverse-longitudinal projection of a 22.5 MeV, 1 nC flat-top electron beam without and with plasma interaction at a delay between end of the discharge current pulse and bunch arrival of 60 µs. The longitudinal profile is measured using the transverse deflecting structure (TDS, see Ch. 6) and a scintillator screen. To achieve the highest possible measurement resolution, the delay between first and last resolvable microbunch in the self-modulated bunch is measured. The RMS deviation in 10 consecutive measurements was found to be 0.05 ps in the shown case, whereas the resolution given by the pixelsize of the measurement screen's camera was 0.08 ps. Taking the average microbunch distance as a rough measure of the plasma wavelength, the measured RMS deviation and the camera resolution translate into approximate density jitters of 0.6 % and 1 %, respectively. Measurements at different plasma densities, i.e. different plasma ignition-bunch arrival delays, yielded similar results. Even though the resolution of the SMI-based measurements is only sufficient to confirm the order of magnitude of the electronic jitter measurements, the stability of the beam-plasma interaction also excludes influence of e.g. plasma instabilities which might not be visible in the discharge current waveform [193].

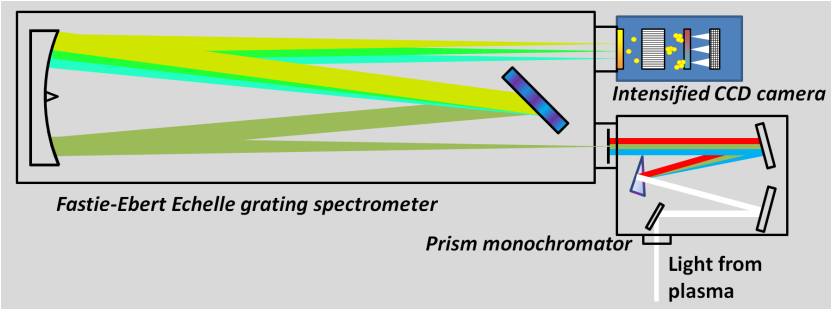

Figure 8.18: Setup of the spectrometer used for line width measurements. The prism monochromator reduces the spectral bandwidth of the incoming light. This avoids overlap of dispersion orders in the main spectrometer. Light is then dispersed further in the Fastie-Ebert configuration spectrometer.

8.4 Plasma electron density measurements

8.4.1 Spectroscopic density measurements

Plasma density measurements based on the analysis of the emission spectrum of the plasma provide a non-invasive, time- and spatially resolvable measurement of the electron density. A common method is the evaluation of the broadening of spectral lines due to the influence of the electric fields of plasma electrons on the atomic states. In homogeneous electrical fields this effect leads to a shift of spectral lines. Due to the random distribution of free charges in a plasma, their space charge fields also randomly shift the spectral lines of plasma ions and atoms, which leads to line broadening [207–210]. As these methods are widely used, a profound basis of theoretical and experimental data exists to ensure the accuracy of the measurements.

Other mechanisms also have influence on the spectral line width, the most prominent being *Doppler*-, *resonance*- and *van der Waals*-broadening. While the first is caused by the thermal motion of the emitter, the latter two result from interaction of the emitter with neutral atoms of the same species. As described in the previous section, the PITZ gas discharge cell is operated with argon gas. While line broadening is difficult to evaluate for argon emission lines due to small line width changes, hydrogen exhibits very strong broadening effects due to electric fields of plasma electrons. Therefore, 2 % of hydrogen is added to the argon during density measurements. Discharge dynamics are assumed to be not affected by this rather low amount of hydrogen gas. The low percentage of hydrogen also has the advantage that hydrogen

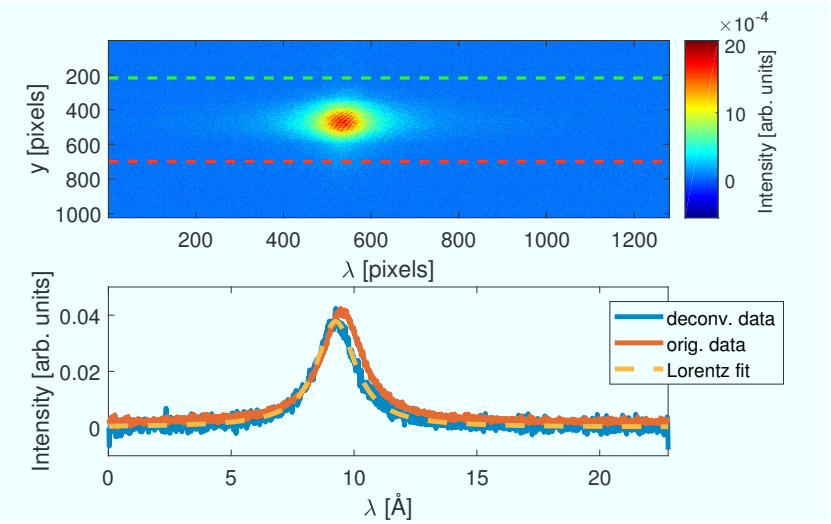

Figure 8.19: Dispersed H_α-line on the CCD camera chip (top) and corresponding projection between green and red dashed lines with wavelength scaling (bottom, red line). Doppler and instrumental broadening are deconvoluted from the line profile (bottom, blue line) and a Lorentz curve is fit to the data (bottom, orange dashed line).

densities are low and thus neutral atom interaction can be neglected.

Due to its high signal strength, which allowed a time resolution of 0.5 μs, the Balmer-α line at 656.1 nm is chosen for the density diagnostics. Measurements were done using a Sopra UHRS F1500DP Fastie-Ebert configuration spectrometer with an Echelle grating operated in the 8th diffraction order [211], and an intensified charge-coupled device (CCD) camera with an overall spectral resolution of $\sim$1 pm at 656 nm. A schematic of the setup is shown in Fig. 8.18. The spectrometer was calibrated using two calibration sources based on argon/mercury and neon/platinum emission spectra. After emission from the plasma, light was transported to the entrance of the spectrometer via a 1 mm diameter optical fiber. Figure 8.19 shows a measurement of the H_α-line. The Gaussian line broadening due to the spectrometer is measured with calibration lines of negligible natural linewidth. Doppler broadening, which also results in Gaussian line shapes, is estimated with the numerical temperature calculations shown in the previous section for the final discharge parameters. Gaussian RMS widths of the two broadening functions are added quadratically and the resulting function is deconvoluted from the measured line profile. The resulting data is fit with a Lorentzian

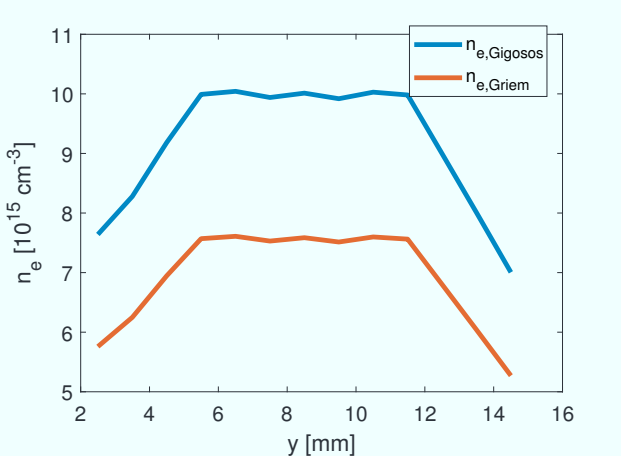

Figure 8.20: Plasma densities for different vertical positions of the spectrometer fiber. Measurements were taken with a 3 µs delay to the discharge current pulse.

function, which is an approximation of the broadened line profile [207] and which agrees well with the measured line shapes. Plasma densities are calculated using the semi-analytical formula given by *Griem* in Ref. [207] and the formula based on line profile simulations by *Gigosos et al.* from Ref. [210]. As both references are commonly used, densities calculated from both models are given in this work.

To assess the full density profile in the plasma column, electron densities were first measured vertically to the electron beam axis. Results of the scan, which was performed in the longitudinal centre of the cell, are shown in Fig. 8.20 . From these measurements, the vertical centre was determined at a fiber position of $y = 8.5\,\text{mm}$. This is also assumed to be the position of electron beam passage. The measured vertical density profile is nevertheless not identical with the actual density distribution in vertical direction. First, the density is integrated along the line of sight (convoluted with the local brightness of the plasma) and second, the rather large numerical aperture of the used fiber together with the curvature of the glass leads to an observed vertical range of up to 12 mm (see also Appendix B for details on the position uncertainty). Due to the symmetric distribution it is nevertheless possible to determine the vertical centre position from the measured density profile. The results of a longitudinal density scan at the vertical centre is shown in Fig 8.21. Due to the setup of the plasma cell and the holder of the measurement fiber, the longitudinal measurement range is limited to the central 64 mm of the 100 mm discharge vessel. Data was taken 20 µs after

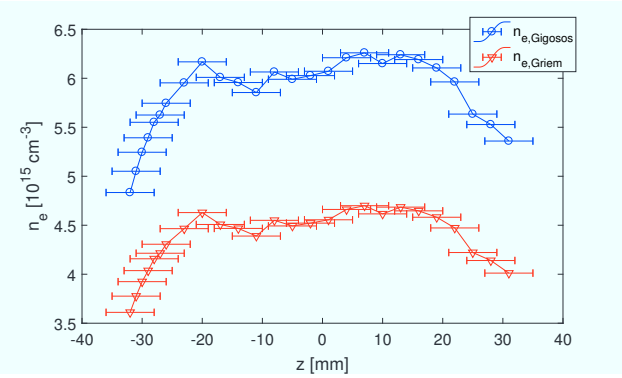

Figure 8.21: Density profile in the gas discharge plasma along the axis of electron beam passage. The cathode surface is situated at (-51±2) mm, the anode at (+51±2) mm.

discharge ignition. A significant drop in density is apparent at both ends of the plasma column. Density profiles observed immediately after the end of the discharge current pulse do not show this characteristic but only exhibit a slight density increase from cathode to anode (see Fig. C.1). The difference is attributed to an outflow of gas through the beam apertures driven by the high pressures in the hot plasma compared to the ambient neutral gas (see also Appendix C).

Line profiles were measured with a changing delay between plasma ignition and camera gate time to gain information about the temporal development of the plasma density. Figure 8.22 shows the measured evolution of the plasma density in the vertical and longitudinal centre of the discharge vessel during the first 80 μs of the discharge. A nearly exponential decrease of the density is observed. After termination of the discharge current pulse the plasma is not heated further and thus the density development is dominated by recombination of free electrons and ions. No spectroscopic density measurement was possible after the shown time range as the signal strength (i.e. light emission from the plasma) was too low and the resulting line widths too small for reliable line-broadening analysis.

8.4.2 SMI-based density measurements

Plasma density measurement methods like spectroscopic analysis or interferometric techniques are a common tool due to their high space and time resolutions and in the case of spectrometry also easy setup. Nevertheless

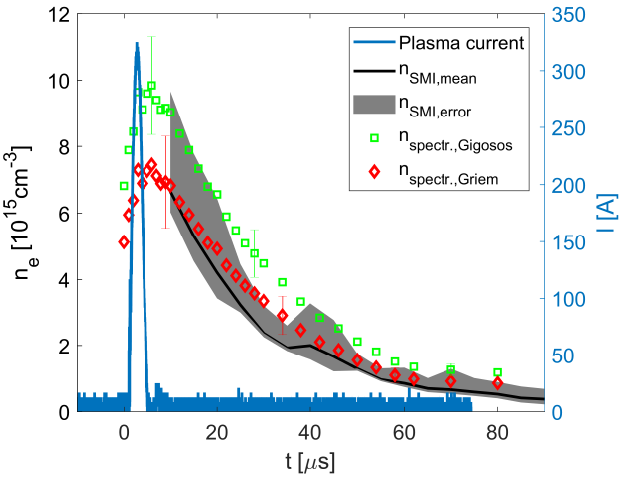

Figure 8.22: Measured discharge current and plasma densities according to the SMI-based and the two spectroscopic measurement methods. The gray area represents the maximum errors of all SMI-based density measurements at each timing t [194].

they share certain drawbacks, e.g. that the precise position of beam passage is often not known and therefore the density the beam interacts with has to be inferred up to a certain degree. The plasma medium of a PWFA can also be difficult to access in the accelerator environment due to space and safety constraints. Operation of complex setups like interferometers during PWFA experiments is therefore restricted. Especially in the PITZ case, the optical density measurement methods are only applicable in a small part of the density range in which experiments are conducted. As knowledge about the electron bunch as well as about the plasma characteristics is essential for the interpretation of PWFA experimental results, this would severely limit the information gain in these experiments. Therefore, a new method to measure the plasma density at the exact time and position of beam passage was proposed.

Figure 8.23 shows a 2D linear wakefield calculation for an ideal, transverse homogeneous, longitudinal flat-top electron bunch. The periodicity of the longitudinal fields excited by the bunch is exactly the plasma wavelength. This would allow to determine the plasma wavelength and therefore the plasma density by measuring the longitudinal phase space (LPS) of a flat-top electron bunch after interaction with the plasma. At the PITZ facility, flat-top electron bunches can be produced by shaping the photocathode

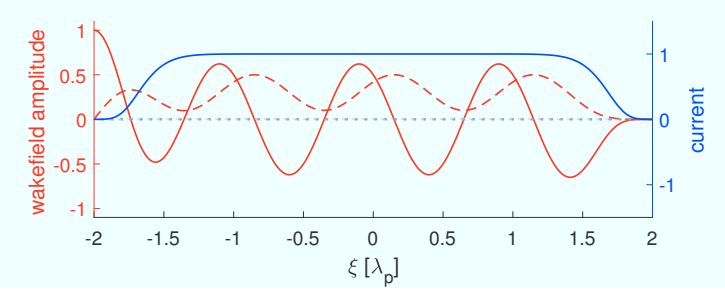

Figure 8.23: Longitudinal (solid red) and transverse (dashed red) normalised wakefields excited by a longitudinal flat-top bunch (blue) according to linear wakefield theory in the co-moving coordinate $\xi = z\text{-}ct$.

laser pulses to a longitudinal flat-top profile. Available beam diagnostics also allow single-shot LPS measurement. From the LPS of bunches with and without plasma interaction, the slice energy change due to the wakefield can be retrieved [212]. The periodicity is deduced from the Fourier spectrum of this slice energy change and the plasma density can be calculated according to Eq. (2.11).
Nevertheless, the transverse fields in Fig. 8.23 show inhomogeneities, also at the wavelength of the plasma. These lead to growth of the self-modulation instability (SMI), as detailed in Sec. 4.1.3. While it has been stated, that the periodicity of the microbunches formed by the SMI corresponds to the plasma wavelength [112], detailed studies of SMI growth have revealed complex dynamics due to a change in phase velocity in the wakefield [114].

Simulation of SMI-based density measurements

To evaluate the suitability of periodicity in the LPS of a self-modulated bunch as a means of measuring the plasma density, HiPACE simulations of the wakefield interaction of different flat-top electron bunches with various plasma densities have been performed. The flat top bunch shape has been chosen as it deviates least from ideal instability dynamics [114]. In accordance with the capabilities of the PITZ facility, parameters have been varied in the following ranges:

- unperturbed plasma density n_e: $10^{12} - 10^{16}\,\mathrm{cm}^{-3}$
- plasma length L_p: 100 mm
- mean bunch energy: 23 MeV

- bunch length: ca. 25 ps (full width at half maximum, FWHM)
- current rise time (10 – 90 %): (1 – 2) ps
- bunch charge: (100 – 1000) pC
- transverse size at plasma entrance $\sigma_{x/y}$: 0.1 mm - 0.5 mm (root mean square, RMS).

A small uncorrelated energy spread was shown to reduce the influence of the Hosing instability [109] with no reported or observed influence on the SMI development. The uncorrelated energy spread in the bunches was therefore set to 5 %. No correlated energy spread was introduced. A grid of $512 \times 256 \times 256$ cells has been used to simulate a box of $12 \times 1 \times 1\,\mathrm{mm}^3$ which is co-moving with the simulated electron bunch.
Figure 8.24 shows the evolution of a bunch undergoing SMI (a, b), the evolution of the slice energy modulations (c) and the Fourier spectrum of the slice energy change (d). A modulation into bunchlets is clearly visible in Fig. 8.24 (b). The bunchlets are formed at phases of focusing transverse fields. Due to the linear regime of the interaction and the consequent 90 ° phase offset between longitudinal and transverse fields this results in an energy change along every individual bunchlet with an overall sinusoidal energy modulation along the bunchlet train [Fig. 8.24 (c)]. After formation of the bunchlets, their wakefields add up towards the tail of the bunch, which can also be seen in Fig. 8.24 (c), where slice energy changes are shown for three different positions along the 100 mm long plasma channel: While at the start of the instability the slice energy modulations are nearly homogeneous along the bunch (25 mm, blue curve), they significantly grow towards the bunch tail in later stages (50 mm and 74.9 mm, red and yellow curves, respectively), which is caused by the resonant excitation of wakefields by the formed train of bunchlets. This general behaviour can be utilised to deduce the growth stage of the instability from the LPS modulations.

The density deduced from the modulations after the full plasma length is 1.5 % lower than the simulated one, while at 50 mm propagation length, the density that corresponds to the highest peak deviates by 16.5 % and the one of the second emerging peak by 7.3 % from the actually simulated density [Fig. 8.24 (d)]. This error is caused by the change of wakefield phase velocity during the evolution of the SMI [114]. Figure 8.24 (c) illustrates this effect: while the first period of the slice energy modulation is mainly changing in amplitude from 50 mm to 75 mm of plasma interaction, the following periods

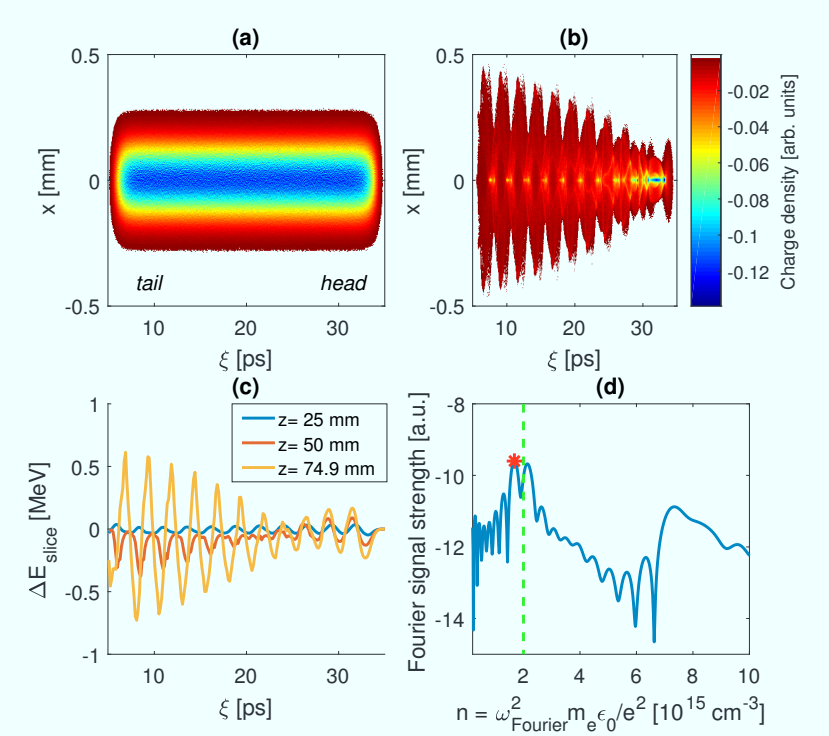

Figure 8.24: Simulated projections of a 530 pC bunch before the 2×10^{15} cm^{-3} plasma (a) and after 50 mm of propagation (b) in the x-ξ plane (ξ=z/c-t). Slice energy changes due to the driven wakefields at different positions in the plasma are depicted in (c). Subfigure (d) shows the Fourier spectrum after 50 mm propagation in the plasma, where Fourier frequencies have been converted to plasma densities n according to Eq. 2.11. The green line indicates the simulated plasma density, the red asterisk the density that would be deduced with the presented method [194].

are also changed in shape. Positions of the energy loss maxima along the bunch are changing significantly from beginning to end of the plasma.

To understand the development of the measurement accuracy, the ratio between simulated measurement and actually simulated density along the plasma for two different probe bunches is plotted in Fig. 8.25. While their charge is similar to the case depicted in Fig. 8.24, a different plasma density and two different initial transverse bunch sizes were simulated. In both cases the measured density drops significantly due to the phase velocity change during the bunchlet formation. Nevertheless the onset of this drop happens much earlier in the plasma in the case of smaller transverse bunch size, which corresponds to a higher initial wakefield amplitude (due to higher

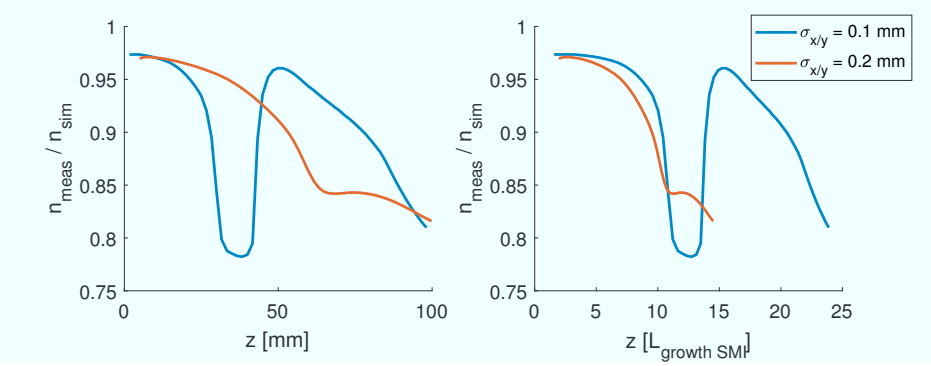

Figure 8.25: Evolution of simulated measured plasma density n_{meas} relative to the actually simulated density n_{sim} of $0.5\times10^{15}\,cm^{-3}$ along the plasma for two different probe bunches, with 510 pC, 27 ps FWHM length. The transverse RMS size $\sigma_{x/y}$ of the bunches at the entrance into the plasma was varied and the curves are measured in geometrical distances (left) and SMI growth lengths (right).

bunch charge density), i.e. stronger seed of the instability. The growth of the SMI is characterised by the number of e-foldings that the instability has developed at the tail of the bunch [see Eq. (4.1)]. This number of e-foldings corresponds to the number of instability growth lengths the bunch has traveled in the plasma. In terms of this instability growth lengths $L_{growth\,SMI}$, the transition takes place in the same phase of the SMI development (see Fig. 8.25, right plot).
Subsequently, a step in the plasma density, that is deduced from the simulation data, towards better accuracy takes place. This corresponds to the appearance of the second (right) peak in Fig. 8.24 (d). The reason is assumed to be that the separation between bunchlets at this stage is again close to one plasma wavelength, whereas the positions of the bunchlets are slightly different from their positions at the beginning. Therefore a peak close to the actual density arises after build-up of the bunchlets, in addition to the peak that originates from the modulations imprinted on the LPS prior to the phase transition. While the second peak does not necessarily emerge at densities higher than the actually simulated (compare Fig. 8.25), the density was always found to be significantly closer to the actual density. No clear pattern for the exact density relation was found in simulations at various beam/plasma parameters, though.
The second, slower drop in accuracy is partially caused by further phase slippage and partially by the increasing transverse offsets of defocused bunch

particles: Particles that are too far off axis do not experience significant longitudinal fields and therefore do not change their energies significantly anymore. As they are still considered in the LPS measurements, they distort the LPS modulation shape and influence the measurement result.

Similar behaviour was observed in all simulated self-modulating bunches. In

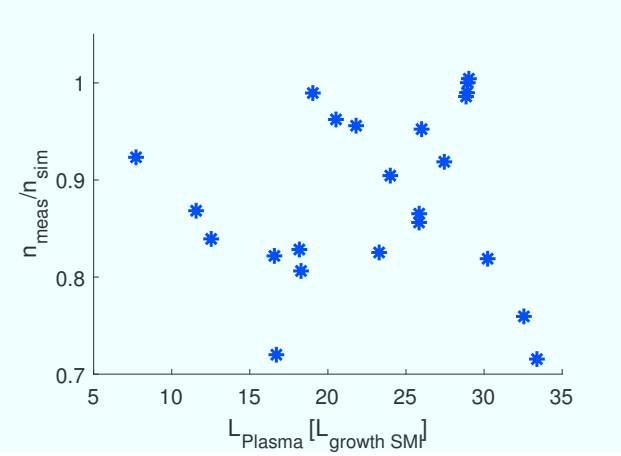

Figure 8.26: Simulated measurement accuracy after the full plasma measured in SMI growth length of the individual simulated bunches.

contrast to the agreement between the two cases shown in Fig. 8.25, it was not possible to find an unambiguous, general correlation between measurement accuracy after the full plasma length and growth stage of the SMI at the end of the plasma, for all simulated bunch/plasma parameters. The simulated measurement accuracy after the full plasma, measured in SMI growth lengths of the individual bunches, is plotted in Fig. 8.26. No significant correlation is apparent in the simulated data. Separating the simulated measurement accuracies by the input parameters (bunch charge, initial transverse size, plasma density, etc.) did also not yield a clear correlation or an explanation for the differing results. The maximum simulated deviations from the actual plasma densities of $^{+5}_{-30}$ % are therefore considered as an intrinsic measurement uncertainty if no dedicated simulation of the measurement parameters was performed. This corresponds to an error of $^{+42}_{-5}$ % for the plasma density measured with the introduced, SMI-based method [194].

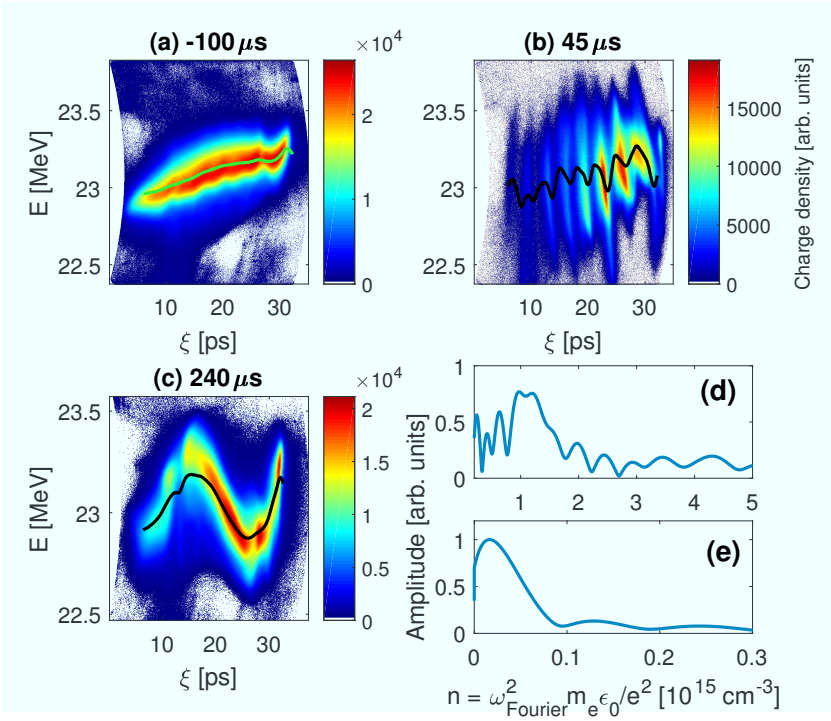

Figure 8.27: Non-interacting (a) and self-modulated electron beams (b, c) with mean slice energy [(a) green line; (b, c) black lines] at indicated delays to discharge ignition. The Fourier spectra for the two modulated beams are shown at high plasma density (d) [corresponding to (b)] and low plasma density (e) [corresponding to (c)] [194].

SMI-based density measurement results

Plasma density measurements based on the method introduced above were performed using the TDS and dipole spectrometers of the PITZ beamline. After dispersing the bunches in time (vertically) and energy (horizontally), a LYSO scintillator screen was inserted into the trajectory. Ten consecutive transverse projections on this screen were recorded for every measurement parameter. After subtraction of the mean of ten background images, taken before every beam measurement, the chromaticity due to the broad energy range was corrected in the LPS. This was necessary due to the sometimes large energy spread after SMI interaction and resulting strong tilts in the LPS, which led to partial overlap of temporal slices of the bunch. Correction was done by applying a temporal offset to the time calibration of every pixel

according to

$$\Delta t = a \cdot (E - \overline{E}) + b \cdot (E - \overline{E})^2 \ , \tag{8.7}$$

where a and b are empirically determined factors and $(E - \overline{E})$ the pixel's energy offset from the mean energy of the bunch.
Figure 8.27 shows three LPS measurements without (a) and with (b, c) interaction with the argon discharge plasma at indicated delays after discharge initiation. The modulation period is changing significantly from high densities [short delays, (b)] to low densities [long delays, (c)]. As mentioned before, this is caused by recombination of ionised particles. To determine the plasma density, mean slice energy changes are calculated in a similar manner as for the simulated bunches and a Fourier spectrum analysis is performed.
The Fourier spectrum at low density [Fig. 8.27 (e), with frequencies converted to corresponding plasma densities] shows a clear peak at $2 \times 10^{13}\,\mathrm{cm}^{-3}$ and low amplitude side bands. At high plasma densities [Fig. 8.27 (d)] determination of the plasma density is more complex: The appearance of a second peak at $1.2 \times 10^{15}\,\mathrm{cm}^{-3}$, slightly higher than the density at the highest signal (ca. $1 \times 10^{15}\,\mathrm{cm}^{-3}$), can be seen, as was found in the simulations for cases in which the energy modulation is evolving after the transition of phase velocity during self-modulation [compare Fig. 8.24 (d)]. As these peaks were simulated to be closer to the actual density, the peak at $\sim 1.2 \times 10^{15}\,\mathrm{cm}^{-3}$ is taken into account in this case.
The linear character of the wakefield can be observed in Fig. 8.27 (c). Below $\xi \approx 15\,\mathrm{ps}$ the signal intensity drops significantly compared to preceding slices. As shown in Sec. 2.2, transverse and longitudinal wakefields exhibit a $90\,^\circ$ phase offset in the linear regime. Thus a sign-change in the transverse forces is expected at the maximum of the longitudinal forces. In line with this expectation, a maximum energy gain is observed around 15 ps.
Similar measurements were performed for different bunch charges, transverse bunch sizes and plasma densities. The results are given in Fig. 8.28. A nearly exponential decay is observed until $\sim 250\,\mu\mathrm{s}$ after discharge ignition. At delays higher than $\sim 350\,\mu\mathrm{s}$ the plasma frequency can hardly be resolved from low frequency noise in the Fourier spectra. This is caused by low signal amplitudes (i.e. slice energy changes) and by the fact that at such low plasma densities the probe bunches are shorter than half a plasma wavelength. Nevertheless, the measurement range is significantly extended in comparison to the spectroscopic measurement range. In the common measurement range good agreement between the two methods is found as shown in Fig. 8.22.
Beside the extended measurement range the method is also advantageous as

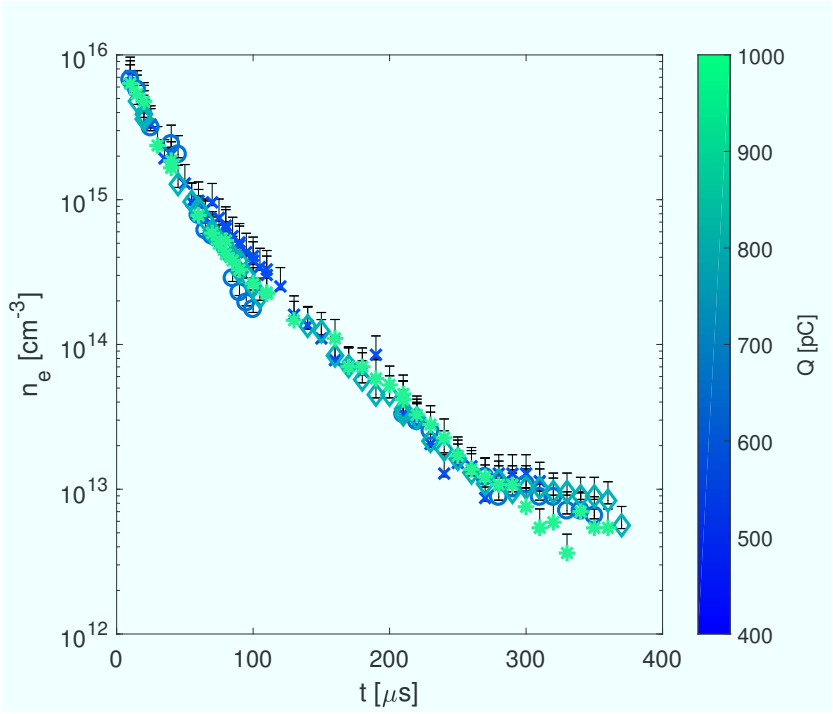

Figure 8.28: Plasma electron densities for varying delays t after discharge ignition. Measurements were performed with different bunch charges Q.

- no measurement equipment other than the existing tools for PWFA experiments is needed
- measurements are done in-situ, which is especially important in case of (unintended or deliberate) changes of the plasma cell parameters (gas pressure, voltage, etc.)
- the measurement takes place at the very position of beam passage
- errors due to the plasma temperature are negligible in non-relativistic plasmas
- the method is independent of the gas species, i.e. plasma composition
- sub-nanosecond time resolution is possible for cm-scale plasmas.

Compared to measuring the plasma density by counting the wake periods in the LPS of self-modulated bunches (or their number of microbunches) the

presented Fourier analysis method allows measurement of densities at which the probe bunch length is smaller than half a plasma wavelength. At such densities only one microbunch remains after SMI and fractions of periods are difficult to determine without detailed analysis by Fourier transformation.
Despite its advantages, longitudinal density profile measurements are not possible with the SMI-based method. It is therefore proposed as a versatile complementary tool to overcome limitations of other density measurement techniques.

Chapter 9

Beam dynamics simulations

Prior to acceleration experiments, the capability of the PITZ facility to drive a high transformer ratio (HTR) plasma wakefield accelerator was evaluated in numerical simulations. First simulations on the originally proposed ramped bunch train scheme quickly led to the discontinuation of work on this scheme (due to the reasons detailed in Sec. 3.2) in favour of single shaped bunch scenarios (see also Sec. 3.2). The results of the simulations for the latter are detailed in the following sections. After the simulations of shaped bunch extraction from the cathode and beam transport to the position of the plasma acceleration medium, the transport through the plasma will be discussed. Expected measurement results conclude the simulation studies.

9.1 Bunch extraction and transport to plasma

In addition to the studies presented in Sec. 7.2, ASTRA simulations of achievable bunch shapes for the PITZ electron gun parameters were performed. After studying the convergence of simulation results, simulations were usually performed with 500 000 macroparticles and with 3-dimensional space charge calculation starting at the exit of the gun cavity on a grid of $64 \times 16 \times 16$ cells size. Several simulated bunch shapes at the entrance of the PITZ plasma are shown in Fig. 9.1. The profile of the photocathode laser pulse was shaped such that different HTR-capable bunch profiles (see Sec. 3.2) are achieved. Due to space charge effects at the cathode, the bunch current profiles deviate from the photocathode laser pulse profiles. Especially the linearity of the long current ramp is modified significantly, which can lower the transformer ratio (TR). To precompensate such deviations,

the input particle distributions were modified in a manual feedback. The possibilities of such precompensation are shown in the "Double triangular" (initially linear ramp) and "Double triangular FB" (precompensated initial bunch profile) curves in Fig. 9.1. Slight further optimisation was achieved in some cases by setting the phase of the bunch in the gun cavity such, that the slice of highest charge is accelerated at the maximum mean momentum gain (MMMG) phase, which corresponds to MMMG-phase minus 2 degrees in ASTRA for the whole bunch.

In parallel to the optimisation of the longitudinal bunch profiles, the beam

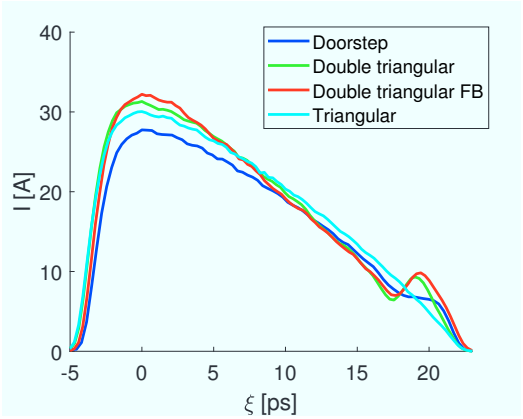

Figure 9.1: Simulated bunch current profiles at the plasma entrance for 500 pC bunches extracted with different longitudinal photocathode laser profiles.

transport to the plasma cell was investigated. Four quadrupoles are available in the PITZ beamline between booster cavity and plasma. Beside these, the gun solenoid provides tunable focusing upstream of the plasma cell. Focusing forces are also present in the booster cavity, but as a maximum energy gain is pursued, these forces are fixed. ASTRA is capable of simulating quadrupoles and also the non-axisymmetric space charge forces in bunches that have different sizes in the two transverse planes, and could therefore in principle also be used to optimise the focusing of beams at the plasma entrance. Nevertheless, many simulations have to be performed for such an optimisation. As ASTRA tracks particles and calculates space charge forces in a PIC routine, it consumes rather large amounts of computational resources. To reduce the required computation time, optimisation of the bunch focusing was therefore done with the linear matrix algorithms MAD-X and SCO, as well as by manual tuning of linear matrix transport pa-

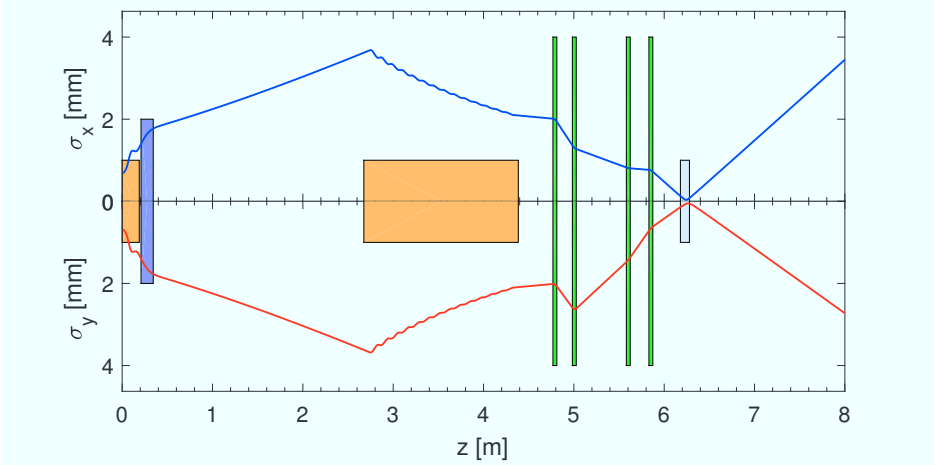

Figure 9.2: Simulated RMS bunch size in x (top) and y (bottom) as a function of the bunch position along the PITZ beamline for 500 pC bunch charge. Coloured rectangles represent the positions of gun and booster cavities (orange), the gun main solenoid (blue), quadrupoles upstream of the plasma (green) and the plasma (grey).

rameters. The acquired magnet parameters were then used to simulate the beam transport including space charge forces in ASTRA. Figure 9.2 shows the result of such a simulation. A tight focus is achieved in the plasma cell. Downstream quadrupoles, which are used to catch the highly divergent beams are not shown. Using different quadrupole settings, the focus size and position can be changed, though changing the gradient of one quadrupole necessitates tuning of the other quadrupoles as well to maintain a symmetric focus. Changes of several 10 A in the gun main solenoid current do not change the focal spot RMS size significantly as the magnet is quite far away from the focal plane. Yet, as shown in Fig. 9.3, it allows to shift the position of the bunch focus by several centimeters without major influence

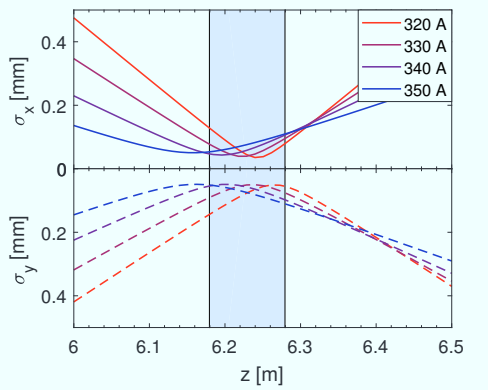

Figure 9.3: Simulated x (top) and y (bottom) RMS bunch sizes at the plasma (grey area) for varying gun main solenoid current at 500 pC bunch charge.

on the focus symmetry. No screen is available at the plasma entrance in the PITZ beamline to fine-tune the focus during experiments. The symmetric focus shift by changing the solenoid current therefore is an important finding which was confirmed in preparatory experimental beam transport studies, where a screen station was installed at the position of the plasma cell.
Projections of the 2D charge densities of the bunches reveal that this focus shift corresponds to shifting the focus along the bunch. Figure 9.4 shows the charge densities for the RMS trajectories displayed in Fig. 9.3. While at lower currents the tail slices are still convergent, they are focused at high currents, where the front slices are already diverging. The asymmetries in

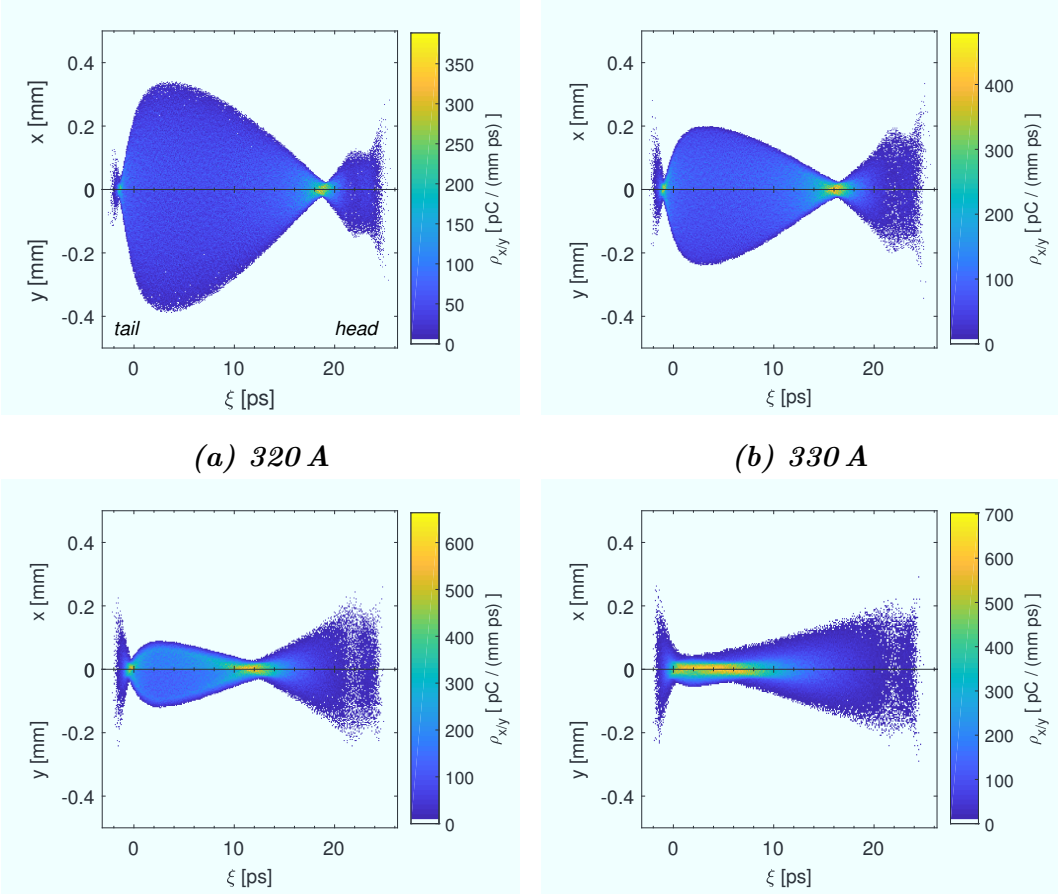

(a) 320 A *(b) 330 A*

(c) 340 A *(d) 350 A*

Figure 9.4: Simulated 2D charge projections in the x- and y-ξ planes at the plasma entrance for different gun main solenoid currents.

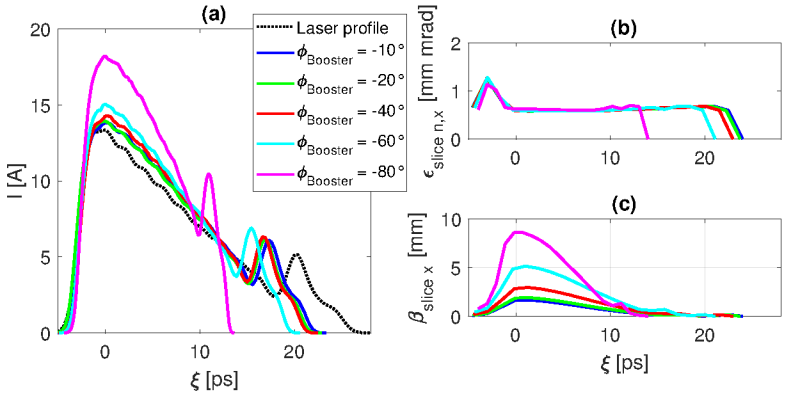

Figure 9.5: Bunch current profile (a), slice emittance (b) and slice beta-function (c) for bunches accelerated at different phases in the CDS booster cavity up to the plasma entrance. Phases are given with respect to the booster MMMG phase.

focus between x and y can be corrected by further quadrupole tuning but were also found to be sufficiently small for subsequent PWFA studies.

In further beam transport studies the phase of the booster cavity was scanned to determine whether higher bunch currents can be provided by ballistic compression of the driver bunch. Such compression is achieved by introducing a negative energy chirp to a bunch, i.e. the bunch tail has higher energy than the bunch head. This is achieved via off-crest acceleration in the booster cavity. Resulting differences in particle velocities allow tail particles to catch up with head particles and hence the bunch is compressed. Figure 9.5 (a) shows that only moderate increase of the maximum slice current can be achieved by ballistic bunching. To distinguish bunch distortions introduced by compression from distortions due to space charge, simulations were performed for rather low bunch charges of 200 pC (note the linearity of the bunch current ramp). While the slice emittance is not affected by compression [Fig. 9.5 (b)], the beta function of slices around the current maximum increases significantly for increasing compression [Fig. 9.5 (c)]. As shown in Fig. 7.4, increasing bunch charge also aggravates the slice mismatch. The significant mismatch present in compressed low-charge bunches is therefore assumed to further increase for higher bunch charges. Inhomogeneous slice focusing was found to be the most prevalent issue in achieving stable transport of the driver bunch through the plasma. As the gain in maximum current by compression is only moderate, further studies were performed without ballistic compression.

9.2 Beam transport in plasma

To simulate the interaction of the PITZ electron bunches with plasma, HiPACE was used. For several individual cases additional simulations using PAMASO [213] were conducted to validate the HiPACE simulation results. Good agreement between the two codes was found in the treated cases [214]. Preliminary HiPACE studies were performed to define standard simulation parameters. Input parameters like particle count and grid resolution were varied, to identify the setup which consumes minimum computational resources while still delivering similar results as simulations with higher resolution. According to the results of these studies, a simulation grid of $512 \times 256 \times 256$ cells was typically simulated and at least 500,000 macroparticles were used to model the bunches of the PITZ accelerator.
Initial high transformer ratio PWFA simulation studies for PITZ were performed without witness bunches. This allowed to reduce the complexity of the simulation setup, to reduce the computation time, and to scan plasma parameters in a timely manner. As the wakefield is not influenced significantly in the case of negligible witness beamloading, the TR is independent of the presence of a witness bunch of low charge.

Plasma densities were initially chosen around the maximum plasma density of $10^{15}\,\mathrm{cm}^{-3}$ which was targeted with the PITZ plasma cells for self-modulation experiments. According to Eq. (3.8), the highest available densities would also produce the highest possible TR, as the bunch length measured in plasma wavelength increases.
The current filamentation instability (see Sec. 4.1.1) is naturally mitigated even at high densities by the tight focus of the driver bunch: at a density of $10^{15}\,\mathrm{cm}^{-3}$ bunch sizes given in Fig. 9.3 correspond to $k_p\sigma_r \approx 0.5$, which is significantly lower than the empirical limit for the instability to occur.
Direct evaluation of whether the beam density at the plasma entrance exceeds the unperturbed plasma electron density was found to be an inadequate measure for identifying scenarios of stable beam transport free of the self-modulation instability: While charge excess of the beam in plasma is the precondition for nonlinear interaction, this can also be fulfilled by bunches which exhibit insufficient density at the plasma entrance. During the wakefield interaction, the bunch can be self-focused by its own transverse wakefields. Thus, only numerical PWFA simulations allow to determine whether

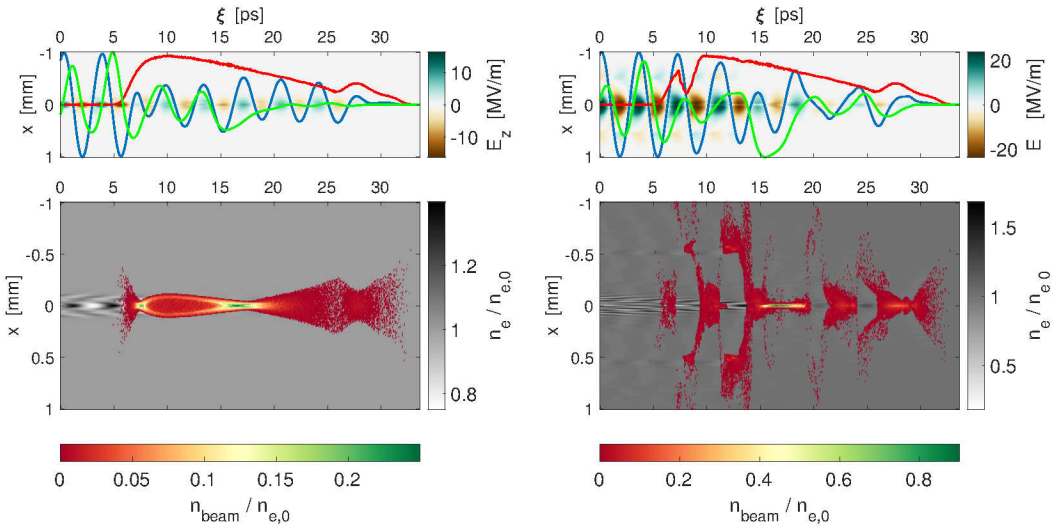

Figure 9.6: Simulation results for the PWFA interaction of a 500 pC double-triangular driver bunch with a plasma of unperturbed electron density $n_{e,0} = 10^{15}\,cm^{-3}$ in the co-moving frame ($\xi = z/c - t$) at the entrance (a) and close to the exit (b) of the plasma, at a main solenoid current of 340 A. The top plots show the electrical field distribution in the x-ξ-plane close to the axis (colour scale), bunch current profiles (red line), longitudinal fields on axis (blue line, shares axis of colour bar) and transverse fields close to the axis (green line, in arbitrary units). The lower plots show beam (colour scale) and plasma electron densities (grey scale) in the x-ξ-plane close to the axis. Bunches are propagating from left to right.

stable transport is achieved or not. The length of the plasma was assumed to be equal to the 100 mm distance of the electrodes in the gas discharge plasma cell. A propagation length corresponding to a multiple of the plasma skin depth close to this assumed plasma length is simulated (hence the slightly deviating final simulation lengths at different plasma densities).
Figure 9.6 shows simulation results for the interaction of a double-triangular driver bunch with a plasma of $10^{15}\,\mathrm{cm}^{-3}$ electron density. A bunch charge of 500 pC was simulated in this case. While other longitudinal bunch profiles and charges were also investigated, simulations with 500 pC double-triangular driver bunches first resulted in an experimentally realisable scheme of an HTR PWFA at PITZ. Beam densities at the entrance of the plasma, which are depicted in Fig. 9.6 (a), are much lower than the plasma density. Moreover, the transverse fields are partially defocusing (positive polarity on colour

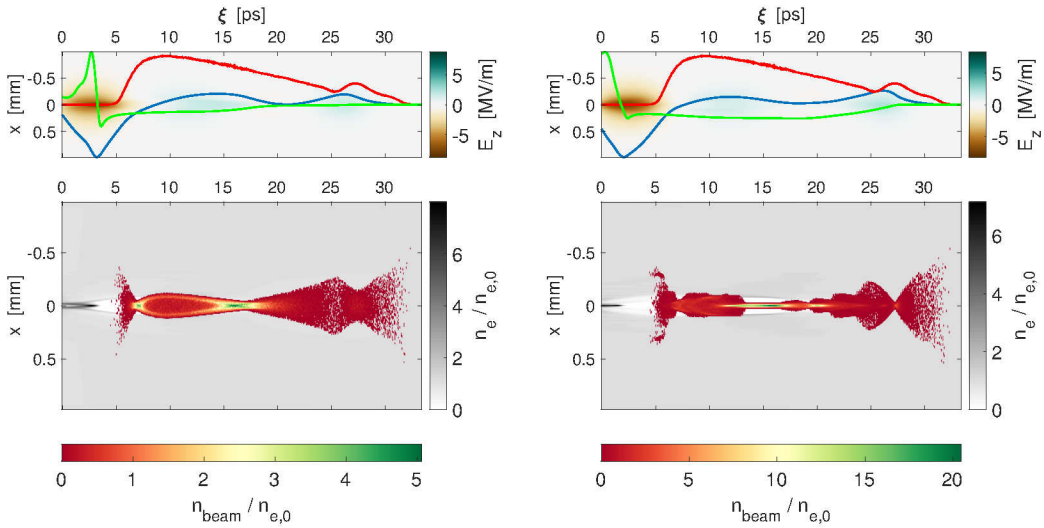

Figure 9.7: Simulation results at entrance (a) and exit (b) of a plasma of unperturbed electron density $n_{e,0} = 5\times 10^{13}\,cm^{-3}$ at main solenoid current of 340 A. Depiction as detailed in Fig. 9.6.

bar axis, Fig. 9.6 (a) top, green line) in the bunch. Correspondingly, self-modulation deteriorates the transverse profile of the bunch significantly during propagation through the plasma [Fig. 9.6 (b)]. Some beam electrons have even left the simulation box transversely at the plasma end ($z = 94\,\mathrm{mm}$), which is apparent in the current profile.

Similar results were obtained for other densities above $10^{14}\,\mathrm{cm}^{-3}$, while results differ for lower densities: At a plasma density of $5 \times 10^{13}\,\mathrm{cm}^{-3}$ the transverse fields are focusing all along the bunch (negative polarity on colour bar axis), as shown in Fig. 9.7. The bunch is not self-modulated at the end of the plasma [Fig. 9.7 (b)] which would allow acceleration of charge in the mildly nonlinear plasma wake behind the bunch.

To determine the transformer ratio, the maximum accelerating field behind the bunch was divided by the maximum decelerating field within the bunch. This corresponds to the original TR definition. Observation of this value at different time steps in the plasma yields the results shown in Fig. 9.8. Along the plasma both the TR and the maximum accelerating field are varying. This is caused by bunch envelope oscillations, which result from improper matching of the slice Twiss-parameters to the focusing forces of the wake-

field [see also descriptions to Eq. (7.4)]. Such variations cannot be mitigated in the current setup at PITZ due to the constraints described in Secs. 9.1 and 7.2. Therefore, an average field-weighted TR was introduced as a figure of merit for evaluating the expected measured TR:

$$R_w = \frac{\int_0^{L_{plasma}} E_{z,max}(z) \cdot R(z) dz}{\int_0^{L_{plasma}} E_{z,max}(z) dz} \ , \tag{9.1}$$

where $E_{z,\,max}(z)$ is the maximum accelerating field at different positions z in the plasma, L_{plasma} is the length of the interaction, and $R(z)$ is the transformer ratio at position z along the plasma. Weighting the TR with the corresponding accelerating field accounts for the fact that high accelerating fields make higher contribution to the final bunch energies. For the case shown in Figs. 9.7 and 9.8, $R_w = 4.0$, which is twice the linear limit.

Further simulations without witness bunch were conducted to assess the sensibility of the TR to experimental deviations from the simulated bunch shape and plasma parameters and to identify conditions for higher TRs. In accordance with the finding from the previous section, the longitudinal bunch slice with maximum focusing is varied by changing the solenoid current within a range of several 10 A. While as a prerequisite for stable transport a tight overall focus of the bunch must be maintained, the slice focusing can also have significant impact on the TR. Examples of such varied focusing are shown in Fig. 9.9. The simulated bunch distributions at the plasma entrance correspond to Figs. 9.4 (c) and (d), respectively. Final bunch density distributions differ significantly for the two cases, as do the weighted TRs of $R_w = 4.6$ for 340 A and $R_w = 5.1$ for 350 A. Similar TR variations were observed for slightly differing bunch profiles. Nevertheless, by slightly changing solenoid and plasma densities for such a modified bunch profile, similar TRs as without bunch profile changes were obtained again. After optimisation of the solenoid focusing it was also possible

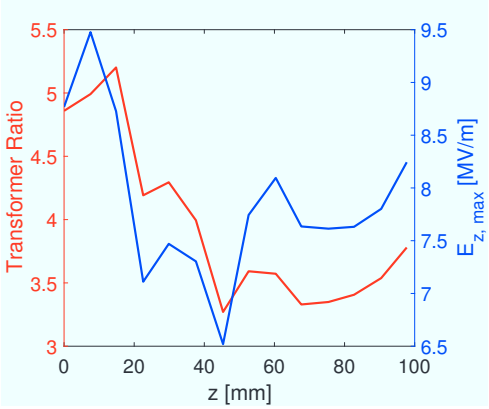

Figure 9.8: Simulated transformer ratio and maximum accelerating voltage behind the bunch along the plasma.

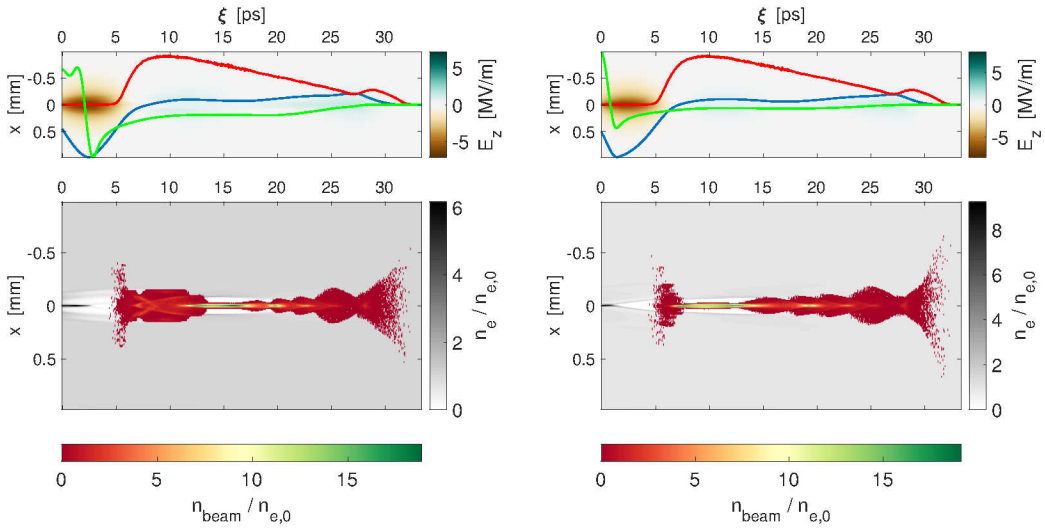

(a) $I_{main} = 340\,A$ ***(b)*** $I_{main} = 350\,A$

Figure 9.9: Simulated x-ξ-plane of PWFA interactions, 98 mm into the $5 \times 10^{13}\,cm^{-3}$ *plasma for different main solenoid currents. Depiction as detailed in Fig. 9.6.*

to achieve stable transport of the driver bunch at plasma densities up to $10^{14}\,\mathrm{cm}^{-3}$ for various profiles in simulation. Scanning both the plasma density and the solenoid focusing was therefore foreseen in experiment to achieve optimal matching of bunch focusing and plasma wake for the experimentally achieved bunch profile, to observe the highest possible TR.
The conducted simulations did not yield a clear upper limit for the TR achievable at PITZ. Due to the slice focusing mismatch and the resulting betatron oscillations within the driver bunch (which causes erratic changes of the wakefield shape, i.e. of the TR), no definite pattern for achieving higher TRs could be identified. For driver bunches with finite slice energy spread, the slice emittance grows in the betatron oscillations until it would finally fulfill Eq. (7.4). This means that the beam envelope betatron oscillations would be damped and therefore the variation of the wakefield shape would also be reduced. Such an equilibrium is not reached in the PITZ plasma, as the length of the interaction is too short. The lengths of the plasma media are however constrained by the available space in the PITZ beamline and the resulting maximum plasma cell size.
Nevertheless, the simulations revealed possibilities to mitigate effects that

prohibit high transformer ratio PWFA and confirmed that driving HTR fields is possible with the given driver beams and plasma media.

9.3 Simulation of measurements

To assess the transformer ratio of a PWFA, which is defined as the ratio between the maximum accelerating fields behind the driver bunch and the maximum decelerating fields within the driver bunch [see Eq. (3.1)], the amplitudes of the driven fields would have to be measured. As these are hardly accessible in experiment, the energy gain of a witness bunch, trailing the driver bunch in the plasma, and the slice energy loss of the driver are measured instead. From these energy changes an effective transformer ratio is calculated:

$$R_{eff} = \frac{\Delta_{max} E_{witness,\ max}}{\Delta_{max}(-E_{driver,\ slice-mean})} \ , \tag{9.2}$$

where $\Delta_{max} E_{witness,\, max}$ is the maximum change of the maximum witness bunch energy. Correspondingly, $\Delta_{max}(-E_{driver,\, slice-mean})$ is the maximum loss of the mean slice energies within the longitudinal slices of the driver bunch. The change of the maximum witness energies is considered, as the witness bunch length at PITZ is fixed at ca. 2.5 ps FWHM. At a plasma density of e.g. $10^{14}\,\mathrm{cm}^{-3}$ this bunch length results in a wake phase range of more than 80 degrees, which is experienced by witness bunch particles (see also Fig. 9.10). The witness bunch of a PWFA for applications would be significantly shorter, to provide sufficiently low final energy spread. Such an optimised witness bunch would be placed at the phase of maximum energy gain, which is why the maximum gain in the maximum energy is considered in the present experiment.
In case of the driver, the energy depletion of a full slice is considered critical for maintaining further stable acceleration, as the loss of a slice would modify the bunch profile and therefore also the wakefield it drives. Hence, the mean slice energy is taken into account to calculate the transformer ratio. Infinitesimal slice length was used in simulations. As the variation of the wakefields within the driver takes place on length scales of the plasma wavelength, infinitesimally long slices are considered equal to the finite slice resolution of the experiments as long as the latter is significantly lower than the plasma wavelength, which was the case in all conducted experiments. R_{eff} is calculated from the wakefields integrated over the full length of interaction for each individual bunch slice. It therefore slightly differs from

the weighted transformer ratio defined in Eq. (9.1), which was utilised to optimise the driver bunch parameters in simulation. For the application of a PWFA, the maximum particle energy gain of the witness per invested driver particle energy is the relevant parameter to describe the maximum possible acceleration. As this is described by the effective transformer ratio, R_{eff} is considered the appropriate figure of merit to describe the transformer ratio experimentally, also in accordance with Refs. [70, 133].
To determine R_{eff} at PITZ, bunches are transported to the first screen station in the second high energy dispersive section (HEDA2, see Fig. 10.1). Here, the longitudinal phase space can be measured and thus energy changes of the witness and of the driver bunch slices can be observed.
Simulations were conducted to assess how accurate the transformer ratio can be reconstructed from the measured witness and driver bunch parameters. The experimental technique to deliver the witness bunch from the cathode is described in Sec. 7.2. In simulations, a short Gaussian bunch with a variable delay was added to the charge profile that is initialised at the cathode in ASTRA. The bunch profiles at the entrance of the plasma are shown in Fig. 9.10 (a). Focus mismatch of slices of different space charge also causes

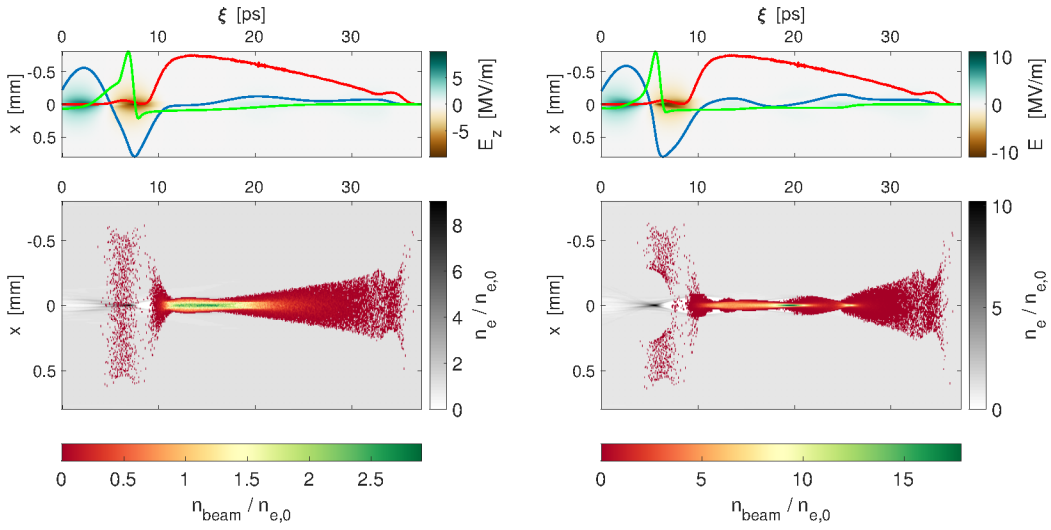

(a) z = 0 mm *(b) z = 27 mm*

Figure 9.10: Simulation results for driver (right, $\xi \geq 10\,ps$) and witness (left, $\xi \approx 7\,ps$) bunches at different positions z in the $10^{14}\,cm^{-3}$ plasma. Depiction as detailed in Fig. 9.6.

the witness bunch to be much less focused than the high charge slices of the driver. As the stable transport of the driver defines the bunch focusing, no improvement on the witness size at the plasma entrance is possible. This deteriorates the witness bunch phase space significantly and would thus be unacceptable for a PWFA machine that delivers bunches for further applications. In the present work, the aim is to measure the transformer ratio, i.e. the amplitude of the accelerating and decelerating fields. Therefore, the acceleration of a fraction of the witness electrons is sufficient to probe the wakefield at the witness position.
Figure 9.11 shows the simulated LPS of the beam with and without plasma interaction directly after the plasma position. The effective transformer ratio

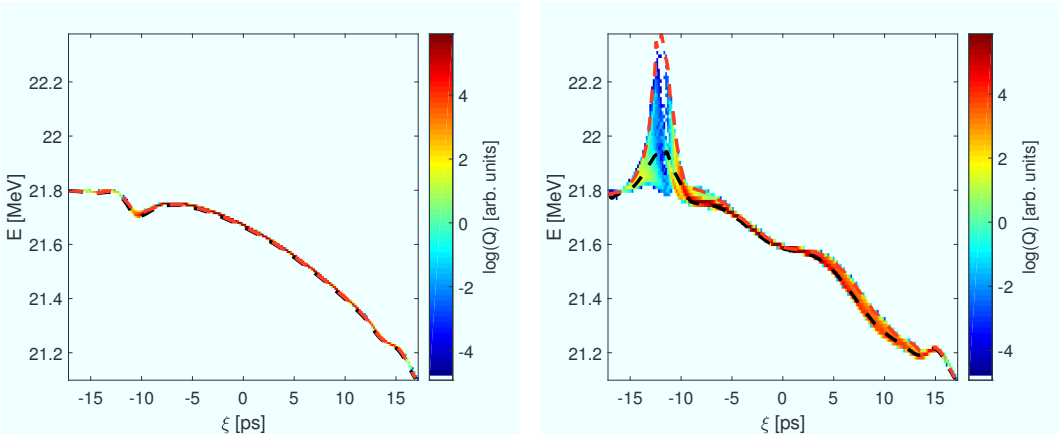

(a) without plasma ***(b) with plasma***

Figure 9.11: Simulated longitudinal phase space of the beam at the end of the plasma cell without (a) and with (b) plasma interaction. Charge density is shown in logarithmic scale to resolve the witness bunch around $\xi \approx$ -13 ps. Black and red dashed lines show the mean and maximum particle energies in every slice, respectively.

calculated according to Eq. 9.2 from these distributions is $R_{eff} = 4.8$.
To simulate the measurement accuracy, the particle distributions were tracked further down the PITZ beamline using ASTRA. Beam transport was optimised using MAD-X, SCO as well as manual tuning of quadrupoles. The simulated measurement of the longitudinal phase space, using diagnostics available at PITZ (vertically deflecting TDS cavity and HEDA2 horizontal dipole spectrometer; see Fig. 10.1), is shown in Fig. 9.12. While especially the time resolution of the spectrometer is diminished by the transverse bunch

size of the beam at the measurement screen, the relative numbers, i.e. the energy changes, can be retrieved rather precisely from the simulated measurement data. Calculation of the effective transformer ratio from the simulated measurement yields $R_{eff} = 4.6$. The good agreement within 4 % proves the capability of the PITZ facility to not only drive a HTR PWFA but also to extract the achieved transformer ratio accurately from the measurement data.

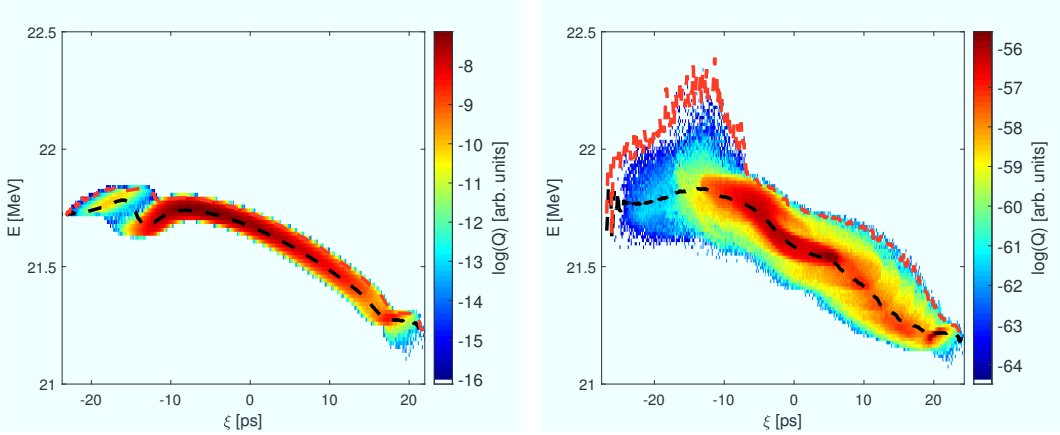

(a) without plasma ***(b) with plasma***

Figure 9.12: Simulated measurement of the longitudinal phase space of the beam without (a) and with (b) plasma interaction in the second high energy dispersive arm (HEDA2) of the PITZ beamline. Charge density is shown in logarithmic scale to resolve the witness bunch at $\xi \approx$ -20 ps. Black and red dashed lines show the mean and maximum particle energies in every slice, respectively.

Chapter 10

Experimental demonstration of HTR PWFA

Following the successful demonstration of photocathode laser based shaping of HTR-capable bunches, the commissioning of the gas discharge plasma cell and the simulation results with the achieved beam and plasma parameters, HTR PWFA experiments were conducted at PITZ. This chapter comprises the experimental results of these measurements. After discussing the experimental setup and the observation and mitigation of beam-plasma instabilities, the first experimental demonstration of high transformer ratio plasma wakefield acceleration will be described. This demonstration is validated with numerical simulation of the measured beam parameters. Finally, further experimental observations are detailed. The chapter is partially based on results published in Ref. [215].

10.1 The experimental setup

After installation of the gas discharge plasma cell in the PITZ beamline, a beam timing and trajectory which provided bunches similar to the ones defined in simulations at first had to established. With the initial, arbitrary laser pulse shape, the timing of the photocathode laser pulses to the RF phases of gun and booster cavity was set such, that the accelerated bunches acquire the maximum mean momentum gain (MMMG) in the dispersive sections LEDA and HEDA1 (see Fig. 10.1). This MMMG phase was re-measured after optimisation of the bunch shape and finally the bunch-

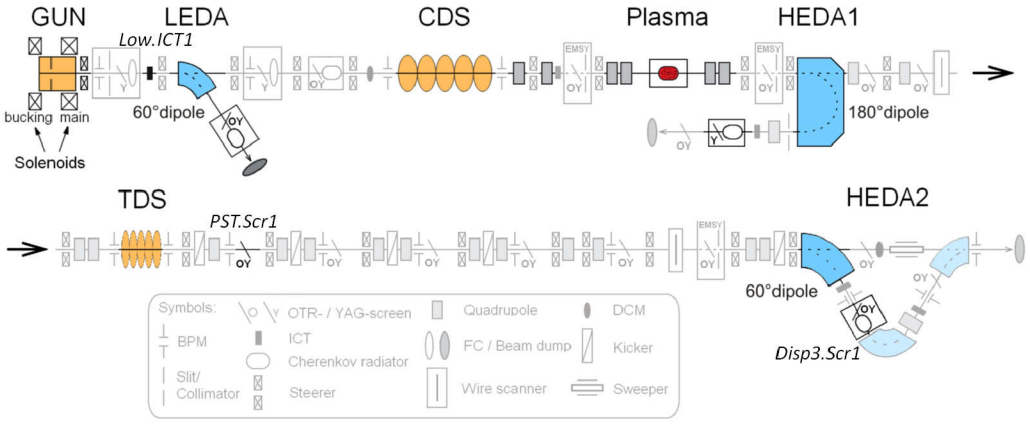

Figure 10.1: PITZ beamline with highlighted main components for driving and measuring high transformer ratio wakefield acceleration. Bunches are accelerated in gun and CDS booster cavities, drive and experience wakefields in the plasma and are dispersed in time and energy by the vertically deflecting TDS cavity and the horizontally dispersing HEDA2 dipole, respectively. The longitudinal profile is measured on PST.Scr1, the longitudinal phase space of the bunches is observed on the first screen station in HEDA2 (Disp3.Scr1).

RF timing setpoint was set to MMMG phase plus 2 degrees, to adjust the longitudinal phase space to the conditions of the simulations (see Sec. 9.1). 6.5 MW and 3 MW of RF power were coupled into gun and CDS booster cavities, respectively. The corresponding rms beam particle energies were 6.7 MeV and 23 MeV. As no screen station is available at the plasma position while the discharge cell is mounted, gun solenoid and quadrupole currents around the plasma cell for a tight focus at the plasma entrance were defined in preparatory measurements: A YAG-screen had been installed at the centre position of the plasma cell in a previous run period of the accelerator, and the focusing had then been adjusted for the minimum transverse beamsize. After establishing a good focus at the first screen station downstream of the TDS cavity, the bunch shape was adjusted to resemble a double triangular current profile, by automated and manual tuning of the birefringent crystal based laser pulse shaper (see Sec. 7.2). During the longitudinal laser pulse shaping, the bunch charge was kept at ~ 100 pC, to reduce the effects of space charge on the bunch shape and the longitudinal profile measurements. Due to drifts in the longitudinal bunch shape, the shaping procedure was repeated several times throughout the experiments and bunch shapes are given for individual measurements below. The bunch charge was adjusted by in-

creasing the laser pulse intensity on the photocathode. This is realised by a half-wave plate with adjustable orientation and a downstream birefringent crystal in the photocathode laser beamline: changing the polarisation of the laser pulse by rotation of the half-wave plate changes the amount of intensity that is transported into the direction of the photocathode through the birefringent crystal. Charge ratio and delay between the shaped driver bunch and the Gaussian witness bunch were measured at the first screen available downstream of the TDS cavity (Fig. 10.1, PST.Scr1) and was adjusted via the laser bypass setup depicted in Fig. 7.5.
Following these preparations, the argon gas flow through the discharge plasma cell was adjusted for a stable pressure of 0.6 mbar in the cell and a voltage of 2.4 kV was applied to the capacitors of the pulse electronics. A trigger signal synchronised to the master oscillator of the accelerator was used to trigger the discharge switch. The timing at which bunch extraction from the cathode and ignition of the arc discharge in the plasma cell coincide was determined by monitoring the discharge current pulse and the signal of an integrating current transformer (ICT) at the photoelectron gun (Fig. 10.1, Low.ICT1) on an oscilloscope. A delay of zero was defined as the time when the bunch is measured at the same time with the plasma current rise above the noise level, which corresponds to $t \sim 0.5\,\mu$s in Figs. 8.14 and 8.22). The bunches' drift duration from the ICT to the plasma cell is roughly 20 ns, which is negligible with respect to the evolution of the plasma with a timescale of microseconds (see e.g. Fig. 8.22).
For every beam/plasma parameter setting, 10 consecutive measurements were recorded. Beam measurements shown below are averaged over the 10 individual measurements. No significant deviation between individual measurements was found, if not indicated differently.

10.2 Mitigation of beam-plasma instabilities

In accordance with the simulation results presented in Sec. 9.2, the first measurements after setting up initial beam parameters were to scan the plasma density during the interaction in order to achieve stable beam transport. As described in Sec. 8.4, this is done by changing the delay between electron beam arrival and arc discharge ignition in the plasma cell. Figure 10.2 shows the measured longitudinal-transverse projection of driver and witness bunches with a total charge of (677 ± 70) pC with and without plasma interaction at a main gun solenoid current of 380 A.

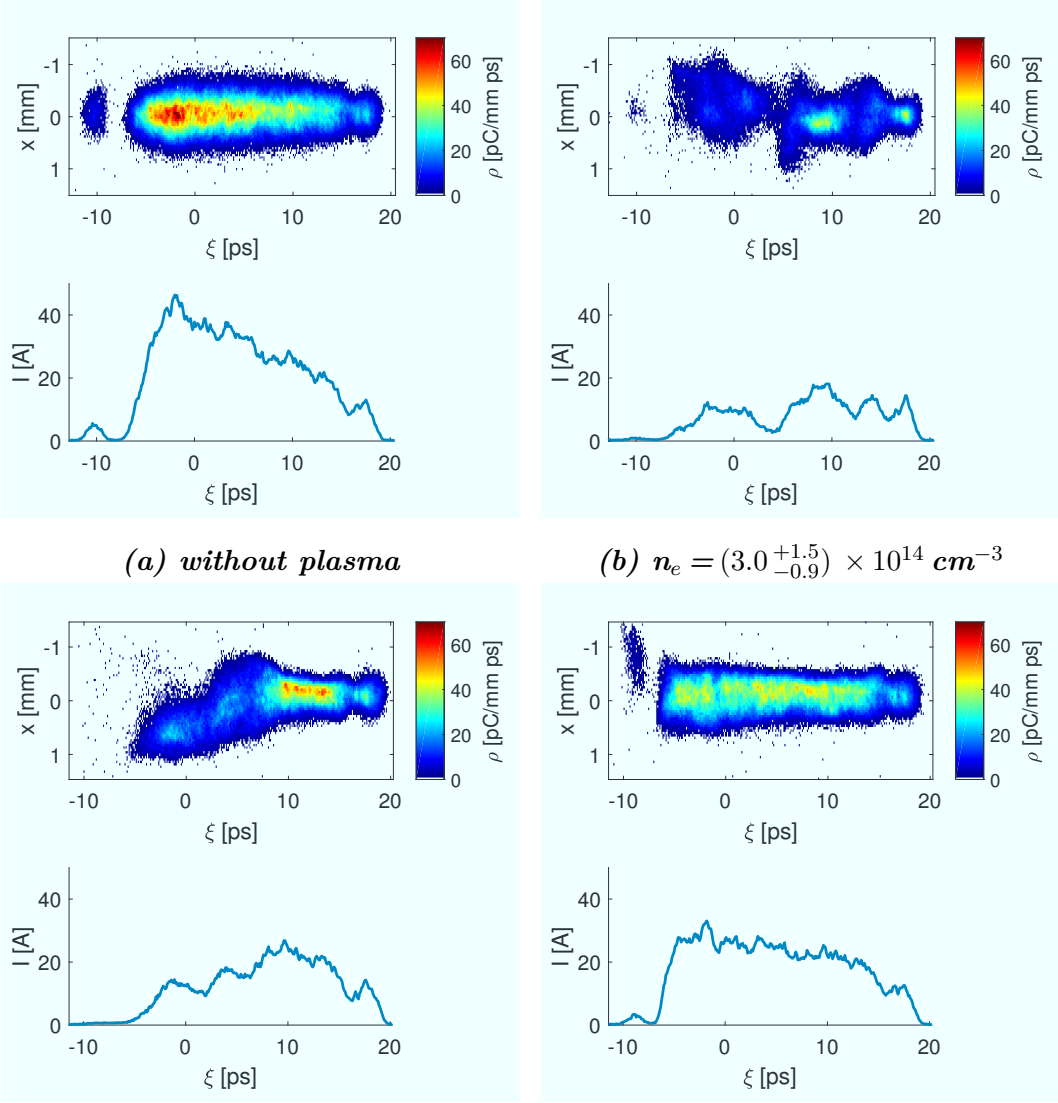

(a) without plasma ***(b)*** $n_e = (3.0\,^{+1.5}_{-0.9}) \times 10^{14}\ cm^{-3}$

(c) $n_e = (6.5\,^{+4.5}_{-2.3}) \times 10^{13}\ cm^{-3}$ ***(d)*** $n_e = (1.1\,^{+0.7}_{-0.4}) \times 10^{13}\ cm^{-3}$

Figure 10.2: Transverse-longitudinal projections of charge density ρ of a $(677 \pm 70)\,pC$ bunch without (a) and with (b-d) plasma interaction in the comoving coordinate $\xi = z - ct$. The delays of the electron bunches to the zero timing of the gas discharge are $110\,\mu s$ in (b), $190\,\mu s$ in (c) and $300\,\mu s$ in (d).

Given densities are measured with the SMI-based method introduced in Sec. 8.4. As expected from simulations, the bunch shows clear signs of self-modulation at the rather high density in Fig. 10.2 (b):

- the charge dropped significantly to less than 250 pC
- the driver bunch is split up longitudinally into small bunchlets, the periodicity of which roughly corresponds to the expected plasma oscillation period length of 7 ps.

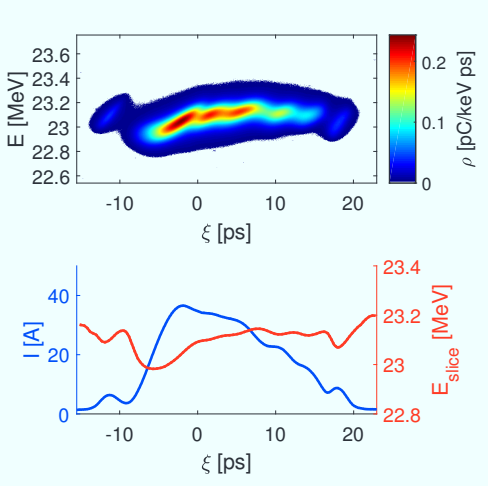

Figure 10.3: Longitudinal phase space of the (677±70) pC driver & witness beam, measured in the high energy dispersive section HEDA2 [top; no plasma interaction, compare Fig. 10.2 (a)]. Bottom plots show bunch current profile (blue) and slice energies (red).

The transverse offset of several slices (e.g. around 7 ps and -2 ps) might either have been caused by the hosing instability or by dispersion in the beamline optics after the plasma. In the wakefield interaction large differences in the slice energies may have been acquired, which could cause inhomogeneous transport. Further lowering the plasma density yielded the projections shown in Figs. 10.2 (c) and (d). While in Fig. 10.2 (c) a deflection of the tail of the driver bunch is still apparent, this is completely mitigated in Fig. 10.2 (d). Stable transport in the wakefields is therefore assumed. The deflection of the witness bunch might still be caused by asymmetric wakefields, i.e. hosing. To exclude influence of such an offset on the measured witness bunch energy changes and therefore on the measured transformer ratio, it is considered in the error calculations as detailed in the next section.

The residual charge losses at the tail of the driver bunch are attributed to large focusing forces inside of the plasma. Slices at the tail of the driver experience the highest transverse forces [see e.g. Fig. 9.9 (b)] and therefore exhibit the largest divergence upon the exit of the plasma. Simulations show that this can lead to particle losses at the plasma cell exit window flange in certain cases.
In the measurements where the instabilities are not as clearly visible in the

longitudinal projection of the bunches as in Fig. 10.2 (b), further information, e.g. on the longitudinal phase space (LPS) of the bunches, is required. Figures 10.3 and 10.4 display the longitudinal phase spaces of the beam without and with plasma interaction, respectively. The phase space of the

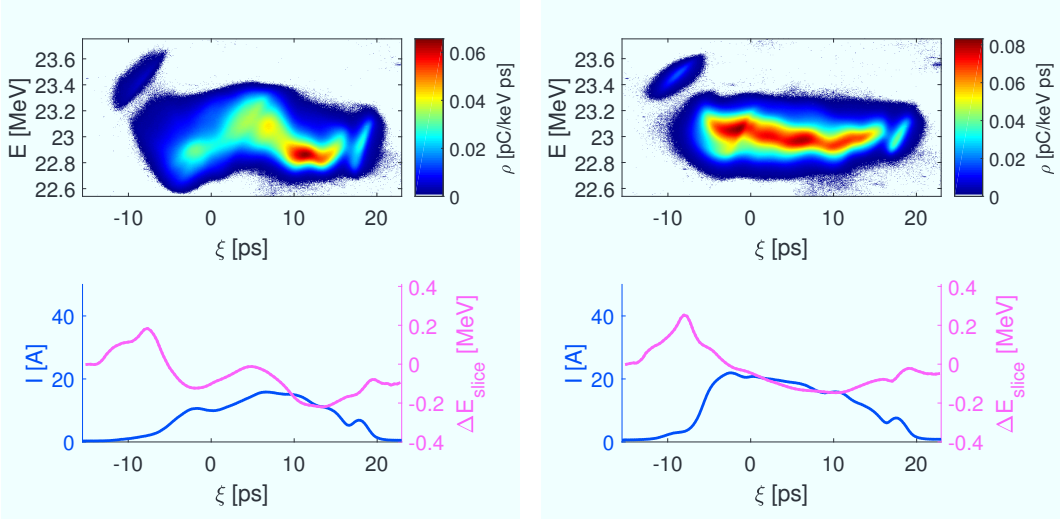

(a) $n_e = (6.5\,^{+4.5}_{-2.3}) \times 10^{13}\ cm^{-3}$ ***(b)*** $n_e = (1.1\,^{+0.7}_{-0.4}) \times 10^{13}\ cm^{-3}$

Figure 10.4: Longitudinal phase space of bunches after wakefield interaction for two different plasma densities (top). The delays of the electron bunches to the zero timing of the gas discharge are 190 μs *and* 300 μs *for cases (a) and (b), respectively [compare Fig. 10.2 (c-d)]. Bottom plots show measured bunch current profiles (blue) and slice energy changes (magenta) compared to the corresponding LPS without plasma interaction (Fig. 10.3).*

beam at higher density [Fig. 10.4 (a), corresponding to Fig. 10.2 (c)] shows an energy modulation within the driver bunch, i.e. the slice energy drops to lower values shortly after the bunch head, then rises again to higher values in the middle of the bunch and finally decreases towards the bunch tail. This is again a clear sign for the self-modulation instability, where the wakefield changes sign within the bunch (compare Figs. 8.23 and 8.24). In the case of Fig. 10.4 (b), no such modulation is apparent, which confirms that no self-modulation has occurred in this PWFA interaction. Similar results for changing plasma density are achieved for other bunch charges, with slight variations in the maximum density at which signs of instabilities disappear.

Further studies on the mitigation of the self-modulation instability were

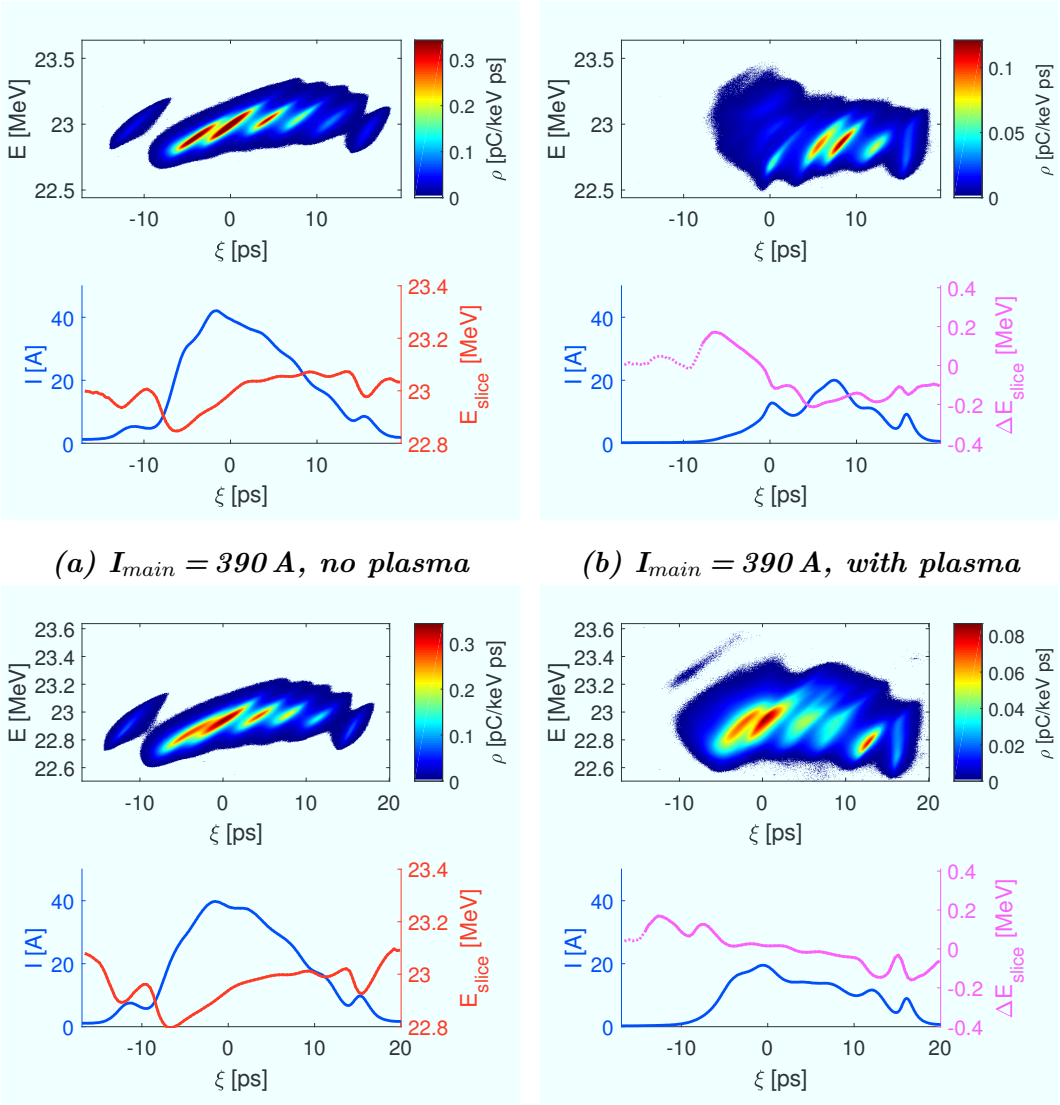

(a) $I_{main} = 390\,A$, no plasma ***(b) $I_{main} = 390\,A$, with plasma***

(c) $I_{main} = 360\,A$, no plasma ***(d) $I_{main} = 360\,A$, with plasma***

Figure 10.5: Longitudinal phase spaces of bunches (top) without (a,c) and with (b,d) plasma interaction for different gun main solenoid currents I_{main}. The bunch-discharge delay in (b) and (d) is 170 µs, which corresponds to a plasma density of $n_e = (8.5\,^{+6.3}_{-1.1}) \times 10^{13}\ cm^{-3}$. Bottom plots show bunch current profile (blue) and slice energy (a,c; red)/slice energy changes due to wakefields (b,d; magenta).

conducted with varying bunch focus at the entrance of the plasma. The longitudinal phase spaces of bunches with a gun main solenoid focusing current of 390 A are depicted in Figs. 10.5 (a,b). With a plasma present in the plasma cell [Fig. 10.5 (b)], the LPS of the driver is clearly deteriorated and large losses of beam particles from the centre to the tail of the bunch are visible in the current profile. This is again attributed to defocusing transverse wakefields and consequent loss of beam particles at the plasma cell exit aperture.
Such strong signs of the self-modulation instability are not observed at the same plasma density and a gun main solenoid current of 360 A [Figs. 10.5 (c,d)]. Here, the driver bunch current profile shows significantly lower charge losses at the bunch tail with plasma interaction. As for the case shown in Fig. 10.2 (d), these losses are attributed to strong divergence of the bunch tail due to large transverse focusing wakefields in the plasma rather than defocusing fields. Also the slice energy changes in Fig. 10.5 (d), bottom, do not exhibit the clear change of sign within the driver bunch that is observed in Fig. 10.5 (b). It is concluded that a main solenoid current of 390 A provides an over-focused bunch at the plasma entrance. Such, the bunch density is not sufficiently high at this plasma density to allow PWFA in the quasi-nonlinear regime, as needed for mitigating the self-modulation instability (see Secs. 4.1.3 and 9.2).
This experimental mitigation of beam-plasma instabilities by optimisation of the bunch parameters relative to plasma parameters (i.e. bunch length in plasma skin depths, beam density to plasma densities, etc.) via changing the plasma density and the bunch focusing, validates the predictions of numerical simulations described in Sec. 9.2. Detailed scans in the parameter range free of clear instability signatures could therefore be performed to experimentally optimise the transformer ratio of the PWFA.

10.3 High transformer ratio observation

10.3.1 Experimental error analysis

To find the maximum transformer ratio achievable with the setup described above, various parameter scans of the bunch charge, the driver-witness delay, the solenoid current, the plasma density and the driver shape were performed. Transformer ratios were calculated according to Eq. (9.2). To assess the experimental uncertainty of the measurements, several sources of errors were

taken into account:

1. The RMS slice energy spread of the driver bunch is considered as an error of the driver slice energy loss. It is included into the error of the transformer ratio to represent that some particles in a slice might be lost earlier than others and that this partial loss of a slice may already prohibit stable acceleration (i.e. reduce the amount of energy that can be extracted from the driver and transferred to a witness bunch).

2. The standard deviation of the measured driver and witness bunch energies in 10 consecutive measurements represents statistical variation of the driver and witness bunches. This is important as the transformer ratio was not measured in a single shot but driver slice loss and witness energy gain were measured separately. The contribution of this error source was found to be comparably small in all cases presented here.

3. The resolution of the dipole spectrometer, which is used for the LPS measurements, is included into the error of measured energies to account for the limited precision with which bunch energies can be determined in experiment.

4. As shown in the previous section, the witness bunches may acquire transverse offsets in the wakefield interaction compared to their positions on measurement screens without interaction. While these offsets were only observed in some cases, they may influence the energy measurement and hence the measured TR. The position of the witness was therefore measured at a screen upstream of the dipole spectrometer with and without plasma interaction, to quantify transverse offsets. In a separate experiment, the sensitivity of the dipole spectrometer to transverse and angular offsets was determined by changing position/angle of the beam using two steerer magnets upstream of the dipole, while monitoring changes in the energy measurement. The energy deviation resulting from the measured offset and spectrometer sensitivity was added to the measurement uncertainty of the witness bunch energy. For measurements in which no additional measurement of the witness bunch position had been performed, the maximum error that was measured for the spectrometer while staying within the transverse acceptance of the dipole was taken into account.

5. The transverse size of the witness bunch at the energy measurement screen is convoluted with the energy spectrum of the bunches and hence

changes the maximum energy that is measured for the witness bunch. It is therefore included into the error of the measured maximum witness bunch energy. Due to the edge focusing of the 60° HEDA2 dipole, the size of the bunches at the measurement screen is not directly accessible. Therefore, the full RMS energy spread of the witness bunch is taken as the measurement error, i.e. it is assumed that the full measured energy spread might be due to the transverse bunch size at the measurement screen.

6. To account for the fact that the witness electrons with the highest energy after plasma acceleration may not have been the highest-energetic electrons before plasma interaction, the difference between mean and maximum witness energy is added to the positive error on the measured energy gain in the PWFA.

Errors for the measured transformer ratios were calculated from the above-mentioned errors by Gaussian error propagation.
The temporal resolution in the longitudinal phase space measurements was deduced from the vertical bunch size on the measurement screen with TDS cavity switched off. The vertical bunch size is defined by the beam optics upstream of the measurement screen and has to be traded off against the horizontal bunch size, i.e. energy resolution in the dispersive section. For the used

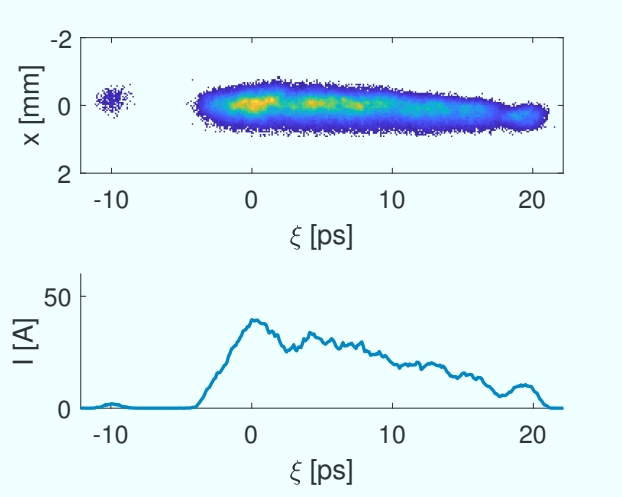

Figure 10.6: Transverse-longitudinal projection in the co-moving frame $\xi = z/c - t$ for the 518 ± 16 pC driver/witness beam that was measured to drive a PWFA with a transformer ratio of $4.6^{+2.2}_{-0.7}$.

beam optics the temporal RMS resolution was measured to be (2.0 ± 0.3) ps. The highest density at which stable HTR driver transport was predicted in simulations is $10^{14}\,\mathrm{cm}^{-3}$ (see Sec. 9.2). The temporal measurement resolution allows to well resolve the energy variations on the time scale of this highest expected density, which corresponds to a plasma wavelength of ~ 11 ps. Maximum densities at which stable acceleration was actually measured were even slightly lower.

10.3.2 First demonstration of HTR PWFA

Figure 10.6 shows the transverse-longitudinal projection of a (508 ± 10) pC double triangular driver bunch with a (10 ± 6) pC Gaussian witness bunch. These entered a plasma with an electron density of $(1.9 \pm 0.4) \times 10^{13}\,\mathrm{cm}^{-3}$. Longitudinal phase spaces of the bunches without and with plasma are depicted in Figs. 10.7 (a) and (b), respectively. Driver and witness bunch longitudinal phase spaces were measured independently on the same LYSO scintillator but using different camera gain, to allow for the best signal to noise ratio for both bunches despite their large charge difference. An energy uncertainty due to the witness position of 30 keV was determined for this measurement. The maximum energy loss of the driver slices [max. difference between white dashed lines in Figs. 10.7 (a) and (b)] was measured to be

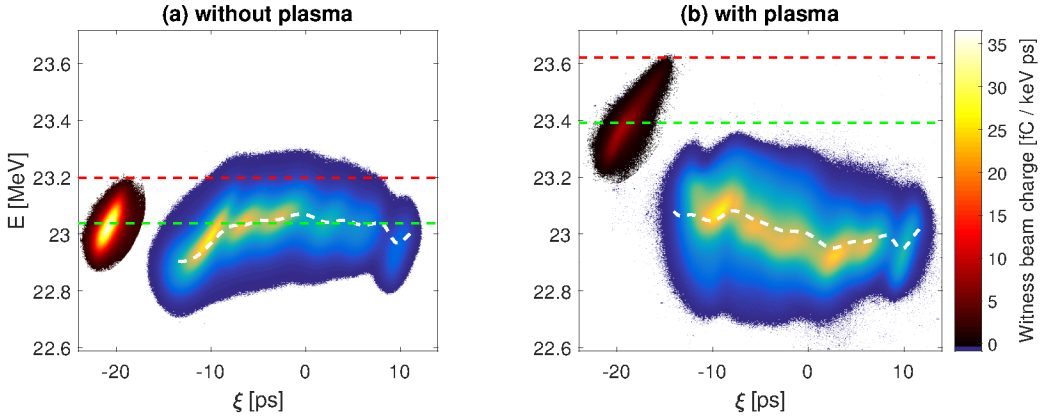

Figure 10.7: Longitudinal phase spaces of driver and witness bunches measured without (a) and with (b) a plasma of $(1.9 \pm 0.4) \times 10^{13}\,cm^{-3}$ *electron density. The witness bunch (at* $\xi \approx$ *-20 ps) was measured with a different camera gain than the driver. Dashed lines indicate witness mean (green) and maximum (red) energies and the driver mean slice energies (white).*

(0.09 ± 0.01) MeV. For the witness bunch, the highest energy was defined experimentally as the energy at which the signal of the witness bunch exceeds five standard deviations of the measurement noise above the mean noise level. The increase of the maximum energy was measured to be $(0.43^{+0.19}_{-0.02})$ MeV, the increase of its mean energy (0.36 ± 0.01) MeV [energy change for the red and green dashed lines between Figs. 10.7 (a) and (b), respectively]. The former corresponds to an effective transformer ratio of $R_{eff} = 4.6^{+2.2}_{-0.7}$, which is the first and only reported high transformer ratio measured in a plasma wakefield accelerator to date [215].
Calculating the transformer ratio for the change of the mean energy of the witness yields $R_{eff,\,mean} = 3.9 \pm 0.7$. By comparing the total light yields on the LYSO scintillator screen with and without plasma interaction, a charge loss of the witness bunch of 66 % was measured, which is discussed below.
No signs of instabilities were found in the measurements even though calculation reveals that $\sim$ 13 growth lengths of the self-modulation instability and $\sim$ 10 of the hosing instability have been traveled by the driver bunch (according to formulas given in Ref. [114]). Instabilities have therefore been successfully mitigated by operation in the nonlinear regime.

10.3.3 Numerical simulation of measurements

To validate that the measured transformer ratios can be reproduced from wakefield theory, numerical simulations were performed with ASTRA and HiPACE. First the longitudinal bunch profile was iterated until the bunch shape at the plasma entrance corresponded to the profile measured in experiment (see Figs. 10.6 and 10.8). Subsequently, the gun main solenoid current, the plasma density and also the increase of the bunch divergence due to the foil windows were varied within the uncertainty of the measurements. For all simulated cases, the energy loss and gain and the corresponding transformer ratio was monitored. Reasonable agreement with the measured values was found at a plasma density of $2.2 \times 10^{13}\,\mathrm{cm}^{-3}$, a mean foil scattering angle of 0.2 mrad, and a plasma length of 64 mm. Plasma density and foil scattering are well within the expected parameter range. The shorter interaction length compared to the electrode distance of 100 mm is attributed to the loss of ionised gas through the beam apertures of the electrodes as detailed in Sec. 8.4. The simulated transformer ratio for these parameters (for the gain in maximum witness bunch energy) is $R_{eff} = 4.3$.

Figure 10.9 shows the bunch and plasma density, and the wakefield distributions at beginning ($z = 0$ mm) and end ($z = 64$ mm) of the simulated

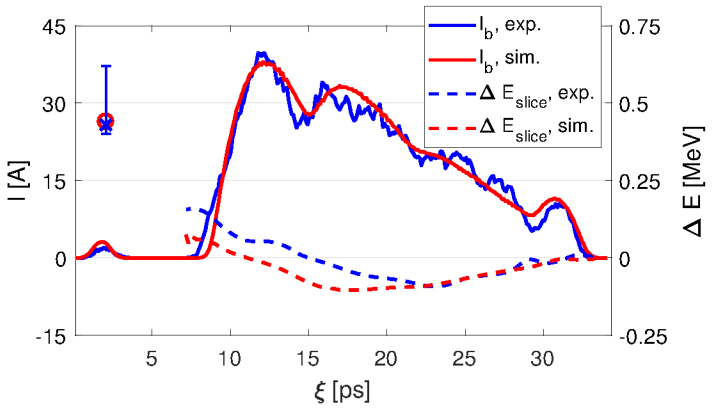

Figure 10.8: Experimental and simulated electron bunch currents I_b (solid lines) and slice energy changes ΔE_{slice} (dashed lines) between plasma off and on cases in the comoving coordinate $\xi = z/c - t$. Blue cross and red circle indicate measured and simulated maximum witness energy gain, respectively.

interaction. The majority of witness bunch electrons (around $\xi \approx 3\,\mathrm{ps}$) is outside of the plasma bubble at the beginning of the interaction [Fig. 10.9 (a)] where they are defocused by strong transverse wakefields until the end of the interaction. Only $\sim 30\,\%$ are trapped on axis within the plasma bubble and accelerated [Fig. 10.9 (b), bottom, red dots close to axis at $\xi \approx 3\,\mathrm{ps}$; large charge difference between witness and driver bunches gives uniform colour of witness charge density]. The number agrees well with the witness particle loss that was measured in experiment. Defocusing and consequent collision with downstream beamline apertures is therefore assumed to be the reason for the witness charge loss, whereas simulations did not allow to reconstruct the exact LPS of the witness bunch. This may be due to known discrepancies between simulated and experimental bunch Twiss-parameters and correspondingly different bunch transport.
The wakefields and slice energy loss along the driver bunch, which are shown in Figs. 10.9 (a,b), and Fig. 10.8, respectively, are not homogeneous, as predicted for achieving the highest transformer ratios (see Sec. 3.2). This might be due to improper matching of the bunch shape to the plasma density. The precursor of the double triangle should e.g. be a quarter plasma wavelength long (see Sec. 3.2). Otherwise the wakefield amplitude varies along the driver bunch, as in Fig. 3.2 (a). Furthermore, the one-dimensional calculations for optimal longitudinal bunch shapes in Sec. 3.2 do only apply to homogeneously focused bunches and are assuming linear interaction. The interaction in the

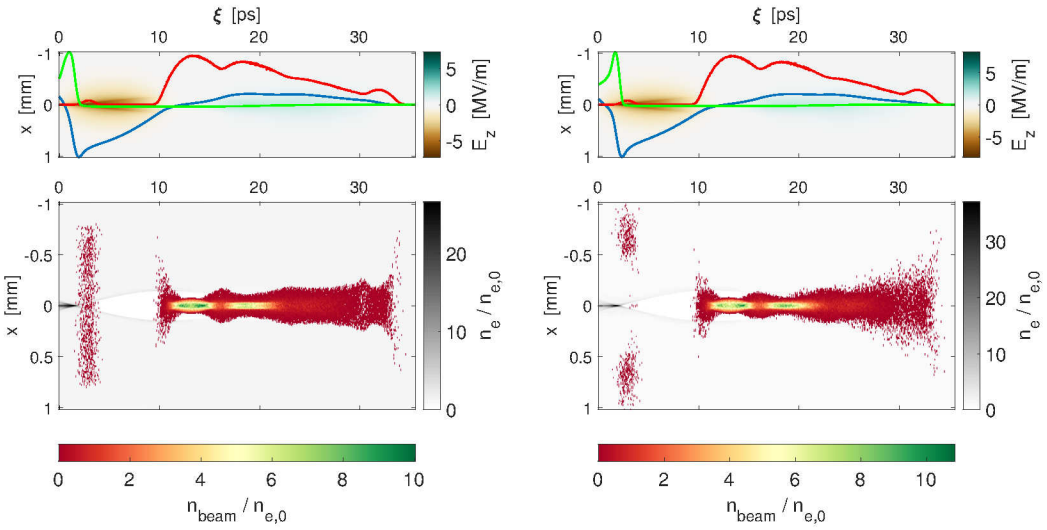

(a) $z = 0\,mm$ **(b) $z = 64\,mm$**

Figure 10.9: Simulation results for the experimentally demonstrated HTR PWFA at a plasma density of $2.2 \times 10^{13}\,cm^{-3}$ *in the co-moving frame* ($\xi = z/c - t$) *at the entrance (a) and at the end (b) of the plasma. Top plots show the longitudinal electric field distribution in the* x-ξ*-plane close to the axis, bunch current profiles (red line), longitudinal fields (blue line, shares axis of colourbar) and transverse fields (green line, in arbitrary units) on axis. The lower plots show beam (red-yellow-green colour scale) and plasma (grey colour scale) electron densities in the* x-ξ*-plane close to the axis.*

present case is clearly nonlinear, though, with bunch densities exceeding the plasma electron densities by an order of magnitude and a wakefield bubble completely void of plasma electrons [see Figs. 10.9 (a,b), bottom].
Overall, simulations allowed to rather accurately reproduce the measured values with input parameters well within the bounds of experimental uncertainties. This affirms the experimental findings as well as the validity of the numerical models applied in simulations.

10.4 Maximum transformer ratio and energy extraction

As stated in the beginning of the previous section, various measurements of HTRs have been recorded. In the following, two further measurements will

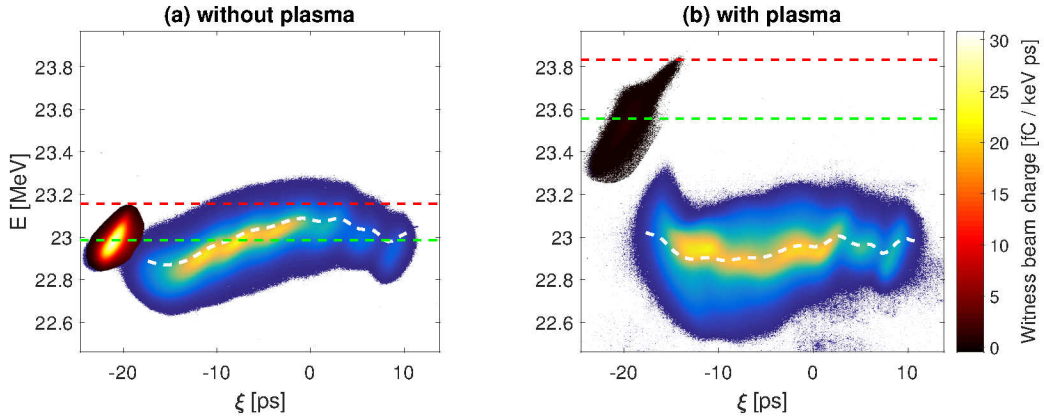

Figure 10.10: Longitudinal phase spaces of driver and witness bunches measured without (a) and with (b) a plasma of $(1.2 \pm 0.4) \times 10^{13}\, cm^{-3}$ *electron density. The witness bunch* ($\xi \approx -20\, ps$) *was measured with a different camera gain than the driver. Dashed lines indicate witness mean (green) and maximum (red) energies and the driver mean slice energies (white).*

be addressed in detail, which show the highest measured TR and the most homogeneous driver energy extraction. Other measurement results, which are of interest but not directly related to the scope of demonstrating high transformer ratio PWFA, are discussed in Appendix D.

Highest recorded transformer ratio

Various other measurements that were conducted also yielded transformer ratios well above 2. Few of these measurements also showed higher values than the one reported in the previous section. Figure 10.10 shows the longitudinal phase space of a driver and witness beam, that was calculated to drive and experience, respectively, a wakefield with $R_{eff} = 5.0^{+1.5}_{-0.4}$. The plasma density in this measurement was $(1.2 \pm 0.4) \times 10^{13}\,\mathrm{cm}^{-3}$, the charge of driver and witness bunches (700 ± 19) pC and (29 ± 1) pC, respectively.
Even though this measurement shows the highest recorded TR, the measurement of the witness bunch LPS was subject to larger statistical fluctuation than the measurement shown in the previous section. The LPS measurement with a charge density colourmap scaled to the maximum witness density measured with plasma is shown in Fig. 10.11. While the LPS of the driver beam was rather stable throughout the measurements, the witness bunch high energy tail does not reach to the highest measured energy in every of the 10

recorded phase space measurements (a detailed depiction of similar fluctuations is shown in App. D). Furthermore, only 4 % of the witness bunch charge was transported to the LPS measurement screen when the bunch interacted with the plasma.
No reconstruction of the measurement via simulations is available thus far, neither. Simulations that have been conducted did not reproduce the measured TR value, whereas due to the sensitivity of the simulated TR on the input parameters and the large parameter space this does not exclude the possibility of numerical reconstruction. Nevertheless, these findings do not affect the measured transformer ratio.
No clear reason for the higher transformer ratio compared to the case described in the previous section could be identified. As stated above, simulations show very sensitive dependence of the TR on the input bunch parameters. One indication is a higher uniformity of the wakefields within the driver bunch as discussed below.

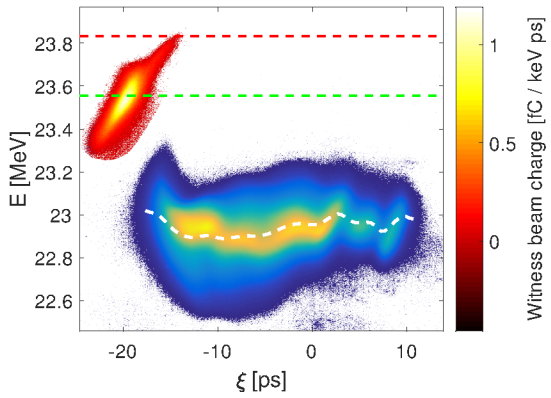

Figure 10.11: LPS measurement of the beam that showed a transformer ratio of $5.0^{+1.5}_{-0.4}$ *with witness charge density colourmap scaled to the maximum measured witness intensity after plasma wakefield interaction [compare Fig. 10.10 (b)].*

Homogeneous driver bunch energy extraction

As detailed in Sec. 3.2, the maximum TR should be achieved when the deceleration of the driver bunch is homogeneous. This is also the condition for maximum energy extraction from the driver bunch, i.e. for enabling high efficiency acceleration (see also Sec. 3.3).
The maximum deviation from the mean deceleration along the driver bunch

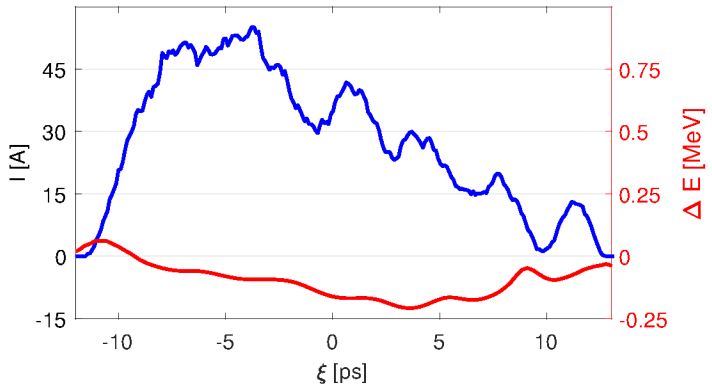

Figure 10.12: Driver bunch current profile and energy change of the mean slice energy ΔE in the co-moving frame $\xi = z/c - t$ for a bunch of $(685 \pm 15)\,pC$, which showed the most homogeneous deceleration by plasma wakefields at a plasma density of $(3.1^{+1.1}_{-0.3}) \times 10^{13}\ cm^{-3}$.

was evaluated in the conducted measurements, to validate this correlation between TR and the flatness of deceleration in the driver bunch. The deceleration in the driver varies within the precursor even in ideal cases (see Fig. 3.2). Therefore the wakefields at the driver bunch head (in the precursor) are not taken into account. The wakefield behind the current maximum of the driver bunch shall rise quickly to high gradients and therefore a high deviation is often found in these tail slices. In an ideal bunch shape, the current sharply drops to zero after the current maximum. Hence, the deceleration in the driver bunch tail behind the current maximum is not considered for calculating the homogeneity of deceleration, neither. The maximum deviation is here defined as the maximum difference between slice mean energy change to the average slice mean energy change. To account for the fact that all slices are equally important to retain stable acceleration, slice energies are not weighted by the slice charge.
Analysis reveals that the measurements reported above, which were found to exhibit the highest TRs, do not show the most homogeneous deceleration along the driver bunches. In case of the measurement that yielded $R_{eff} = 4.6^{+2.2}_{-0.7}$, which is examined in Sec. 10.3, the maximum absolute deviation of 0.11 MeV corresponds to more than 100 % relative deviation from the mean deceleration (~ 0.03 MeV). The high relative numbers are caused by the fact that part of the driver bunch is even accelerated, which causes the mean deceleration to approach low absolute values. For the measure-

ment that yielded the highest TR of $R_{eff} = 5.0^{+1.5}_{-0.4}$ (see previous passage), a maximum deviation of 0.07 MeV, corresponding to 73 % of the mean deceleration of 0.10 MeV, was calculated. The reduced deviation compared to the $R_{eff} = 4.6^{+2.2}_{-0.7}$ case is also evident from the lower acceleration in the driver bunch tail in Fig. 10.10 compared to Fig. 10.7.
A minimum value of 62 % for the maximum relative deviation (0.09 MeV over 0.13 MeV) was found at a plasma density of $(3.1^{+1.1}_{-0.3}) \times 10^{13}\,\mathrm{cm}^{-3}$ and gun main solenoid current of 380 A for a (685±15) pC driver bunch with the bunch current profile shown in Fig. 10.12. The measurement was recorded during scanning the focusing of the beam into the plasma, i.e. the gun solenoid current. The main difference to the measurements described above is therefore assumed to be the transverse profile of the bunch when entering the plasma. As the witness bunch signal was not detectable over the noise level at these parameters, no transformer ratio is available for this measurement. The loss of all witness bunch particles is attributed to an unfavourable driver-witness bunch delay. No additional measurements with different bunch delay could be performed due to increased permeation of gas from the plasma cell through the electron beam foil windows (see also Sec. 8.2). Measurements with the same bunch parameters and slightly higher and lower plasma densities (±30 %), which showed comparable slice energy change homogeneity, yielded TRs between 1 and 3.
The fact that no direct correlation between measurements of most homogeneous driver deceleration and highest TRs was found (i.e. that the most homogeneous energy extraction does not seem to have provided the highest TR) is partially attributed to improper driver-witness bunch timing and beamloading of the driver wakefield by electrons in the driver bunch tail. In the former case, the TR might be high, but due to the witness bunch not probing the wakefield phases of maximum acceleration, the measurement does not reveal the actual TR. In the latter case, the beam optics of the driver bunch might lead to tail electrons behind the current maximum of the driver being focused such, that their wakefields reduce the wakefield amplitude at the witness position. This effect is described in Sec. 3.2 and Ref. [69]. Improvement of bunch shaping flexibility and accuracy would therefore allow to increase the TR for driver bunches with homogeneous deceleration and thus also enable reaching highest efficiency in PWFA.

Part III

Summary, Conclusion and Outlook

The field of electron acceleration in plasma wakes driven by high brightness particle beams has made significant progress in the last decade and has become one of the prime candidates for future compact electron accelerator technologies. Ever higher gradients were reported from experiments at the Stanford Linear Accelerator Center (SLAC), culminating in the demonstration of 52 GV/m accelerating fields for an acceleration length of 85 cm. Besides these energy records, efficiency and stability were main targets for experimental efforts in the field in recent years.
Future experiments will further push into this direction and for beam quality preservation, to investigate the capability of PWFA to deliver electron beams for user applications. These experiments will also include the extraction of the maximum amount of energy from the driver bunches, to maximise first the energy gain of the witness electrons and second the amount of energy that is transferred to the whole witness bunch. For the former, the ratio between deceleration of the driver and acceleration of the witness (i.e. transformer ratio) plays a crucial role, as it defines the maximum achievable energy gain of witness particles for a given driver particle energy. For the latter, the energy transfer from the driver to the wake has to be maximised, which requires homogeneous energy extraction from the driver bunch. Only then, the acceleration is not deteriorated by loss of driver particles before the maximum energy is extracted from all of them. This homogeneity is achieved when the transformer ratio of the driver's wakefield is maximised. The transformer ratio is therefore a crucial parameter for the optimisation of PWFA. Nevertheless, despite much theoretical and numerical investigations since the proposal of PWFA, thus far no experiment had reported a TR exceeding the linear limit of 2.

In the course of the present work, an experiment was planned, implemented and successfully conducted to demonstrate the driving of plasma wakefields with a transformer ratio significantly surpassing this limit.
High transformer ratio schemes were investigated with numerical simulations on their applicability to the PITZ accelerator at DESY. Single, shaped driver bunches with triangular current profiles were found to drive HTR PWFA at the parameters achievable at PITZ. The existing bunch shaping capabilities of the facility, which are based on the shaping of the photocathode laser pulses, were extended to the production of bunches with the necessary parameters. After the successful generation of such driver bunches and the addition of a low charge, Gaussian witness bunch to the PITZ beam, the prospects of

the bunch shaping method by new laser pulse forming techniques based on spatial light modulators (SLMs) were investigated numerically.
An argon discharge plasma cell, providing the PWFA medium, was conceived, designed and built. Timing jitter problems in the initial design were investigated and mitigated. A novel method to determine low plasma densities ($\ll 10^{15}\,\mathrm{cm}^{-3}$), based on the self-modulation of long electron bunches in the plasma, was proposed, investigated in numerical simulations and applied to the argon discharge cell. In the available density range, results were validated by established spectroscopic density measurements.
The PITZ electron beam diagnostics were extended by LYSO scintillators, which allow to measure bunch charges below 1 pC, to ensure that accelerated bunches can be measured even after experiencing large charge losses in the PWFA.
Following the numerical confirmation, that HTR PWFA could be measured with the available diagnostics at PITZ, experiments were conducted, which yielded the first observation of high transformer ratios in a plasma wakefield accelerator. A measured TR of $4.6^{+2.2}_{-0.7}$ was also reproduced by numerical simulations at the measurement parameters. Ratios of up to $5.0^{+1.5}_{-0.4}$ were measured but could not yet be reconstructed in simulations.

Experimental methods that were developed in the course of this work may find application in further experiments. Photocathode laser based shaping of flexible bunch profiles might be applied at high energy accelerators to provide high transformer ratio drivers or customised witness bunches for the optimisation of wakefield beamloading, just to name few of the possible applications. Further optimisation of the photocathode laser based bunch shaping is ongoing at the PITZ facility and first results of the SLM-based shaping setup are expected soon. Simulations and experiments will have to reveal, whether custom bunches can be provided to applications using this technique despite possibly detrimental influence of nonlinear effects during beam transport from cathode to the point of application (e.g. by longitudinal compression of the bunches upstream of the plasma entrance for a PWFA).
Gas discharge cells like the one developed in the present work may be used in any PWFA operating at moderate densities ($\lesssim 10^{16}\,\mathrm{cm}^{-3}$) with single stage lengths of up to several meters. For the second phase of the AWAKE experiment at CERN [216] argon gas discharges with electrode distances of 5 m are e.g. being developed. The achievement of stable operation in the 10 cm long PITZ discharge cell, that was also confirmed by stable interaction of

the PITZ electron beam with the produced plasmas, is a first step towards stable operation in much longer prototypes. Further experiments at PITZ are proposed to investigate the coupling of two stages without intermediate beam optics. Two discharge cells, which share one of their electrodes, might provide negligible inter-plasma beam drift distance. This would allow to preserve beam quality over long acceleration distances where multiple plasma cells have to be used, as the length of one cell is limited by the voltage necessary to ionise the gas between the electrodes.
Furthermore, the plasma density measurement based on the self-modulation instability may be applied at any facility where the necessary longitudinal phase space diagnostics (typically a combination of a transverse deflecting cavity and a dipole spectrometer downstream of the PWFA)are available. Various facilities are planned to comprise such capabilities (e.g. FLASHForward [217], SINBAD [218]) and might therefore apply this method to validate density measurements of their plasmas or to monitor the density during measurements.
In the numerically reproduced high transformer ratio measurement, the driver bunch traveled ~ 13 growth length of the self-modulation and ~ 10 growth lengths of the hosing instability [114]. These instabilities were predicted by theory to occur in HTR-capable bunches and to inhibit acceleration over relevant distances in the plasma. The measurement of high transformer ratios therefore demonstrates that these beam-plasma instabilities can indeed be overcome by theoretically proposed means, which can similarly be applied to future PWFA experiments. In the case of the self-modulation instability, mitigation is achieved by operation in the nonlinear regime of PWFA. The absence of the hosing instability is attributed to the decoherence of slice betatron oscillations due to correlated and uncorrelated energy spreads in the driver bunch.
Finally, a transformer ratio of 4.6, as it was observed in this work, would allow the acceleration of witness particles by ~ 2.3 times higher energy as compared to the acceleration at the transformer ratio linear limit of 2. Alternatively it would allow a reduction of the driver bunch energy — and hence of the length of the driver beam accelerator — by the same factor, which may reduce size and cost of a PWFA facility significantly.

Part IV

Appendix

Appendix A

Time resolved discharge monitoring

Using the PCO DiCam Intensified CCD camera, which was also used for spectral analysis of plasma emission lines, a series of pictures with an integration time of 240 ns and step-wise increase of the delay between discharge ignition and camera gate was taken. Measurements were conducted with the first prototype of the cell, i.e. with electrodes made of stainless steel and slightly different design than the cell used for the successful HTR PWFA measurements. This setup was also operated with a preliminary version of the discharge electronics, which provided current pulses with different parameters than the ones of the optimised, final electronics presented in Ch. 8. The temporal evolution of the plasma is therefore not necessarily the same as for the final setup. Nevertheless, some observed characteristics of the discharge may be of interest for further development of plasma cells of this type or should be kept in mind when operating such cells.
The plasma cell was filled with pure argon at a pressure of 0.4 mbar and the initial capacitor voltage was 1.4 kV. Figure A.1 shows the current pulse through the plasma, that was recorded for these settings. A picture of the full plasma cell, taken with the ICCD camera, is depicted in Fig. A.2. The red rectangle marks the cutout of the discharge vessel in the centre of the cell, that is shown in Fig. A.3. Here, the same cutout is shown at different discharge/camera gate delays. The delay times refer to the time scale shown in Fig. A.1. Discharge evolution is shown up to a delay between discharge trigger and camera exposure of 4.5 μs. At higher delays the intensity of the light emitted from the plasma decreases quickly. During the build-up phase of the discharge ($t = 0.5\,\mu\text{s} - 2.5\,\mu\text{s}$) the light emission from the plasma is

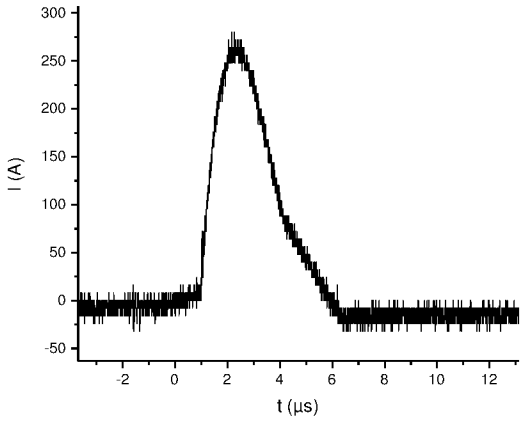

Figure A.1: Current pulse through the plasma cell for the optical discharge investigation using the preliminary discharge electronics. Zero timing corresponds to the camera gate starting point.

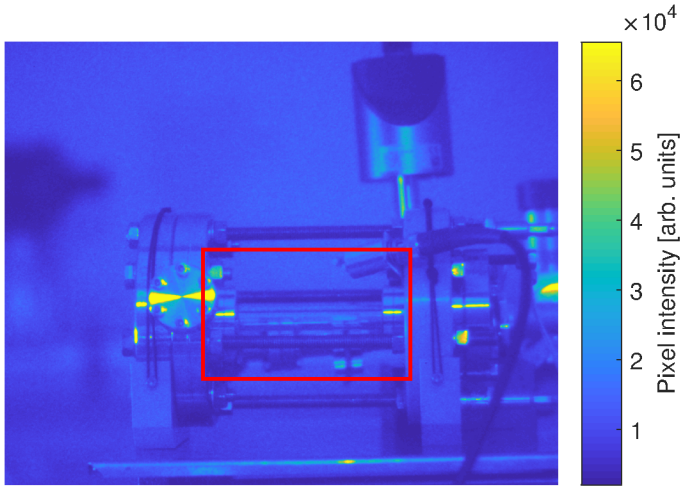

Figure A.2: Full picture of the discharge plasma cell with the discharge vessel cutout framed in red.

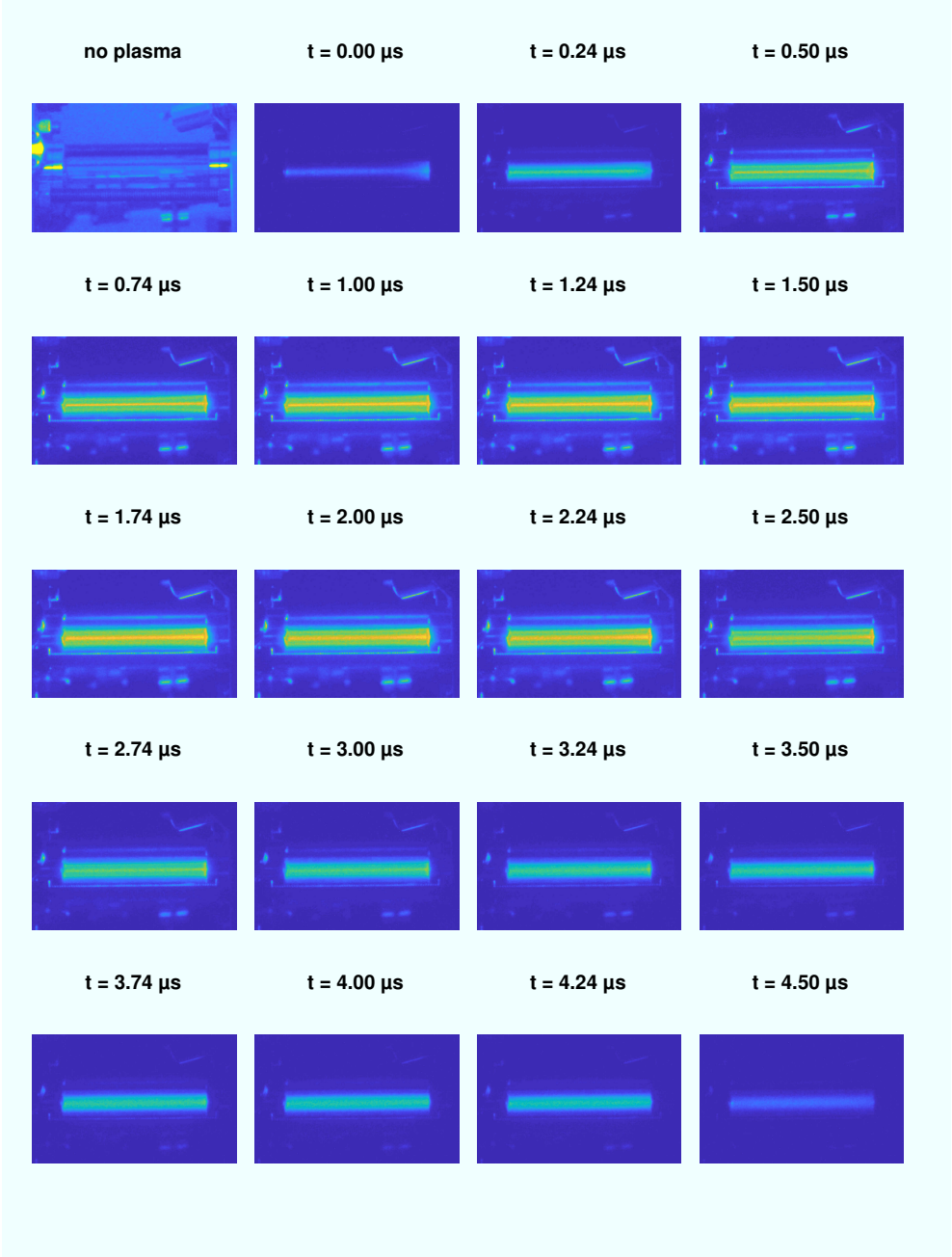

Figure A.3: Pictures of the discharge plasma in the initial setup of the PITZ gas discharge plasma cell at constant discharge parameters and varying delay between camera gate and discharge ignition. The pictures share the colour bar of Fig. A.2, whereas integration times of the pictures without plasma were $1\,ms$ *and* $240\,ns$ *with plasma.*

much brighter in the vertical middle of the discharge vessel than at the sides (Fig. A.3). This is partially due to the fact that in the vertical centre, the observer looks through a longer distance of plasma. In an optically thin medium, i.e. negligible light absorption within the plasma, the integrated light intensity is highest at this position. Nevertheless, the intensity difference between vertical centre and in the periphery is significantly smaller in later stages of the current pulse. Here the light emission seems to be rather equally distributed across the transverse cross-section of the plasma. The confined light emission in the beginning of the discharge is assumed to result from higher plasma temperatures in the transverse centre of the discharge vessel. This temperature difference might be caused by a self-confinement of the current to the centre by its own azimuthal magnetic field. This effect is also known as "pinch-effect" and is well known in discharge plasma physics [48].

To investigate this confinement further, pictures of the plasma were taken with a constant delay of $1\,\mu$s but with varying discharge voltage. The results are shown in Fig. A.4. Higher discharge voltages also correspond to higher maximum discharge currents. Confinement of the light emission to the transverse centre of the discharge seems to be less pronounced at higher voltages, i.e. currents. The higher currents result in even higher plasma temperatures. Correspondingly, the pressure of the plasma is higher, which counteracts the transverse pinching of the discharge due to the magnetic field of the discharge current. This might be more pronounced at higher discharge voltages and thus lead to the reduced light emission inhomogeneity in Fig. A.4.

Due to the rather large delays to the discharge ignition, at which HTR PWFA was measured in the present work ($\geq 200\,\mu$s), no negative effect on the HTR measurements by the transverse plasma density inhomogeneities, which may exist in the beginning of the discharge, is expected. At large delays the plasma density is assumed to have equalised transversely due to diffusion of ionised particles into regions of lower density (see also transverse homogeneity in Fig. A.3, $t \geq 4\,\mu$s). Nevertheless the effect may have to be considered for experiments conducted with lower delays between discharge ignition and beam arrival, i.e. at higher plasma densities.

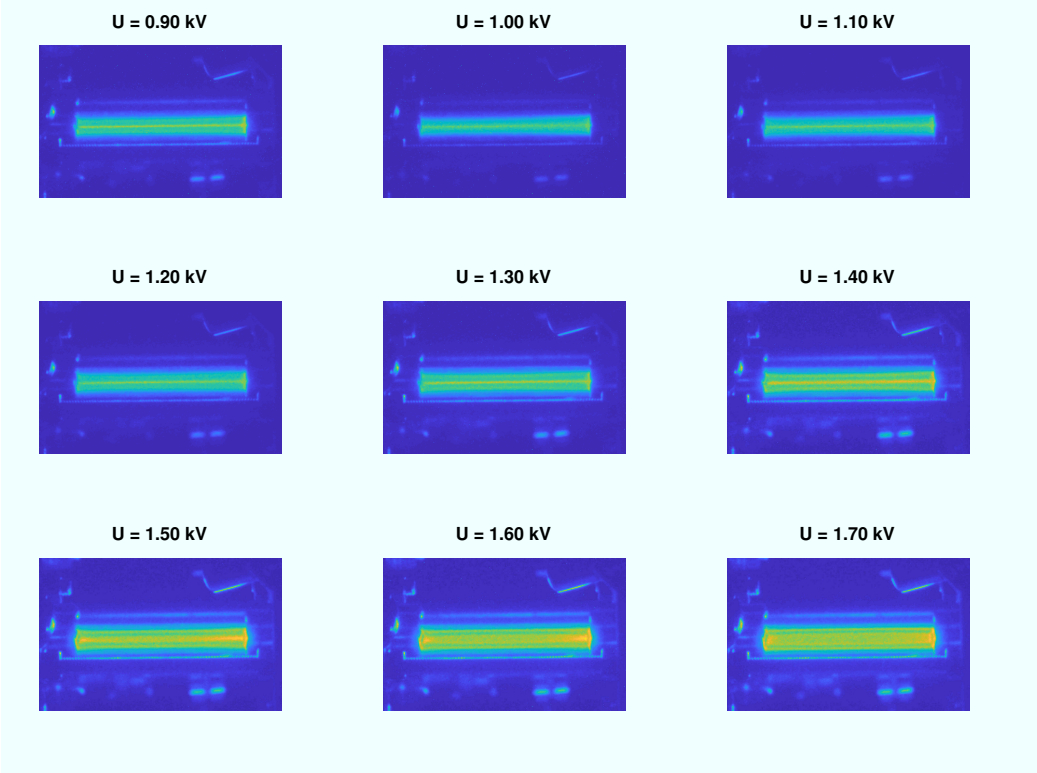

Figure A.4: Pictures of the discharge taken at $0.4\,mbar$ *and* $t = 1\,\mu s$ *with varying initial capacitor voltage. The pictures share the colour bar of Fig. A.2 and camera integration time was* $240\,ns$.

Appendix B

Density measurement accuracy simulations

The light acceptance of the fiber that was used for plasma density measurements (as detailed in Sec. 8.4) was simulated using the ray tracing function of Zemax. Figure B.1 shows a simulation of the rays that fit into the numerical aperture of the used fiber. Due to the curvature of the glass the ray traces change for different vertical positions of the fiber entrance with respect to the glass. The distance between the vertical position of the vertical fibre centre and the maximum and minimum vertical position of rays in the horizontal centre of the discharge vessel (right edge in Fig. B.1), that are within the acceptance of the fibre, are assumed to represent the position uncertainty of the plasma density measurement. Thus, the errors do not represent an uncertainty in the positioning of the fiber (which is negligible) but rather describe the area from which light and therefore information about the local plasma density is integrated. An exemplary vertical density profile measurement including these simulated errors is shown in Fig. B.2. Nevertheless, the errors do not include the fact that the local brightness of the plasma varies and that the outermost positions, from which light can be transported through the fiber, are farther away from the fiber entrance. As light intensity drops with $\frac{1}{r^2}$, with r being the distance between fiber entrance and point of light emission, areas closer to the fiber contribute more to the measured density at a certain fiber position. Similar simulations for the longitudinal measurement uncertainty are included in Fig. 8.21.

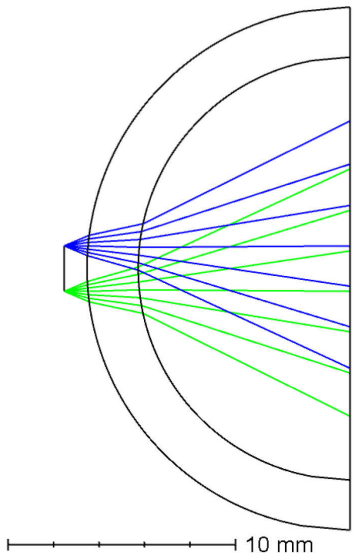

Figure B.1: Ray tracing simulation of the vertical acceptance of the fiber used for plasma density measurements. The black circles indicate the inner and outer surface of the glass discharge vessel. Blue and green are the rays that are transported through the fiber at the upper and lower edge, respectively.

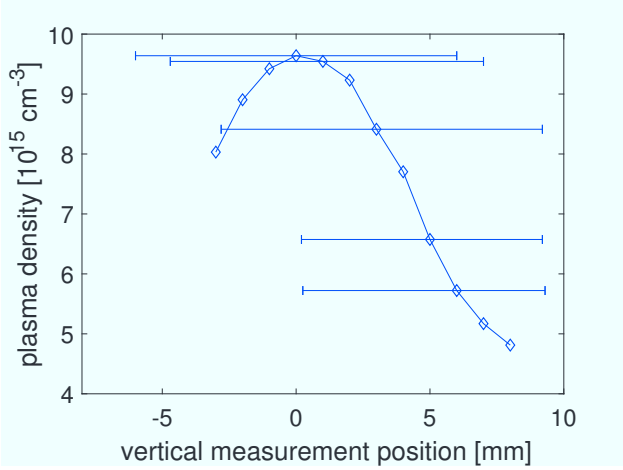

Figure B.2: Vertical density measurement at $20\,\mu$s *delay in* $2\,$mbar *argon with simulated position uncertainties.*

Appendix C

Detailed plasma density profile measurements

Additional measurements of the plasma density in the PITZ gas discharge plasma were performed to acquire a full time resolved density profile. Figure C.1 shows a longitudinal density profile in 0.6 mbar argon (98 % Ar, 2 % H_2) with a capacitor charging voltage of 2.4 kV, immediately after the end of the discharge current pulse. A slight increase in the density is visible from cathode [(-51±2) mm] to anode [(+51±2) mm]. This is attributed to the fact that electrons are expelled from the cathode region by the negative potential and attracted to the anode by the positive potential. The slope is hardly visible 20 μs after the end of the discharge current pulse (see Fig. 8.21), which is attributed either to the density measurement resolution or also to diffusion of charge particles to regions of lower density.

To validate whether the sharp drops in the density at the ends of the measurement range in Fig. 8.21 are caused by diffusion of ionised particles at the ends of the plasma column, this was analytically modeled. The plasma electrons are assumed to follow the diffusion of the slower plasma ions due to the attraction by their space charge. Diffusion is described by [48]

$$\frac{\partial n_e}{\partial t} = D\nabla^2 n_e \ , \tag{C.1}$$

where D is the ion diffusion parameter

$$D = 2k_B T/mv \ , \tag{C.2}$$

with the ion mass m, temperature T and velocity v. Assuming that the system is symmetric in transverse direction, Eq. (C.1) can be solved using a

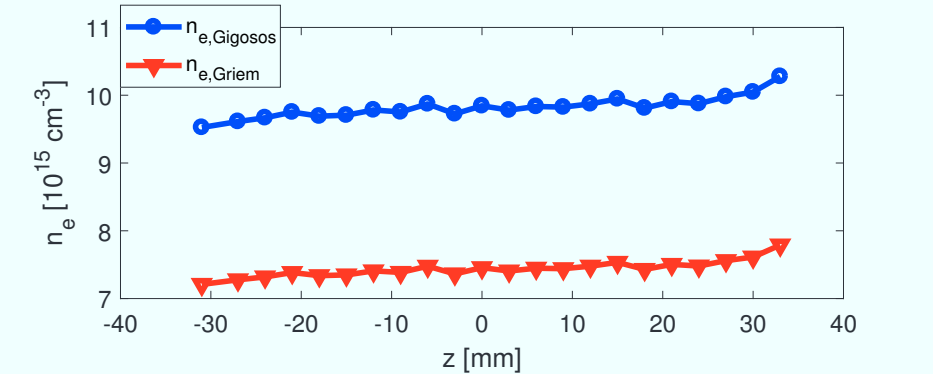

Figure C.1: Longitudinal density scan with 3 µs delay between discharge ignition and camera gate.

Fourier series and exponential time decay [48]

$$n_e(z,t) = \sum_{n=0}^{\infty} e^{-\frac{t}{\tau_n}} a_n cos(k_n z) \ , \tag{C.3}$$

where for a normalised, initially flat density profile

$$k_n = \frac{(2n+1)\pi}{L} \ , \tag{C.4}$$

$$a_n = \frac{1}{L} \int_{-\frac{L}{2}-\Delta d}^{+\frac{L}{2}+\Delta d} cos\left(\frac{(2n+1)\pi z}{L}\right) dz \ , \tag{C.5}$$

$$\tau_n = \frac{1}{D k_n^2} \ , \tag{C.6}$$

with L the plasma length and Δd the distance outside the plasma in which diffusion is considered. Figure C.2 shows a calculated, initially homogeneous longitudinal profile after 20 µs of diffusion time. As diffusion only leads to a drop in density in a few mm range on this short timescale, the major reason for the reduced relative density at the plasma edges shown in Fig. 8.21 is assumed to be loss of ionised particles due to expansion of the high pressure plasma into the ambient gas.
Another characteristic of the discharge density distribution is shown in Fig. C.3. Vertical density profiles were recorded directly after the termination of the discharge current pulse at the closest positions to the electrode surfaces. A central drop in the density profile is observed at both ends of the discharge. This is presumably caused by a funnel-like current density

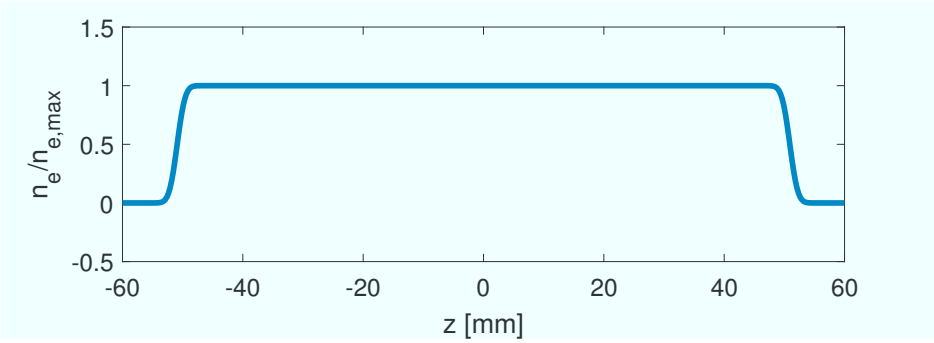

Figure C.2: Calculated normalised longitudinal density profile of an initially 100 mm, homogeneous plasma column at 0.6 mbar *after* 20 μs.

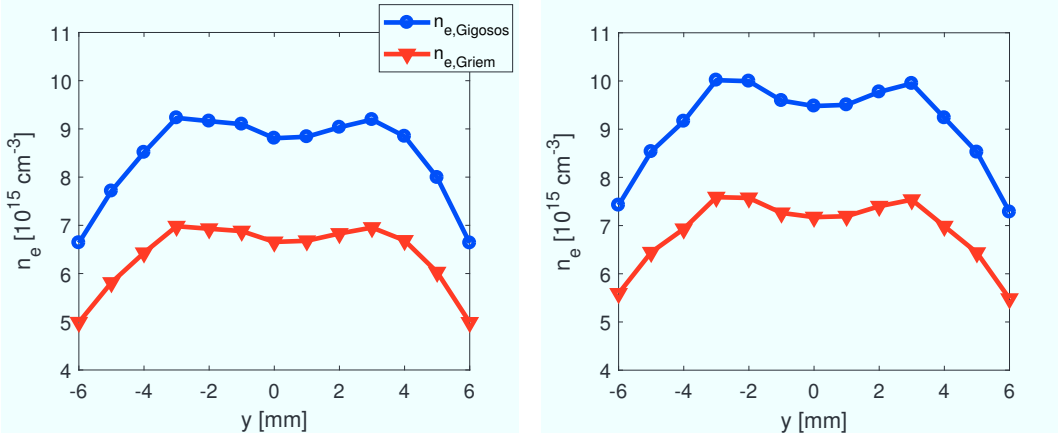

(a) $z = z_{cathode}$*+(19±2) mm* *(b)* $z = z_{anode}$*-(19±2) mm*

Figure C.3: Vertical density scans close to the electrode surfaces at 3 μs *delay after discharge ignition.*

distribution close to the electrodes. As the electrode centre is open to let the beam pass through, the discharge current, which is mainly flowing in longitudinal direction, is higher close to the metal surfaces in close proximity of the electrodes. In the longitudinal centre of the plasma the current is homogeneously distributed (compare Fig. 8.20).

Following the measurement of these inhomogeneities in the plasma density distribution, an experiment on the possibility to deliberately modify the local plasma density was conducted. The diameter of a discharge glass tube was periodically widened, which is believed to locally change the current density during the discharge. Figure C.4 shows the modulated discharge

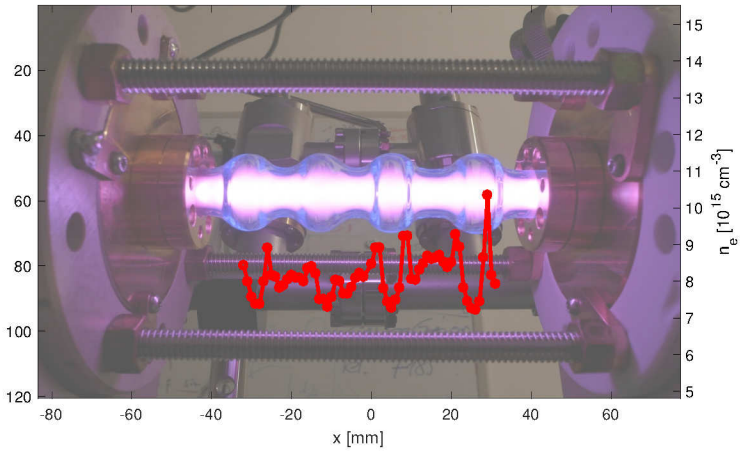

Figure C.4: Picture of the modulated glass discharge vessel with measured electron densities for 2 mbar *initial gas pressure,* 2.4 kV *maximum capacitor voltage and* 3 μs *spectrometer camera delay.*

vessel. Similar modulations can be seen in the measured electron densities: the density measured in the vertical centre of the vessel is lowered at the positions were the glass is wider. The absolute density values are not considered representative, as they are not only integrated over the line of sight through the discharge vessel, but reflections due to the curved glass bulges may allow contributions to the measured densities from other longitudinal positions in the glass. Nevertheless, a tendency is evident from the measurement. A comparison to the density in a flat discharge vessel is shown in Fig. C.5. Measurements at different initial gas pressures and different discharge times are also plotted. The modulation seems to vanish after a few ten microseconds, which is probably due to diffusion/expansion of plasma from high density regions into low density ones. Recombination rates are also higher at higher densities. Varying the pressure allows to change the overall density and maybe also the shape of the modulations, whereas this would have to be determined in density measurements with higher spatial resolution.

The proof-of-principle experiment shows that it is possible to vary the plasma profile in a discharge plasma by modification of the discharge vessel cross-section locally. Applications of this could be e.g. controlling the plasma entrance and exit density ramps or modulation of the plasma density for alternating gradient wakefield acceleration [219].

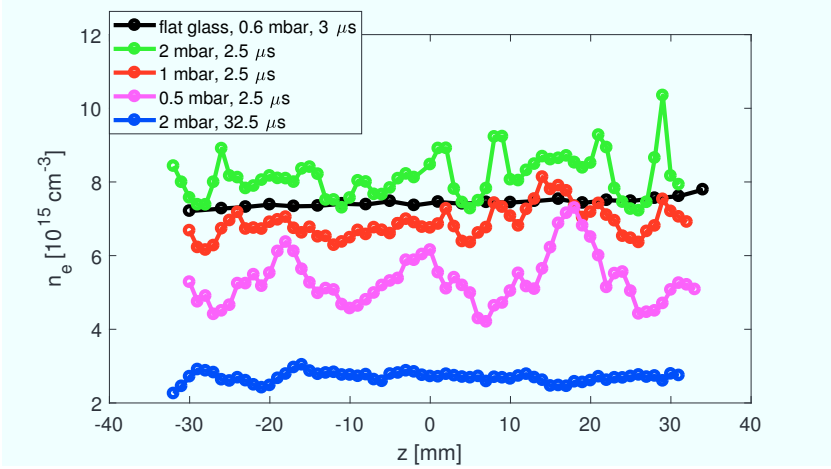

Figure C.5: Comparison of measured longitudinal plasma density profiles in the modulated discharge vessel. Measurements were done with 2.4 kV *maximum capacitor voltage and varying initial gas pressures and density measurement delays.*

Appendix D

Additional transformer ratio measurements

Transformer ratio density dependance

In experiment, the beam parameters (bunch current profile, focusing, driver-witness delay, etc.) were set up and then measurements were conducted for varying plasma density. This allowed to minimise the operation time of the plasma cell (to reduce the strain on the foil windows) and to speed up the measurements as adjustment of the plasma density only required a change of trigger signal delay, which is significantly faster than e.g. adjusting magnet currents. Figure D.1 shows such a plasma trigger delay (plasma density) scan. Each recorded transformer ratio corresponds to a longitudinal phase space measurement of the beam after interaction with the plasma. The depicted measurements also include the measurement discussed in Sec. 10.3 at 275 μs. Even though fluctuations in the measured TRs are apparent, no isolated high TR is measured. High TRs are rather measured over a density range. This agrees with the understanding, that a driver bunch, which is shaped appropriately, produces HTR wakefields for various density but an optimal matching of bunch shape to plasma density and also of driver-witness delay to the plasma density is only achieved at a certain point.

The same TR measurements are plotted against plasma densities in Fig. D.2. Due to the large uncertainty in the plasma density measurement the tendencies in the TR are less obvious. Nevertheless, also in this depiction no isolated high transformer ratio is present.

Plasma density at different beam parameters show similar characteristics, although the TR values in the depicted scan are among the highest measured

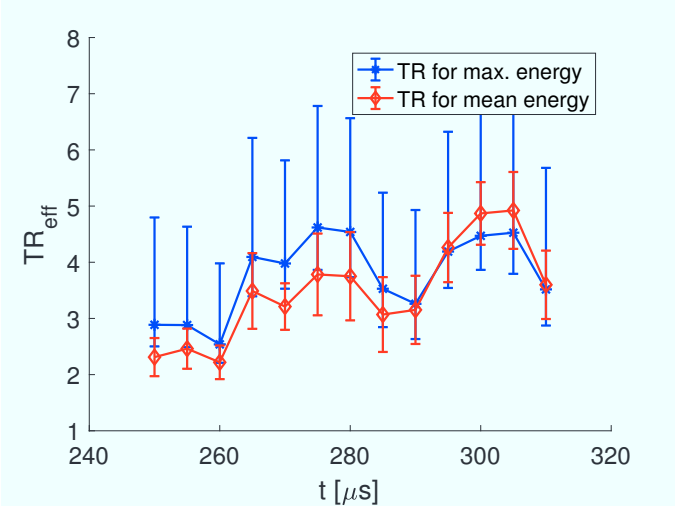

Figure D.1: Measured TRs for varying delay t between discharge ignition and beam arrival at the plasma.

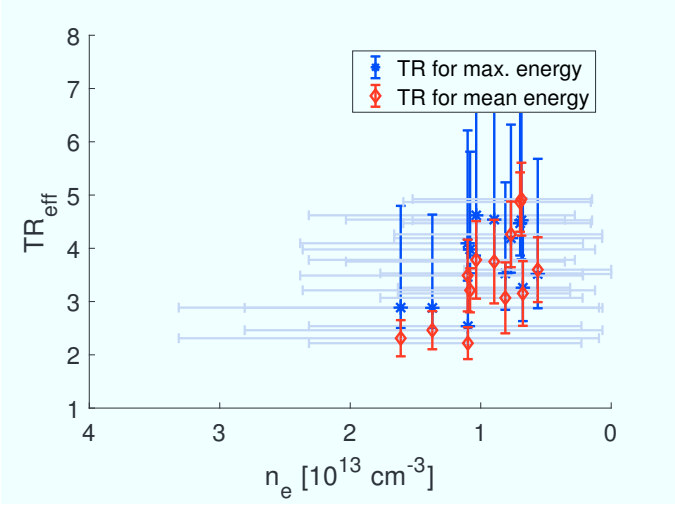

Figure D.2: Measured TRs for varying delay between discharge ignition and beam arrival at the plasma. Discharge delays have been converted to plasma densities, as measured via SMI (see also Sec. 8.4).

values. Variation of the beam parameters can e.g. change the maximum TR values, but also the delays at which they are measured. Nevertheless, no single shot or isolated HTR values have been recorded, which also suggests good stability of the conducted measurements.

PITZ HTR PWFA maximum energy gain

Even though the PITZ PWFA experiments are not designed to achieve maximum acceleration gradients in plasmas, the acceleration gradient is certainly an interesting figure of merit as it is the driving argument for the development of PWFA. Figure D.3 shows the HTR measurement in which the max-

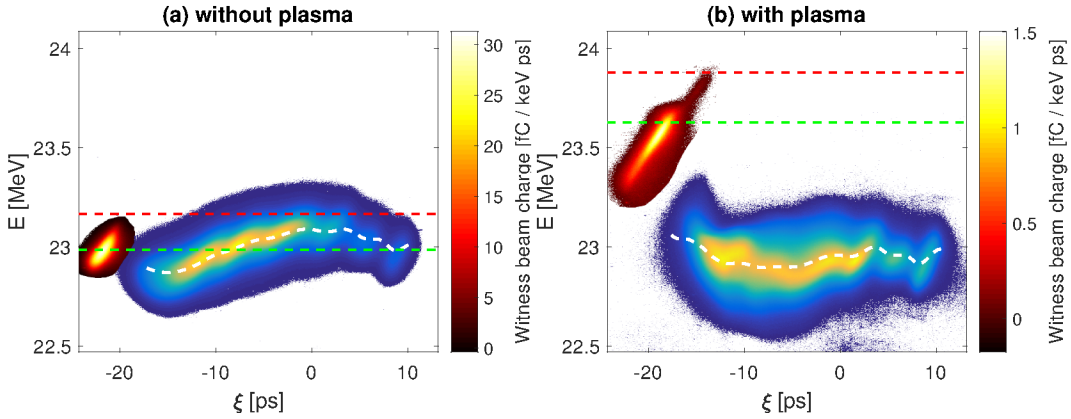

Figure D.3: Longitudinal phase spaces of driver and witness bunches measured without (a) and with (b) interaction with a plasma of $1.4^{+0.6}_{-0.2} \times 10^{13}\ cm^{-3}$ *electron density. The witness bunch (*$\xi \approx$ *-20 ps) was measured with a different camera gain than the driver. Dashed lines indicate witness mean (green) and maximum (red) energies and the driver mean slice energies (white).*

imum witness energy gain was recorded. The driver bunch of (700 ± 19) pC accelerated part of the (29 ± 1) pC witness bunch by 0.71 MeV. Driver and witness beam parameters are similar to the ones which showed the highest measured transformer ratio (see also Sec. 10.4). Maximum witness energy gain was achieved at a slightly higher plasma density of $1.4^{+0.6}_{-0.2} \times 10^{13}\,\mathrm{cm}^{-3}$. The transformer ratio at these parameters was measured to be $R_{eff} = 4.9^{+1.5}_{-0.2}$, with similar uncertainties as the measurement with the maximum recorded TR (Sec. 10.4). Figure D.4 shows the 10 measurements of the witness bunch longitudinal phase space taken for this case. While the high energy tail

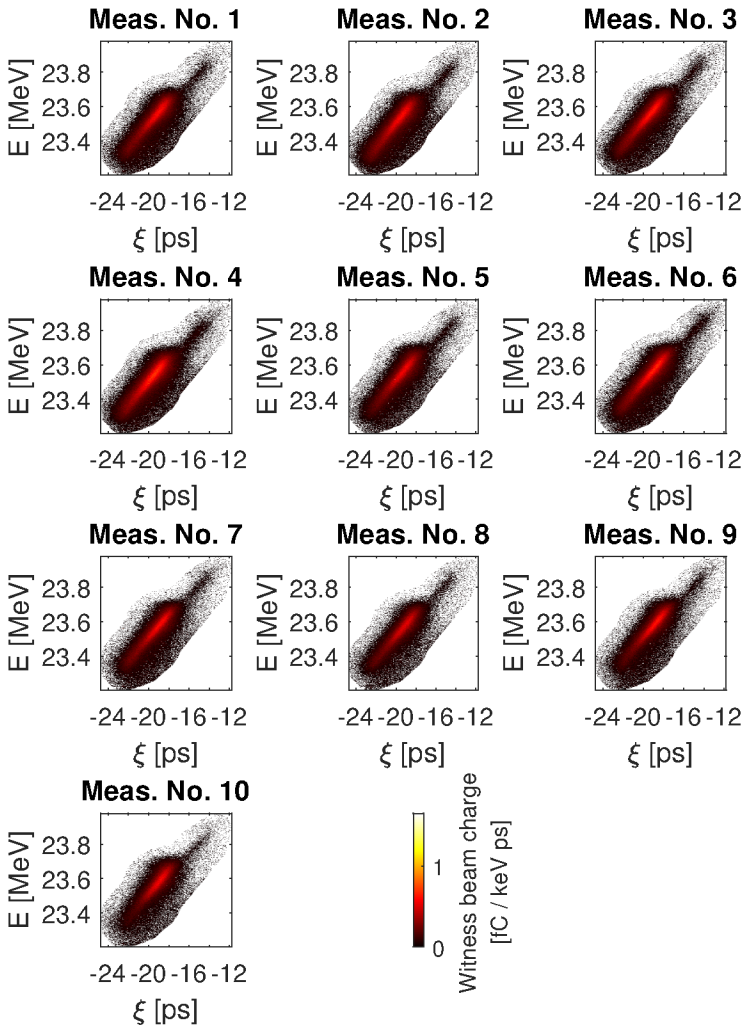

Figure D.4: Longitudinal phase space of the witness beam in 10 consecutive measurements for the beam and plasma parameters, which yielded the highest witness energy gain.

is clearly visible e.g. in measurement number 6, it is hard to distinguish from the background noise in measurement number 10. Other measurements with clear and stable witness beam signal showed witness energy gains up to 0.62 MeV.
For comparison to other acceleration structures, the energy gain is usually divided by the acceleration length to get the acceleration gradient. In case of the PITZ PWFA, the acceleration length is not exactly known. Spectroscopic density measurements (see Sec. 8.4) and simulation of the measured PWFA (see Sec. 10.3) suggest that the plasma column length reduces with delay to the discharge ignition due to outflow of ionised gas through the electrode beam apertures. When assuming a similar interaction length as for the first confirmed HTR measurement (Sec. 10.3), i.e. $\sim$64 mm, the maximum measured witness energy gain corresponds to a gradient of 11 MV/m. Even though this is not nearly as high as the gradients achieved or aimed for in other PWFA experiments, it is still compatible with gradients achieved in conventional metal-cavity based accelerating structures (e.g. PITZ CDS booster cavity typical gradient 17 MV/m).

Index of abbreviations

AC	*Alternating current*: Electrical current that is not continuous but changes amplitude periodically. The usual time-dependency of the current amplitude corresponds to a sine-wave.
CCD	*Charge coupled device*: Electronic sensor used to determine intensity of incident light (see Sec. 8.4 and Ch. 6).
DESY	*Deutsches Elektronen-Synchrotron* www.desy.de
DWA	*Dielectric wakefield accelerator*: Acceleration concept in which wakefields are excited in a dielectric structure by a driver particle beam, via which energy is transferred to a trailing witness beam (see Sec, 1.6).
FEL	*Free electron laser*: Concept for the emission of coherent light from an ensemble of unbound electrons (see Sec. 1.1).
FWHM	*Full width at half maximum*: Difference between argument values of a function, at which the function has dropped to half of its maximum amplitude.
HTR	*High transformer ratio*: Transformer ratio that exceeds the limit of 2 for linear plasma wakefields excited by a longitudinally symmetric driver bunch (see Ch. 3).
IR	*Infrared*: Electromagnetic waves with wavelengths of 700 nm–1000 nm.
Linac	*Linear accelerator*: Particle accelerator through which accelerated particles only pass once.
LPS	*Longitudinal phase space*: space of all possible values of momentum and direction in longitudinal direction (main direction of motion). Also used to describe the area occupied by an ensemble of particles in the space of all possible values.
LWFA	*Laser wakefield accelerator/acceleration*: Concept to accelerate

	particles in a wake, that is excited in a plasma medium by an intense, short laser pulse (see Sec. 1.6).
PITZ	*Photo-Injector Test facility at DESY in Zeuthen*: Research accelerator at the DESY campus Zeuthen (Ch. 6).
PWFA	*Plasma wakefield accelerator/acceleration*: Concept to accelerate particles in a wake that is excited in a plasma medium by the space charge of a high brightness, short particle bunch driver (see Sec. 1.6 and Ch. 2).
RF	*Radiofrequency*: Frequencies between $\sim 9\,\mathrm{kHz}$ and several $100\,\mathrm{GHz}$. Often also used to describe electromagnetic waves in this frequency range.
RMS	*Root mean square*: Square root of the sum of squares of a set of values.
TR	*Transformer ratio*: Ratio between maximum accelerating field behind and maximum decelerating fields within a wakefield driver bunch (see Ch. 3).
UHV	*Ultra-high vacuum*: Vacuum environment at pressures lower than $\sim 10^{-9}\,\mathrm{mbar}$.
UV	*Ultraviolet*: Electromagnetic waves with wavelengths of $10\,\mathrm{nm} - 400\,\mathrm{nm}$.

List of symbols

c	Speed of light 2.998... 10^8 m/s
e	elementary charge 1.602×10^{-19} C
m_e	electron mass 9.109×10^{-31} kg
n_e	unperturbed plasma electron density (see Sec. 2.1)
T_e	plasma electron temperature (see Sec. 2.1)
ω_p	plasma electron characteristic frequency (see Sec. 2.1)
k_p	plasma wave number, inverse plasma skin depth (see Sec. 2.1)
ϵ	beam emittance (see Sec. 1.4)
ϵ_n	normalised beam emittance (see Sec. 1.4)
ϵ_0	vacuum permittivity $8.854\times10^{-12}\ \frac{As}{Vm}$
k_B	Boltzmann constant 1.381×10^{-23} J/K
β	beam amplitude-function (see Sec. 1.4)
γ	beam gamma-function (see Sec. 1.4)
β_b	ratio of particle velocity to speed of light $\beta_b = \frac{v_b eam}{c_0}$
γ_b	relativistic Lorentz-factor $\gamma_b = \frac{1}{\sqrt{1-\beta_b^2}}$
ξ	coordinate along beam axis in the co-moving frame ($\xi = z/c - t$)
R_{eff}	effective transformer ratio, i.e. the ratio of max. witness energy gain to max. driver energy loss in a PWFA

Bibliography

[1] D. Iwanenko and I. Pomeranchuk, "On the Maximal Energy Attainable in a Betatron," *Phys. Rev.*, vol. 65, no. 343, 1944. DOI: https://doi.org/10.1103/PhysRev.65.343.

[2] F. R. Elder, A. M. Gurewitsch, R. V. Langmuir, and H. C. Pollock, "Radiation from Electrons in a Synchrotron," *Phys. Rev.*, vol. 71, pp. 829–830, 1947. DOI: https://doi.org/10.1103/PhysRev.71.829.5.

[3] K. Wille, *Physik der Teilchenbeschleuniger und Synchrotronstrahlungsquellen*. Stuttgart, Germany: B. G. Teubner, 1996. DOI: https://doi.org/10.1007/978-3-663-11039-2.

[4] J. M. J. Madey, "Simulated Emission of Bremsstrahlung in a Periodic Magnetic Field," *J. Appl. Phys.*, vol. 42, no. 5, pp. 1906–1913, 1971. DOI: https://doi.org/10.1063/1.1660466.

[5] CLIC collaboration, "Compact Linear Collider Conceptual Design Report," tech. rep., SLAC, KEK, PSI, JAI, CERN, 2012. URL: http://clic-study.web.cern.ch/content/conceptual-design-report.

[6] ILC collaboration, "International Linear Collider Technical Design Report," tech. rep., ANL, BNL, CEA/irfu, CERN, Cockcroft Inst., Cornell Univ., DESY, Fermilab, IHEP, ILC, INFN, JAI, JINR, JLab, KEK, KNU, LLNL, SLAC, 2013. URL: http://www.linearcollider.org/ILC/Publications/Technical-Design-Report.

[7] F. Zimmermann, M. Benedikt, D. Schulte, and J. Wenninger, "Challenges for Highest Energy Circular Colliders," in *5th International Particle Accelerator Conference*, no. MOXAA01, (Dresden, Germany), pp. 1–6, 2014. URL: http://accelconf.web.cern.ch/AccelConf/IPAC2014/papers/moxaa01.pdf.

[8] J. D. Cockcroft and E. T. Walton, "Artificial Production of Fast Protons," *Nature*, vol. 129, no. 242, 1932. DOI: https://doi.org/10.1038/129242a0.

[9] R. J. Van de Graaff, K. T. Compton, and L. C. Van Atta, "The Electrostatic Production of High Voltage for Nuclear Investigations," *Phys. Rev.*, vol. 43, no. 3, 1933. DOI: https://doi.org/10.1103/PhysRev.43.149.

[10] G. Ising, "Prinzip einer Methode zur Herstellung von Kanalstrahlen hoher Voltzahl," *Arkiv for Matematik, Astronomi och Fysik*, vol. 18, no. 30, pp. 1–4, 1924.

[11] R. Wideröe, "Über ein neues Prinzip zur Herstellung hoher Spannungen," *Archiv für Elektrotechnik*, vol. 21, no. 4, pp. 387–406, 1928. DOI: https://doi.org/10.1007/BF01656341.

[12] A. Degiovanni *et al.*, "High-Gradient Test Results from a CLIC Prototype Accelerating Structure: TD26CC," *Proc. 5th Int. Part. Acc. Conf*, no. WEPME015, pp. 2285–2287, 2014. DOI: https://doi.org/10.18429/JACoW-IPAC2014-WEPME015.

[13] F. Hinterberger, *Physik der Teilchenbeschleuniger und Ionenoptik*. Berlin Heidelberg, Germany: Springer Verlag, 1997. DOI: https://doi.org/10.1007/978-3-540-75282-0.

[14] P. J. Bryant and K. Johnson, *The Principles of Circular Accelerators and Storage Rings*. Cambridge, UK: Cambridge University Press, 1993.

[15] H. Wollnik, *Optics of Charged Particles*. San Diego, USA: Academic Press, Inc., 1987. DOI: https://doi.org/10.1016/B978-0-12-762130-2.X5001-8.

[16] K. Flöttmann, "Some basic features of the beam emittance," *Phys. Rev. Spec. Topics — Acc. and Beams*, vol. 6, no. 034202, 2003. DOI: https://doi.org/10.1103/PhysRevSTAB.6.034202.

[17] R. Q. Twiss and N. H. Frank, "Orbital Stability in a Proton Synchrotron," *Rev. Sci. Instr.*, vol. 20, no. 1, pp. 1–17, 1949. DOI: https://doi.org/10.1063/1.1741343.

[18] E. D. Courant and H. S. Snyder, "Theory of the Alternating-Gradient Synchrotron," *Ann. Phys.*, vol. 3, no. 1, pp. 1–48, 1958. DOI: https://doi.org/10.1016/0003-4916(58)90012-5.

[19] J. W. Gibbs, "On the Fundamental Formula of Statistical Mechanics, with Applications to Astronomy and Thermodynamics," in *Proceedings of the American Association for the Advancement of Science XXXIII*, (Philadelphia, USA), pp. 57–58, 1884.

[20] J. Liouville, "Note on the Theory of the Variation of Arbitrary Constants," *J. Math. Pures Appl.*, vol. 3, pp. 342–349, 1838.

[21] G. Mesyats, *Pulsed Power*. NY, USA: Springer Science+Business Media, Inc., 2005. DOI: https://doi.org/10.1007/b116932.

[22] M. J. Mulcahy and P. C. Bolin, "High Voltage Breakdown Study - Handbook of Vacuum Insulation," Tech. Rep. ECOM-00394-20, United States Army Electronics Command, 1971. URL: https://apps.dtic.mil/dtic/tr/fulltext/u2/723107.pdf.

[23] P. B. Wilson, "Electron Linacs for High Energy Physics," *Rev. Accel. Sci. Tech.*, vol. 1, no. 1, pp. 7–41, 2008. DOI: https://doi.org/10.1142/S1793626808000034.

[24] R. Keinigs, M. E. Jones, and W. Gai, "The Dielectric Wakefield Accelerator," Tech. Rep. No. LA-UR-88-1822, Los Alamos National Laboratory, *also in Argonne National Laboratory Report No. ANL-HEP-PR-88-27*, 1988.

[25] M. Rosing and W. Gai, "Longitudinal- and transverse-wake-field effects in dielectric structures," *Phys. Rev. D*, vol. 42, no. 5, pp. 1829–1834, 1990. DOI: https://doi.org/10.1103/PhysRevD.42.1829.

[26] T. Tajima and J. M. Dawson, "Laser Electron Accelerator," *Phys. Rev. Lett.*, vol. 43, no. 3, pp. 267–270, 1979. DOI: https://doi.org/10.1103/PhysRevLett.43.267.

[27] P. Chen, J. M. Dawson, R. W. Huff, and T. Katsouleas, "Acceleration of Electrons by the Interaction of a Bunched Electron Beam with a Plasma," *Phys. Rev. Lett.*, vol. 54, no. 7, pp. 693–696, 1985. DOI: https://doi.org/10.1103/PhysRevLett.54.693.

[28] G. A. Voss and T. Weiland, "The Wake Field Acceleration Mechanism," Tech. Rep. DESY 82-074, also in M82-10, Deutsches Elektronen-Synchrotron DESY, 1982. URL: http://www-library.desy.de/report82.html.

[29] B. D. O'Shea *et al.*, "Observation of acceleration and deceleration in gigaelectron-volt-per-metre gradient dielectric wakefield accelerators," *Nat. Comm.*, vol. 7, no. 12763, 2016. DOI: https://doi.org/10.1038/ncomms12763.

[30] A. I. Akhiezer and Y. B. Fainberg, "On the Interaction of a Charged Particle Beam with Electron Plasma," *Doklay Academii Nauk SSSR*, vol. 69, no. 555, 1949. URL: http://archive.ujp.bitp.kiev.ua/files/journals/53/si/53SI19p.pdf.

[31] A. I. Ahiezer, "On the Interaction of Electromagnetic Waves with Charged Particles and on the Oscillations of the Electronic Plasma," *Del Nuovo Cimento*, vol. III, no. 4, pp. 591–613, 1956. DOI: https://doi.org/10.1007/BF02746064.

[32] V. I. Veksler, "Coherent Principle of Acceleration of Charged Particles," *Symposium du CERN sur les Accélérateurs de Haute Energie et la Physique des Mesons* π, vol. 1, pp. 80–83, 1956. URL: http://cds.cern.ch/record/1241563/.

[33] V. Malka *et al.*, "Electron Acceleration by a Wake Field Forced by an Intense Ultrashort Laser Pulse," *Science*, vol. 298, pp. 1596–1600, 2002. DOI: https://doi.org/10.1126/science.1076782.

[34] E. Esarey, C. B. Schroeder, and W. P. Leemans, "Physics of laser-driven plasma-based electron accelerators," *Rev. Mod. Phys.*, vol. 81, pp. 1229–1285, 2009. DOI: https://doi.org/10.1103/RevModPhys.81.1229.

[35] D. Strickland and G. Mourou, "Compression of amplified chirped optical pulses," *Optics Communications*, vol. 55, no. 6, pp. 447–449, 1985. DOI: https://doi.org/10.1016/0030-4018(85)90151-8.

[36] W. P. Leemans *et al.*, "Multi-GeV Electron Beams from Capillary-Discharge-Guided Subpetawatt Laser Pulses in the Self-Trapping Regime," *Phys. Rev. Lett.*, vol. 113, no. 245002, 2014. DOI: https://doi.org/10.1103/PhysRevLett.113.245002.

[37] A. J. Gonsalves, K. Nakamura, J. Daniels, *et al.*, "Petawatt Laser Guiding and Electron Beam Acceleration to 8 GeV in a Laser-Heated Capillary Discharge Waveguide," *Phys. Rev. Lett.*, vol. 122, no. 084801, 2019. DOI: https://doi.org/10.1103/PhysRevLett.122.084801.

[38] C. D. Decker and W. B. Mori, "Group Velocity of Large Amplitude Electromagnetic Waves in a Plasma," *Phys. Rev. Lett.*, vol. 72, no. 4, pp. 490–493, 1994. DOI: https://doi.org/10.1103/PhysRevLett.72.490.

[39] F. Grüner *et al.*, "Design considerations for table-top, laser-based VUV and X-ray free electron lasers," *Appl. Phys. B*, vol. 86, pp. 431–435, 2007. DOI: https://doi.org/10.1007/s00340-006-2565-7.

[40] V. Malka *et al.*, "Principles and applications of compact laser-plasma accelerators," *Nature physics*, vol. 4, no. 6, pp. 447–453, 2008. DOI: https://doi.org/10.1038/nphys966.

[41] I. Blumenfeld *et al.*, "Energy doubling of 42 GeV electrons in a metre-scale plasma wakefield accelerator," *Nature Lett.*, vol. 445, pp. 741–744, 2007. DOI: https://doi.org/10.1038/nature05538.

[42] S. Lee *et al.*, "Energy doubler for a linear collider," *Phys. Rev. Spec. Topics Acc. Beams*, vol. 5, no. 011001, 2002. DOI: https://doi.org/10.1038/ncomms12763.

[43] M. C. Thompson, J. B. Rosenzweig, and H. Suk, "Plasma density transition trapping as a possible high-brightness electron beam source," *Phys. Rev. Spec. Topics Acc. Beams*, vol. 7, no. 011301, 2004. DOI: https://doi.org/10.1103/PhysRevSTAB.7.011301.

[44] B. Hidding, G. Pretzler, J. B. Rosenzweig, T. Königstein, D. Schiller, and D. L. Bruhwiler, "Ultracold Electron Bunch Generation via Plasma Photocathode Emission and Acceleration in a Beam-Driven Plasma Blowout," *Phys. Rev. Lett.*, vol. 108, no. 035001, 2012. DOI: https://doi.org/10.1103/PhysRevLett.108.035001.

[45] A. Martinez de la Ossa, J. Grebenyuk, T. Mehrling, L. Schaper, and J. Osterhoff, "High-Quality Electron Beams from Beam-Driven Plasma Accelerators by Wakefield-Induced Ionization Injection," *Phys. Rev. Lett.*, vol. 111, no. 245003, 2013. DOI: https://doi.org/10.1103/PhysRevLett.111.245003.

[46] E. Adli, J. P. Delahaye, S. J. Gessner, M. J. Hogan, T. Raubenheimer, W. An, C. Joshi, and W. Mori, "A Beam Driven Plasma-Wakefield Linear Collider: From Higgs Factory to Multi-TeV," Tech. Rep. SLAC-PUB-15426, SLAC National Accelerator Laboratory, 2013. URL: http://slac.stanford.edu/pubs/slacpubs/15250/slac-pub-15426.pdf.

[47] K.-H. Spatschek, *Theoretische Plasmaphysik*. Stuttgart, Germany: B. G. Teubner, 1990. DOI: https://doi.org/10.1007/978-3-322-84834-5.

[48] F. F. Chen, *Introduction to Plasma Physics and Controlled Fusion*. Cham, Switzerland: Springer International Publishing, 2016. DOI: https://doi.org/10.1007/978-3-319-22309-4.

[49] R. D. Ruth, A. W. Chao, P. L. Morton, and P. B. Wilson, "A Plasma Wake Field Accelerator," Tech. Rep. SLAC-PUB-3374, Stanford Linear Accelerator Center, 1984. URL: http://slac.stanford.edu/pubs/slacpubs/3250/slac-pub-3374.pdf.

[50] L. Tonks and I. Langmuir, "Oscillations in Ionized Gas," *Phys. Rev.*, vol. 33, pp. 195–210, 1929. DOI: https://doi.org/10.1103/PhysRev.33.195.

[51] E. Esarey, P. Sprangle, J. Krall, and A. Ting, "Overview of Plasma-Based Accelerator Concepts," *IEEE Tr. Pl. Sci.*, vol. 24, no. 2, pp. 252–288, 1996. DOI: https://doi.org/10.1109/27.509991.

[52] L. M. Gorbunov and V. I. Kirsanov, "Excitation of plasma waves by an electromagnetic wave packet," *Sov. Phys. JETP*, vol. 66, pp. 290–294, 1987. URL: http://www.jetp.ac.ru/cgi-bin/dn/e_066_02_0290.pdf.

[53] A. Ogata, J. B. Rosenzweig, and M. Ferrario, "Characterization of plasma accelerators with RF linac terminology," *Nucl. Instr. Methods Phys. Res. A*, vol. 410, pp. 549–561, 1998. DOI: https://doi.org/10.1016/S0168-9002(98)00188-0.

[54] W. Lu, C. Huang, M. M. Zhou, W. B. Mori, and T. Katsouleas, "Limits of linear plasma wakefield theory for electron and positron beams," *Phys. Plasmas*, vol. 12, no. 063101, 2005. DOI: https://doi.org/10.1063/1.1905587.

[55] T. Katsouleas, S. Wilks, P. Chen, J. M. Dawson, and J. J. Su, "Beam Loading in Plasma Accelerators," *Part. Accel.*, vol. 22, pp. 81–99, 1987. URL: http://cds.cern.ch/record/898463/.

[56] W. K. H. Panofsky and W. A. Wenzel, "Some Considerations Concerning the Transverse Deflection of Charged Particles in Radio-Frequency Fields," *Rev. Sci. Instr.*, vol. 27, p. 967, 1956. DOI: https://doi.org/10.1063/1.1715427.

[57] K. L. F. Bane, P. Chen, and P. B. Wilson, "On Collinear Wake Field Acceleration," *IEEE Trans. Nucl. Sci.*, vol. NS-32, no. 5, pp. 3524–3526, 1985. DOI: https://doi.org/10.1109/TNS.1985.4334416.

[58] K. L. F. Bane, P. B. Wilson, and T. Weiland, "Wake Fields and Wake Field Acceleration," Tech. Rep. SLAC-PUB-3528, Stanford Linear Accelerator Center, 1984. URL: http://www.slac.stanford.edu/pubs/slacpubs/3500/slac-pub-3528.pdf.

[59] S. A. Heifets and S. A. Kheifets, "Coupling impedance in modern accelerators," *Rev. Mod. Phys.*, vol. 63, no. 3, pp. 631–673, 1991. DOI: https://doi.org/10.1103/RevModPhys.63.631.

[60] J. Seeman, "Collective Electron Driven Linac for High Energy Physics," *IEEE Trans. Nucl. Sci.*, vol. NS-30, no. 4, pp. 3180–3182, 1983. DOI: https://doi.org/10.1109/TNS.1983.4336607.

[61] A. W. Chao, "Coherent Instabilities of a Relativistic Bunched Beam," Tech. Rep. SLAC-PUB-2946, Stanford Linear Accelerator Center, 1982. URL: http://www.slac.stanford.edu/pubs/slacpubs/2750/slac-pub-2946.pdf.

[62] T. R. Lockner and M. Friedman, "The NRL Autoaccelerator Concept," *IEEE Trans. Nucl. Sci.*, vol. NS-26, no. 3, pp. 4237–4238, 1979. DOI: https://doi.org/10.1109/TNS.1979.4330756.

[63] P. Chen and J. M. Dawson, "The Plasma Wakefield Accelerator," Tech. Rep. SLAC-PUB-3601, Stanford Linear Accelerator Center, 1985. URL: http://www.slac.stanford.edu/cgi-wrap/getdoc/slac-pub-3601.pdf.

[64] P. Chen, J. J. Su, J. M. Dawson, K. L. F. Bane, and P. B. Wilson, "Energy Transfer in the Plasma Wake-Field Accelerator," *Phys. Rev.*

Lett., vol. 56, no. 12, pp. 1252–1255, 1986. DOI: https://doi.org/10.1103/PhysRevLett.56.1252.

[65] B. Jiang, C. Jing, P. Schoessow, J. Power, and W. Gai, "Formation of a novel shaped bunch to enhance transformer ratio in collinear wakefield accelerators," *Phys. Rev. Spec. Topics Acc. Beams*, vol. 15, no. 011301, 2012. DOI: https://doi.org/10.1103/PhysRevSTAB.15.011301.

[66] V. I. Maslov, I. N. Onishchenko, and I. P. Yarovaya, "Transformation Ratio at Plasma Wakefield Excitation by Long Electron Bunch with Shaping of its Charge According Cosine," *East Europ. J. Phys.*, vol. 1, no. 4, pp. 84–87, 2014. URL: http://nbuv.gov.ua/UJRN/eejph_2014_1_4_11.

[67] K. V. Lotov, "Efficient operating mode of the plasma wakefield accelerator," *Phys. Plasmas*, vol. 12, no. 053105, 2005. DOI: https://doi.org/10.1063/1.1889444.

[68] F. Lemery and P. Piot, "Tailored electron bunches with smooth current profiles for enhanced transformer ratios in beam-driven acceleration," *Phys. Rev. Spec. Topics Acc. Beams*, vol. 18, no. 081301, 2015. DOI: https://doi.org/10.1103/PhysRevSTAB.18.081301.

[69] T. Katsouleas, "Physical mechanisms in the plasma wake-field accelerator," *Phys. Rev. A*, vol. 33, no. 3, pp. 2056–2064, 1986. DOI: https://doi.org/10.1103/PhysRevA.33.2056.

[70] Q. Gao *et al.*, "Observation of High Transformer Ratio of Shaped Bunch Generated by an Emittance-Exchange Beam Line," *Phys. Rev. Lett.*, vol. 120, no. 114801, 2018. DOI: https://doi.org/10.1103/PhysRevLett.120.114801.

[71] E. M. Laziev, V. M. Tsakanov, and S. S. Vahanyan, "Electromagnetic Wave Generation with High Transformation Ratio by Intense Charged Particle Bunches," Tech. Rep. EFI-1040(3)-88, Yerevan Physics Institute, 1988. URL: https://inis.iaea.org/search/search.aspx?orig_q=RN:21094563.

[72] E. M. Laziev, V. M. Tsakanov, and S. S. Vahanyan, "Electromagnetic Wave Generation with High Transformation Ratio by Intense Charged Particle Bunches," in *1st European Particle Accelerator Conference*,

(Rome, Italy), pp. 523–525, 1988. URL: https://accelconf.web.cern.ch/accelconf/e88/PDF/EPAC1988_0523.PDF.

[73] P. Schütt, T. Weiland, and V. M. Tsakanov, "On the Wake Field Acceleration Using the Sequence of Driving Bunches," Tech. Rep. M-88-13, Deutsches Elektronen-Synchrotron DESY, 1988. URL: https://bib-pubdb1.desy.de/record/275440.

[74] K. Nakajima, "Plasma Wake-Field Accelerator Driven by a Train of Multiple Bunches," *Part. Accel.*, vol. 32, pp. 209–214, 1990. URL: http://cds.cern.ch/record/201643/files/p209.pdf.

[75] V. M. Tsakanov, "On collinear wake field acceleration with high transformer ratio," *Nucl. Instr. Methods Phys. Res. A*, vol. 432, pp. 202–213, 1999. DOI: https://doi.org/10.1016/S0168-9002(99)00378-2.

[76] E. Kallos, *Plasma Wakefield Accelerators Using Multiple Electron Bunches*. PhD thesis, University of Southern California, 2008. DOI: http://digitallibrary.usc.edu/cdm/compoundobject/collection/p15799coll127/id/197855/rec/2.

[77] J. G. Power, W. Gai, and A. Kanareykin, "Transformer Ratio Enhancement Using A Ramped Bunch Train In A Collinear Wakefield Accelerator," in *9th Advanced Accelerator Concepts Workshop*, (Santa Fe, USA), pp. 605–615, 2001. DOI: https://doi.org/10.1063/1.1384388.

[78] J. G. Power, W. Gai, X. Sun, and A. Kanareykin, "Transformer Ratio Enhancement Using a Ramped Bunch Train in a Collinear Wakefield Accelerator," in *Particle Accelerator Conference*, (Chicago, USA), pp. 114–116, 2001. DOI: https://doi.org/10.1109/PAC.2001.987446.

[79] J. P. Farmer, R. Martorelli, and A. Pukhov, "Transformer ratio saturation in a beam-driven wakefield accelerator," *Phys. Plasmas*, vol. 22, p. 123113, 2015. DOI: https://doi.org/10.1063/1.4938038.

[80] J. B. Rosenzweig, G. Andonian, M. Ferrario, P. Muggli, O. Williams, V. Yakimenko, and K. Xuan, "Plasma Wakefields in the Quasi-Nonlinear Regime," in *14th Advanced Accelerator Concepts Workshop*, (Annapolis, USA), pp. 500–504, 2010. DOI: http://dx.doi.org/10.1063/1.3520373.

[81] J. B. Rosenzweig *et al.*, "Plasma wakefields in the quasi-nonlinear regime: Experiments at ATF," in *15th Advanced Accelerator Concepts Workshop*, (Austin, USA), pp. 612–617, 2012. DOI: http://dx.doi.org/10.1063/1.4773767.

[82] E. Chiadroni *et al.*, "Beam manipulation for resonant plasma wakefield acceleration," *Nucl. Instr. Methods Phys. Res. A*, vol. 865, pp. 139–143, 2017. DOI: http://dx.doi.org/10.1016/j.nima.2017.01.017.

[83] C. Jing *et al.*, "Observation of Enhanced Transformer Ratio in Collinear Wakefield Acceleration," *Phys. Rev. Lett.*, vol. 98, no. 144801, 2007. DOI: https://doi.org/10.1103/PhysRevLett.98.144801.

[84] C. Jing, J. G. Power, M. Conde, W. Liu, Z. Yusof, A. Kanareykin, and W. Gai, "Increasing the transformer ratio at the Argonne wakefield accelerator," *Phys. Rev. Spec. Top. Accel. Beams*, vol. 14, no. 021302, 2011. DOI: https://doi.org/10.1103/PhysRevSTAB.14.021302.

[85] R. Brinkmann. DESY internal note, 2011.

[86] G. Asova, A. Oppelt, F. Stephan, and T. Vinatier, "Towards high transformer ratios for plasma wakefield acceleration at PITZ," in *Verhandlungen der Deutschen Physikalischen Gesellschaft*, (Dresden, Germany), 2014.

[87] S. van der Meer, "Improving the Power Efficiency of the Plasma Wakefield Accelerator," Tech. Rep. CERN/PS/85-65, CLIC Note No. 3, European Organization for Nuclear Research, 1985. URL: http://cds.cern.ch/record/163918/.

[88] M. Tzoufras *et al.*, "Beam Loading in the Nonlinear Regime of Plasma-Based Acceleration," *Phys. Rev. Lett.*, vol. 101, no. 145002, 2008. DOI: https://doi.org/10.1103/PhysRevLett.101.145002.

[89] R. D. Ruth and P. Chen, "Plasma Accelerators," Tech. Rep. SLAC-PUB-3906, Stanford Linear Accelerator Center, 1986. URL: http://www.slac.stanford.edu/cgi-wrap/getdoc/slac-pub-3906.pdf.

[90] S. Wilks, T. Katsouleas, J. M. Dawson, P. Chen, and J. J. Su, "Beam Loading in Plasma Waves," *IEEE Trans. Plasma. Sci.*, vol. PS-15, no. 2, pp. 210–217, 1987. DOI: https://doi.org/10.1109/TPS.1987.4316687.

[91] J. J. Su, J. M. Dawson, T. Katsouleas, S. Wilks, P. Chen, M. Jones, and R. Keinigs, "Stability of the Driving Bunch in the Plasma Wakefield Accelerator," *Trans. Plasma Sci.*, vol. 15, no. 2, pp. 192–198, 1987. DOI: https://doi.org/10.1109/TPS.1987.4316684.

[92] R. Keinigs and M. E. Jones, "Two-dimensional dynamics of the plasma wakefield accelerator," *Phys. Fluids*, vol. 30, pp. 252–263, 1987. DOI: https://doi.org/10.1063/1.866183.

[93] J. Krall and G. Joyce, "Transverse equilibrium and stability of the primary beam in the plasma wake-field accelerator," *Phys. Plasmas*, vol. 2, pp. 1326–1331, 1995. DOI: https://doi.org/10.1063/1.871344.

[94] K. V. Lotov, "Simulation of ultrarelativistic beam dynamics in the plasma wake-field accelerator," *Nucl. Instr. Methods Phys. Res. A*, vol. 410, pp. 461–468, 1998. DOI: https://doi.org/10.1016/S0168-9002(98)00178-8.

[95] K. V. Lotov, "Instability of Long Driving Beams in Plasma Wakefield Accelerators," in *6th European Particle Accelerator Conference*, no. MOP12E, (Stockholm, Sweden), pp. 806–808, 1998. URL: http://accelconf.web.cern.ch/AccelConf/e98/PAPERS/MOP12E.PDF.

[96] R. Lee and M. Lampe, "Electromagnetic Instabilities, Filamentation and Focusing of Relativistic Electron Beams," *Phys. Rev. Lett.*, vol. 31, no. 23, pp. 1390–1393, 1973. DOI: https://doi.org/10.1103/PhysRevLett.31.1390.

[97] Y. Sentoku, K. Mima, P. Kaw, and K. Nishikawa, "Anomalous Resistivity Resulting from MeV-Electron Transport in Overdense Plasma," *Phys. Rev. Lett.*, vol. 90, no. 155001, 2003. DOI: https://doi.org/10.1103/PhysRevLett.90.155001.

[98] A. Bret, M.-C. Firpo, and C. Deutsch, "Characterization of the Initial Filamentation of a Relativistic Electron Beam Passing through a Plasma," *Phys. Rev. Lett.*, vol. 94, no. 115002, 2005. DOI: https://doi.org/10.1103/PhysRevLett.94.115002.

[99] E. S. Weibel, "Spontaneously Growing Transverse Waves in a Plasma due to an Anisotropic Velocity Distribution," *Phys. Rev. Lett.*, vol. 2, no. 3, pp. 83–84, 1959. DOI: https://doi.org/10.1103/PhysRevLett.2.83.

[100] V. B. Pathak, T. Grismayer, A. Stockem, R. A. Fonseca, and L. O. Silva, "Spatial-temporal evolution of the current filamentation instability," *New J. Phys.*, vol. 17, no. 043049, 2015. DOI: http://dx.doi.org/10.1088/1367-2630/17/4/043049.

[101] B. Allen, V. Yakimenko, M. Babzien, M. Fedurin, K. Kusche, and P. Muggli, "Experimental Study of the Current Filamentation Instability," *Phys. Rev. Lett.*, vol. 109, no. 185007, 2012. DOI: https://doi.org/10.1103/PhysRevLett.109.185007.

[102] D. H. Whittum, W. M. Sharp, S. S. Yu, M. Lampe, and G. Joyce, "Electron-Hose Instability in the Ion-Focused Regime," *Phys. Rev. Lett.*, vol. 67, no. 8, pp. 991–994, 1991. DOI: https://doi.org/10.1103/PhysRevLett.67.991.

[103] H. L. Buchanan, "Electron beam propagation in the ion-focused regime," *Phys. Fluids*, vol. 30, pp. 221–231, 1987. DOI: https://doi.org/10.1063/1.866173.

[104] M. Lampe, G. Joyce, and S. P. Slinker, "Electron-hose instability of a relativistic electron beam in an ion-focusing channel," *Phys. Fluids B*, vol. 5, pp. 1888–1901, 1993. DOI: https://doi.org/10.1063/1.860772.

[105] D. H. Whittum, "Cumulative hose instabilities of a magnetically self-focused slab electron beam," *Phys. Fluids B*, vol. 5, pp. 4432–4455, 1993. DOI: https://doi.org/10.1063/1.860559.

[106] E. S. Dodd, R. G. Hemker, C.-K. Huang, S. Wang, C. Ren, and W. B. Mori, "Hosing and Sloshing of Short-Pulse GeV-Class Wakefield Drivers," *Phys. Rev. Lett.*, vol. 88, no. 125001, 1993. DOI: https://doi.org/10.1103/PhysRevLett.88.125001.

[107] M. J. Hogan *et al.*, "E-157: A 1.4-m-long plasma wakefield acceleration experiment using a 30 GeV electron beam from the Stanford Linear Accelerator Center Linac," *Phys. Plasmas*, vol. 7, no. 5, pp. 2241–2248, 2000. DOI: https://doi.org/10.1063/1.874059.

[108] M. J. Hogan *et al.*, "Multi-GeV Energy Gain in a Plasma-Wakefield Accelerator," *Phys. Rev. Lett.*, vol. 95, no. 054802, 2005. DOI: https://doi.org/10.1103/PhysRevLett.95.054802.

[109] T. J. Mehrling, R. A. Fonseca, A. Martinez de la Ossa, and J. Vieira, "Mitigation of the Hose Instability in Plasma-Wakefield Accelerators," *Phys. Rev. Lett.*, vol. 118, no. 174801, 2017. DOI: https://doi.org/10.1103/PhysRevLett.118.174801.

[110] A. Martinez de la Ossa, T. J. Mehrling, and J. Osterhoff, "Intrinsic Stabilization of the Drive Beam in Plasma-Wakefield Accelerators," *Phys. Rev. Lett.*, vol. 121, no. 064803, 2018. DOI: https://doi.org/10.1103/PhysRevLett.121.064803.

[111] T. J. Mehrling, C. Benedetti, C. B. Schroeder, E. Esarey, and W. P. Leemans, "Suppression of Beam Hosing Plasma Accelerators with Ion Motion," *Phys. Rev. Lett.*, vol. 121, no. 264802, 2018. DOI: https://doi.org/10.1103/PhysRevLett.121.264802.

[112] N. Kumar, A. Pukhov, and K. Lotov, "Self-Modulation Instability of a Long Proton Bunch in Plasmas," *Phys. Rev. Lett.*, vol. 104, no. 255003, 2010. DOI: https://doi.org/10.1103/PhysRevLett.104.255003.

[113] A. Caldwell, K. Lotov, A. Pukhov, and F. Simon, "Proton-driven plasma-wakefield acceleration," *Nat. Phys.*, vol. 5, pp. 363–367, 2009. DOI: https://doi.org/10.1038/NPHYS1248.

[114] C. B. Schroeder, C. Benedetti, E. Esarey, F. J. Grüner, and W. P. Leemans, "Growth and Phase Velocity of Self-Modulated Beam-Driven Plasma Waves," *Phys. Rev. Lett.*, vol. 107, no. 145002, 2011. DOI: https://doi.org/10.1103/PhysRevLett.107.145002.

[115] A. Pukhov *et al.*, "Phase Velocity and Particle Injection in a Self-Modulated Proton-Driven Plasma Wakefield Accelerator," *Phys. Rev. Lett.*, vol. 107, no. 145003, 2011. DOI: https://doi.org/10.1103/PhysRevLett.107.145003.

[116] C. B. Schroeder, C. Benedetti, E. Esarey, F. J. Grüner, and W. P. Leemans, "Particle beam self-modulation instability in tapered and inhomogeneous plasma," *Phys. Plasmas*, vol. 19, no. 010703, 2012. DOI: https://doi.org/10.1063/1.3677358.

[117] C. B. Schroeder, C. Benedetti, E. Esarey, F. J. Grüner, and W. P. Leemans, "Coherent seeding of self-modulated plasma wakefield accelerators," *Phys. Plasmas*, vol. 20, no. 056704, 2013. DOI: https://doi.org/10.1063/1.4803073.

[118] J. Vieira, Y. Fang, W. B. Mori, L. O. Silva, and P. Muggli, "Transverse self-modulation of ultra-relativistic lepton beams in the plasma wakefield accelerator," *Phys. Plasmas*, vol. 19, no. 063105, 2012. DOI: https://doi.org/10.1063/1.4725425.

[119] K. V. Lotov, "Physics of beam self-modulation in plasma wakefield accelerators," *Phys. Plasmas*, vol. 22, no. 103110, 2015. DOI: https://doi.org/10.1063/1.4933129.

[120] J. B. Rosenzweig, B. Breizman, T. Katsouleas, and J. J. Su, "Acceleration and focusing of electrons in two-dimensional nonlinear plasma wake fields," *Phys. Rev. A*, vol. 44, no. 10, pp. R6189–R6192, 1991. DOI: https://doi.org/10.1103/PhysRevA.44.R6189.

[121] J. B. Rosenzweig, "Nonlinear Plasma Dynamics in the Plasma Wake-Field Accelerator," *Phys. Rev. Lett.*, vol. 58, no. 6, pp. 555–558, 1987. DOI: https://doi.org/10.1103/PhysRevLett.58.555.

[122] N. Barov, J. B. Rosenzweig, M. C. Thompson, and R. B. Yoder, "Energy loss of a high-charge bunched electron beam in plasma: Analysis," *Phys. Rev. Spec. Top. Accel. Beams*, vol. 7, no. 061301, 2004. DOI: https://doi.org/10.1103/PhysRevSTAB.7.061301.

[123] J. B. Rosenzweig, N. Barov, M. C. Thompson, and R. B. Yoder, "Energy loss of a high-charge bunched electron beam in plasma: Simulations, scaling and accelerating wakefields," *Phys. Rev. Spec. Top. Accel. Beams*, vol. 7, no. 061302, 2004. DOI: https://doi.org/10.1103/PhysRevSTAB.7.061302.

[124] J. J. Su, T. Katsouleas, J. M. Dawson, and R. Fedele, "Plasma lenses for focusing particle beams," *Phys. Rev. A*, vol. 41, no. 6, pp. 3321–3331, 1990. DOI: https://doi.org/10.1103/PhysRevA.41.3321.

[125] B. S., N. Naumova, F. Pegoraro, and J. Sakai, "Particle injection into the wave acceleration phase due to nonlinear wake wave breaking," *Phys. Rev. E*, vol. 58, no. 5, pp. R5257–R5260, 1998. DOI: https://doi.org/10.1103/PhysRevE.58.R5257.

[126] A. Pukhov and J. Meyer-ter Vehn, "Laser wake field acceleration: the highly non-linear broken-wave regime," *Appl. Phys. B*, vol. 74, pp. 355–361, 2002. DOI: https://doi.org/10.1007/s003400200795.

[127] H. Suk, N. Barov, J. B. Rosenzweig, and E. Esarey, "Plasma Electron Trapping and Acceleration in a Plasma Wake Field Using a Density Transition," *Phys. Rev. Lett.*, vol. 86, no. 6, pp. 1011–1014, 2001. DOI: https://doi.org/10.1103/PhysRevLett.86.1011.

[128] C. B. Schroeder, E. Esarey, B. A. Shadwick, and W. P. Leemans, "Trapping, dark current, and wave breaking in nonlinear plasma waves," *Phys. Plasmas*, vol. 13, no. 033103, 2006. DOI: https://doi.org/10.1063/1.2173960.

[129] W. Lu, C. Huang, M. Zhou, W. B. Mori, and T. Katsouleas, "Nonlinear Theory for Relativistic Plasma Wakefields in the Blowout Regime," *Phys. Rev. Lett.*, vol. 96, no. 165002, 2006. DOI: https://doi.org/10.1103/PhysRevLett.96.165002.

[130] S. A. Yi, V. Khudik, C. Siemon, and G. Shvets, "Analytical model of electromagnetic fields around a plasma bubble in the blow-out regime," *Phys. Plasmas*, vol. 20, no. 013108, 2013. DOI: https://doi.org/10.1063/1.4775774.

[131] E. A. Jackson, "Nonlinear Oscillations in a Cold Plasma," *Phys. Fluids*, vol. 3, pp. 831–834, 1960. DOI: https://doi.org/10.1063/1.1706133.

[132] F. F. Chen, "Excitation of Large Amplitude Plasma Waves," *Phys. Scr.*, vol. T30, pp. 14–23, 1990. DOI: https://doi.org/10.1088/0031-8949/1990/T30/003.

[133] I. Blumenfeld *et al.*, "Scaling of the longitudinal electric field and transformer ratio in a nonlinear plasma wakefield accelerator," *Phys. Rev. Spec. Top. Accel. Beams*, vol. 12, no. 111301, 2010. DOI: https://doi.org/10.1103/PhysRevSTAB.13.111301.

[134] N. Barov, J. B. Rosenzweig, M. E. Conde, W. Gai, and J. G. Power, "Observation of plasma wakefield acceleration in the underdense regime," *Phys. Rev. Spec. Top. Accel. Beams*, vol. 3, no. 011301, 2000. DOI: https://doi.org/10.1103/PhysRevSTAB.3.011301.

[135] K. V. Lotov, "Blowout regimes of plasma wakefield acceleration," *Phys. Rev. E*, vol. 69, no. 046405, 2004. DOI: https://doi.org/10.1103/PhysRevE.69.046405.

[136] H. Grote and F. Schmidt, "MAD-X – An Upgrade From MAD8," in *2003 Particle Accelerator Conference*, no. FPAG014, (Portland, USA), pp. 3497–3499, 2003. DOI: https://doi.org/10.1109/PAC.2003.1289960.

[137] M. Borland, "ELEGANT: A flexible SDDS-compliant code for accelerator simulation," Tech. Rep. LS-287, Argonne National Laboratory, 2000. DOI: https://doi.org/10.2172/761286.

[138] K. Floettmann, "ASTRA: A Space Charge Tracking Algorithm," *Manual*, vol. 3.2, 2017. URL: http://www.desy.de/~mpyflo/.

[139] A. Friedman *et al.*, "3D Particle Simulation of Beams Using the WARP Code: Transport Around Bends," *Part. Accel.*, vol. 37–38, pp. 131–139, 1992. URL: http://cds.cern.ch/record/1054703/files/.

[140] R. A. Fonseca *et al.*, "OSIRIS: A three-dimensional, fully relativistic particle in cell code for modeling plasma based accelerators," in *2002 Int. Conf. Comp. Sci. ICCS*, pp. 342–351, 2002. DOI: https://doi.org/10.1007/3-540-47789-6_36.

[141] R. A. Fonseca *et al.*, "One-to-one direct modeling of experiments and astrophysical scenarios: pushing the envelope on kinetic plasma simulations," *Plasma Phys. Control. Fusion*, vol. 50, no. 124034, 2008. DOI: dx.doi.org/10.1088/0741-3335/50/12/124034.

[142] K. V. Lotov, "Simulation of ultrarelativistic beam dynamics in plasma wake-field accelerator," *Phys. Plasmas*, vol. 5, no. 3, pp. 785–791, 1998. DOI: https://doi.org/10.1063/1.872765.

[143] K. V. Lotov, "Fine wakefield structure in the blowout regime of plasma wakefield accelerators," *Phys. Rev. Spec. Top. Accel. Beams*, vol. 6, no. 061301, 2003. DOI: https://doi.org/10.1103/PhysRevSTAB.6.061301.

[144] C. Huang *et al.*, "Quickpic: A highly efficient particle-in-cell code for modeling wakefield acceleration in plasmas," *J. Comp. Phys.*, vol. 217, pp. 658–679, 2006. DOI: https://doi.org/10.1016/j.jcp.2006.01.039.

[145] T. Mehrling, C. Benedetti, C. B. Schroeder, and J. Osterhoff, "HiPACE: a quasi-static particle-in-cell code," *Plasma Phys. Control. Fusion*, vol. 56, no. 084012, 2014. DOI: dx.doi.org/10.1088/0741-3335/56/8/084012.

[146] K. S. Yee, "Numerical Solution of Initial Boundary Value Problems Involving Maxwell's Equations in Isotropic Media," *IEEE Trans. Antennas Propagation*, vol. AP-14, no. 8, pp. 302–307, 1966. DOI: https://doi.org/10.1109/TAP.1966.1138693.

[147] R. Courant, K. Friedrichs, and H. Lewy, "Über die partiellen Differenzengleichungen der mathematischen Physik," *Mathematische Annalen*, vol. 100, no. 1, pp. 32–74, 1928. DOI: https://doi.org/10.1007/BF01448839.

[148] P. Mora and T. M. Antonsen, "Electron cavitation and acceleration in the wake of an ultraintense, self-focused, laser pulse," *Phys. Rev. E*, vol. 53, no. 3, pp. R2068–R2071, 1996. DOI: https://doi.org/10.1103/PhysRevE.53.R2068.

[149] D. H. Whittum, "Transverse two-stream instability of a beam with a Bennett profile," *Phys. Plasmas*, vol. 4, no. 1154, 1997. DOI: https://doi.org/10.1063/1.872202.

[150] E. Esarey, B. A. Schadwick, P. Catravas, and W. P. Leemans, "Synchrotron radiation from electron beams in plasma-focusing channels," *Phys. Rev. E*, vol. 65, no. 056505, 2002. DOI: https://doi.org/10.1103/PhysRevE.65.056505.

[151] F. Stephan, C. H. Boulware, M. Krasilnikov, J. Bähr, *et al.*, "Detailed characterization of electron sources yielding first demonstration of European X-ray Free-Electron Laser beam quality," *Phys. Rev. Spec. Top. Accel. Beams*, vol. 13, no. 020704, 2010. DOI: https://doi.org/10.1103/PhysRevSTAB.13.020704.

[152] M. Krasilnikov, F. Stephan, *et al.*, "Experimentally minimized beam emittance from an *L*-band photoinjector," *Phys. Rev. Spec. Top. Accel. Beams*, vol. 15, no. 100701, 2012. DOI: https://doi.org/10.1103/PhysRevSTAB.15.100701.

[153] P. Piot, "Photoinjectors R&D for Future Light Sources & Linear Colliders," in *Linear Accelerator Conference LINAC*, no. TH3001, (Knoxville,

USA), pp. 549–553, 2006. URL: http://accelconf.web.cern.ch/AccelConf/l06/PAPERS/TH3001.PDF.

[154] A. Einstein, "Ueber einen die Erzeugung und Verwandlung des Lichtes betreffenden heuristischen Gesichtspunkt," *Annalen der Physik*, vol. 322, no. 6, pp. 132–148, 1905. DOI: https://doi.org/10.1002/andp.19053220607.

[155] B. E. Carlsten, "New Photoelectric Injector Design for the Los Alamos National Laboratory XUV FEL Accelerator," *Nucl. Instr. Methods. Phys. Res. A*, vol. 285, pp. 313–319, 1989. DOI: https://doi.org/10.1016/0168-9002(89)90472-5.

[156] W. Ackermann *et al.*, "Operation of a free-electron laser from the extreme ultraviolet to the water window," *Nat. Phot.*, vol. 1, pp. 336–342, 2007. DOI: https://doi.org/10.1038/nphoton.2007.76.

[157] M. Altarelli *et al.*, "The European X-ray Free-Electron Laser," Tech. Rep. DESY 2006-097, Deutsches Elektronen-Synchrotron DESY, 2006. URL: http://xfel.desy.de/technical_information/tdr/tdr/.

[158] K. Flöttmann, "Note on the thermal emittance of electrons emitted by Cesium Telluride photo cathodes," Tech. Rep. TESLA-FEL 97-01, Deutsches Elektronen-Synchrotron DESY, 1997. URL: http://bib-pubdb1.desy.de/record/414634.

[159] I. Will and G. Klemz, "Generation of flat-top picosecond pulses by coherent pulse stacking in a multicrystal birefringent filter," *Opt. Express*, vol. 16, no. 19, 2008. DOI: https://doi.org/10.1364/OE.16.014922.

[160] B. Instrumentation, *Integrating Current Transformer User's Manual*, rev. 4.0 ed. URL: http://www.bergoz.com/sites/www.bergoz.com/files/ictmanual4-0_0.

[161] D. Malyutin, *Time resolved transverse and longitudinal phase space measurements at the high brightness photo injector PITZ*. PhD thesis, University of Hamburg, 2014. URL: http://bib-pubdb1.desy.de/record/171168.

[162] V. V. Paramonov *et al.*, "Design Parameters of the Normal Conducting Booster Cavity for the PITZ-2 Test Stand," in *Linear Accelerator Conference LINAC*, no. MOP77, (Lübeck, Germany), pp. 204–

206, 2004. URL: http://accelconf.web.cern.ch/AccelConf/l04/PAPERS/MOP77.PDF.

[163] P. Emma, J. Frisch, and P. Krejcik, "A Transverse RF Deflecting Structure for Bunch Length and Phase Space Diagnostics," Tech. Rep. LCLS-TN-0012, LCC–047, Stanford Linear Accelerator Center SLAC, 2000. URL: https://www-ssrl.slac.stanford.edu/lcls/technotes/lcls-tn-00-12.pdf.

[164] L. Kravchuk *et al.*, "Layout of the PITZ Transverse Deflecting System for Longitudinal Phase Space and Slice Emittance Measurements," in *Linear Accelerator Conference LINAC*, (Tsukuba, Japan), pp. 416–418, 2010. URL: http://accelconf.web.cern.ch/AccelConf/LINAC2010/papers/tup011.pdf.

[165] H. Huck *et al.*, "Progress on the PITZ TDS," in *International Beam Instrumentation Conference IBIC*, no. WEPG47, (Barcelona, Spain), pp. 744–747, 2016. URL: http://accelconf.web.cern.ch/AccelConf/ibic2016/papers/wepg47.pdf.

[166] S. Khodyachykh *et al.*, "Design of Multipurpose Dispersive Section at PITZ," in *International Free-Electron Laser Conference FEL*, no. THPPH020, (Berlin, Germany), pp. 601–604, 2006. URL: http://accelconf.web.cern.ch/AccelConf/f06/PAPERS/THPPH020.PDF.

[167] S. Rimjaem *et al.*, "Physics and Technical Design of the Second High Energy Dispersive Section at PITZ," in *European Workshop on Beam Diagnostics and Instrumentation for Particle Accelerators DIPAC*, no. MOPD26, (Basel, Switzerland), pp. 107–109, 2009. URL: http://accelconf.web.cern.ch/AccelConf/d09/papers/mopd26.pdf.

[168] G. Loisch *et al.*, "Photocathode laser based bunch shaping for high transformer ratio plasma wakefield acceleration," *Nucl. Instr. Methods Phys. Res. A*, vol. 909, pp. 107–110, 2018. DOI: https://doi.org/10.1016/j.nima.2018.02.043.

[169] D. C. Nguyen and B. E. Carlsten, "Amplified coherent emission from electron beams prebunched in a masked chicane," *Nucl. Instr. Methods Phys. Res. A*, vol. 375, pp. 597–601, 1996. DOI: https://doi.org/10.1016/0168-9002(95)01372-5.

[170] P. Muggli, V. Yakimenko, M. Babzien, E. Kallos, and K. P. Kusche, "Generation of Trains of Electron Microbunches with Adjustable Subpicosecond Spacing," *Phys. Rev. Lett.*, vol. 101, no. 054801, 2008. DOI: https://doi.org/10.1103/PhysRevLett.101.054801.

[171] P. Muggli *et al.*, "Excitation of Plasma Wakefields with Designer Bunch Trains," in *International Particle Accelerator Conference 2012*, (New Orleans, USA), pp. 2828–2830, 2012. URL: https://accelconf.web.cern.ch/accelconf/IPAC2012/papers/weppp051.pdf.

[172] R. J. England, J. B. Rosenzweig, G. Andonian, P. Musumeci, G. Travish, and R. Yoder, "Sextupole correction of the longitudinal transport of relativistic beams in dispersionless translating sections," *Phys. Rev. Spec. Top. Accel. Beams*, vol. 8, no. 012801, 2008. DOI: https://doi.org/10.1103/PhysRevSTAB.8.012801.

[173] R. J. England, J. B. Rosenzweig, and G. Travish, "Generation and Measurement of Relativistic Electron Bunches Characterized by a Linearly Ramped Current Profile," *Phys. Rev. Lett.*, vol. 100, no. 214802, 2008. DOI: https://doi.org/10.1103/PhysRevLett.100.214802.

[174] P. Piot, C. Behrens, C. Gerth, M. Dohlus, F. Lemery, D. Mihalcea, P. Stoltz, and M. Vogt, "Generation and Characterization of Electron Bunches with Ramped Current Profiles in a Dual-Frequency Superconducting Linear Accelerator," *Phys. Rev. Lett*, vol. 108, no. 034801, 2012. DOI: https://doi.org/10.1103/PhysRevLett.108.034801.

[175] L. Serafini and M. Ferrario, "Velocity bunching in photo-injectors," *AIP Conference Proceedings*, vol. 581, pp. 87–106, 2001. DOI: https://doi.org/10.1063/1.1401564.

[176] G. Andonian, S. Barber, F. H. O'Shea, M. Fedurin, K. Kusche, C. Swinson, and J. B. Rosenzweig, "Generation of Ramped Current Profiles in Relativistic Electron Bunches Using Wakefields in Dielectric Structures," *Phys. Rev. Lett*, vol. 118, no. 054802, 2017. DOI: https://doi.org/10.1103/PhysRevLett.118.054802.

[177] M. Cornacchia and P. Emma, "Transverse to longitudinal emittance exchange," *Phys. Rev. Spec. Top. Accel. Beams*, vol. 5, no. 084001, 2002. DOI: https://doi.org/10.1103/PhysRevSTAB.5.084001.

[178] P. Emma, Z. Huang, K.-J. Kim, and P. Piot, "Transverse-to-longitudinal emittance exchange to improve performance of high-gain free-electron lasers," *Phys. Rev. Spec. Top. Accel. Beams*, vol. 9, no. 100702, 2006. DOI: https://doi.org/10.1103/PhysRevSTAB.9.100702.

[179] Y.-E. Sun, P. Piot, A. H. Lumpkin, T. J. Maxwell, J. Ruan, and R. Thurmann-Keup, "Tunable Subpicosecond Electron-Bunch-Train Generation Using a Transverse-To-Longitudinal Phase-Space Exchange Technique," *Phys. Rev. Lett*, vol. 105, no. 234801, 2010. DOI: https://doi.org/10.1103/PhysRevLett.105.234801.

[180] P. Piot, Y.-E. Sun, J. G. Power, and M. Rihaoui, "Generation of relativistic electron bunches with arbitrary current distribution via transverse-to-longitudinal phase space exchange," *Phys. Rev. Spec. Top. Accel. Beams*, vol. 14, no. 022801, 2011. DOI: https://doi.org/10.1103/PhysRevSTAB.14.022801.

[181] G. Ha *et al.*, "Precision Control of the Electron Longitudinal Bunch Shape Using an Emittance-Exchange Beam Line," *Phys. Rev. Lett*, vol. 118, no. 104801, 2018. DOI: https://doi.org/10.1103/PhysRevLett.118.104801.

[182] D. Y. Shchegolkov and E. I. Simakov, "Design of an emittance exchanger for production of special shapes of the electron beam current," *Phys. Rev. Spec. Top. Accel. Beams*, vol. 17, no. 041301, 2014. DOI: https://doi.org/10.1103/PhysRevSTAB.17.041301.

[183] G. Ha, M. H. Cho, W. Gai, K.-J. Kim, W. Namkung, and J. G. Power, "Perturbation-minimized triangular bunch for high-transformer ratio using a double dogleg emittance exchange beam line," *Phys. Rev. Spec. Top. Accel. Beams*, vol. 19, no. 121301, 2016. DOI: https://doi.org/10.1103/PhysRevAccelBeams.19.121301.

[184] M. Boscolo, M. Ferrario, I. Boscolo, F. Castelli, and S. Cialdi, "Generation of short THz bunch trains in a RF photoinjector," *Nucl. Instr. Methods Phys. Res. A*, vol. 577, pp. 409–416, 2007. DOI: https://doi.org/10.1016/j.nima.2007.04.129.

[185] Y. Li and K.-J. Kim, "Nonrelativistic electron bunch train for coherently enhanced terahertz radiation sources," *Appl. Phys. Lett.*, vol. 92, no. 014101, 2008. DOI: https://doi.org/10.1063/1.2828337.

[186] G. Penco *et al.*, "Experimental Demonstration of Electron Longitudinal-Phase-Space Linearization by Shaping the Photoinjector Laser Pulse," *Phys. Rev. Lett*, vol. 112, no. 044801, 2014. DOI: https://doi.org/10.1103/PhysRevLett.112.044801.

[187] I. Šolc, "Birefringent Chain Filters," *J. Opt. Soc. Am.*, vol. 55, no. 6, pp. 621–625, 1965. DOI: https://doi.org/10.1364/JOSA.55.000621.

[188] J. C. Lagarias, J. A. Reeds, M. H. Wright, and P. E. Wright, "Convergence Properties of the Nelder-Mead Simplex Method in Low Dimensions," *Soc. Ind. Appl. Math. J. Optim.*, vol. 9, no. 1, pp. 112–147, 1998. DOI: https://doi.org/10.1137/S1052623496303470.

[189] P. Tomassini and A. R. Rossi, "Matching strategies for a plasma booster," *Plasma Phys. Control. Fusion*, vol. 58, no. 034001, 2016. DOI: https://doi.org/10.1088/0741-3335/58/3/034001.

[190] C. Mitchell, J. Qiang, and P. Emma, "Longitudinal pulse shaping for the suppression of coherent synchrotron radiation-induced emittance growth," *Phys. Rev. Spec. Top. Accel. Beams*, vol. 16, no. 060703, 2013. DOI: https://doi.org/10.1103/PhysRevSTAB.16.060703.

[191] I. Kuzmin *et al.*, "Shaping triangular picosecond laser pulses for electron photoinjectors," *Laser Phys. Lett.*, vol. 16, no. 015001, 2018. DOI: https://doi.org/10.1088/1612-202X/aaef95.

[192] D. L. Bruhwiler, D. A. Dimitrov, J. R. Cary, E. Esarey, W. Leemans, and R. E. Giacone, "Particle-in-cell simulations of tunneling ionization effects in plasma-based accelerators," *Phys. Plasmas*, vol. 10, no. 5, pp. 2022–2030, 2003. DOI: http://dx.doi.org/10.1063/1.1566027.

[193] G. Loisch *et al.*, "Jitter mitigation in low density discharge plasma cells for wakefield accelerators," *J. Appl. Phys.*, vol. 125, no. 063301, 2019. DOI: https://doi.org/10.1063/1.5068753.

[194] G. Loisch *et al.*, "Plasma density measurement by means of self-modulation of long electron bunches," *Plasma Phys. Control. Fusion*, vol. 61, no. 045012, 2019. DOI: https://doi.org/10.1088/1361-6587/ab04b9.

[195] J. Engel *et al.*, "Polymer foil windows for accelerator applications," *Nucl. Instr. Methods Phys. Res. A*, 2019. subm.

[196] Y. P. Raizer, *Gas Discharge Physics*. Berlin Heidelberg: Springer-Verlag, 1991. ISBN: 3-540-19462-2.

[197] B. M. Smirnov, *Theory of Gas Discharge Plasma*. Cham Heidelberg New York Dordrecht London: Springer-Verlag, 2015. ISBN: 978-3-319-11064-6, DOI: https://doi.org/10.1007/978-3-319-11065-3.

[198] J. D. Huba, *NRL Plasma Formulary*. Washington, DC, USA: Naval Research Laboratory, 2016.

[199] M. P. Anania *et al.*, "Plasma production for electron acceleration by resonant plasma wave," *Nucl. Instr. Methods Phys. Res. A*, vol. 829, pp. 254–259, 2016. DOI: http://dx.doi.org/10.1016/j.nima.2016.02.029.

[200] L. W. Nagel and D. O. Pederson, "Spice (simulation program with integrated circuit emphasis)," Tech. Rep. UCB/ERL M382, EECS Department, University of California, Berkeley, 1973. URL: http://www2.eecs.berkeley.edu/Pubs/TechRpts/1973/22871.html.

[201] J. Jacoby *et al.*, "Stopping of Heavy Ions in a Hydrogen Plasma," *Phys. Rev. Lett.*, vol. 74, no. 9, pp. 1550–1553, 1995. DOI: https://doi.org/10.1103/PhysRevLett.74.1550.

[202] O. Lishilin *et al.*, "First results of the plasma wakefield acceleration experiment at PITZ," *Nucl. Instr. Methods Phys. Res. A*, vol. 829, pp. 37–42, 2016. DOI: https://doi.org/10.1016/j.nima.2016.01.005.

[203] J. P. Jog, "Crystallization of Polyethyleneterephthalate," *J. Macromol. Sc. C: Polymer Rev.*, vol. 35, no. 3, pp. 531–553, 1995. DOI: https://doi.org/10.1080/15321799508014598.

[204] J. Christiansen and C. Schultheiss, "Production of high current particle beams by low pressure spark discharges," *Zeitschrift für Physik A Atoms and Nuclei*, vol. 290, no. 1, pp. 35–41, 1979. DOI: https://doi.org/10.1007/BF01408477.

[205] N. Lopes. Private communication, 2017. Instituto Superior Técnico, Lisbon, Portugal.

[206] D. Kind, M. Kurrat, and T. H. Kopp, "Voltage-time Characteristics of Air Gaps and Insulation Coordination — Survey of 100 Years Research —," in *33rd International Conference on Lightning Protection*, (Estoril, Portugal), 2016. URL: https://doi.org/10.1109/ICLP.2016.7791358.

[207] H. R. Griem, *Principles of Plasma Spectroscopy*. Maryland: McGraw-Hill Book Company, 1964. DOI: https://doi.org/10.1126/science.147.3655.284.

[208] H. R. Griem, *Spectral Line Broadening by Plasmas*. New York, USA and London, UK: Academic Press, 1974. ISBN: 0-12-302850-7.

[209] H. R. Griem, *Principles of Plasma Spectroscopy*. Cambridge, UK: Cambridge University Press, 1997. ISBN: 0 521 45504 9, DOI: https://doi.org/10.1017/CBO9780511524578.

[210] M. A. Gigosos, M. A. González, and V. Cardeñoso, "Computer simulated Balmer-alpha, -beta and -gamma Stark line profiles for non-equilibrium plasmas diagnostics," *Spectrochim. Acta Electr.*, vol. 58, pp. 1489–1504, 2003. DOI: https://doi.org/10.1016/S0584-8547(03)00097-1.

[211] V. Mazzacurati, P. Benassi, and G. Ruocco, "A new class of multiple dispersion grating spectrometers," *J. Phys. E: Sci. Instrum.*, vol. 21, pp. 798–804, 1988. DOI: https://doi.org/10.1088/0022-3735/21/8/012.

[212] O. Lishilin, *Study of self-modulation of an electron beam in plasma*. PhD thesis, University of Hamburg, 2018. URL: http://bib-pubdb1.desy.de/record/420545/.

[213] E. Gjonaj and T. Weiland, "Particle based PWFA simulations using a Discontinuous Galerkin approach," in *International Conference on Electromagnetics in Advanced Applications*, (Sydney, Australia), pp. 604–607, 2010. URL: https://doi.org/10.1109/ICEAA.2010.5652271.

[214] V. Wohlfarth, "PIC simulation of transverse instabilities in plasma wakefield acceleration at PITZ." Bachelor thesis, 2018. Humboldt-Universität zu Berlin.

[215] G. Loisch *et al.*, "Observation of High Transformer Ratio Plasma Wakefield Acceleration," *Phys. Rev. Lett.*, vol. 121, no. 064801, 2018. DOI: https://doi.org/10.1103/PhysRevLett.121.064801.

[216] A. Caldwell *et al.*, "Path to AWAKE: Evolution of the concept," *Nucl. Instr. Methods Phys. Res. A*, no. 829, pp. 3–16, 2016. DOI: http://dx.doi.org/10.1016/j.nima.2015.12.050.

[217] A. Aschikhin *et al.*, "The FLASHForward facility at DESY," *Nucl. Instr. Methods Phys. Res. A*, no. 806, pp. 175–183, 2016. DOI: http://dx.doi.org/10.1016/j.nima.2015.10.005.

[218] U. Dorda *et al.*, "SINBAD — The accelerator R&D facility under construction at DESY," *Nucl. Instr. Methods Phys. Res. A*, no. 829, pp. 233–236, 2016. DOI: http://dx.doi.org/10.1016/j.nima.2016.01.067.

[219] R. Brinkmann *et al.*, "Chirp Mitigation of Plasma-Accelerated Beams by a Modulated Plasma Density," *Phys. Rev. Lett.*, vol. 118, no. 214801, 2017. DOI: https://doi.org/10.1103/PhysRevLett.118.214801.

Acknowledgements

In the course of this work I have received help, support, teaching, friendship and assurance through numerous persons which I am deeply grateful for as I would like to express below in my native words.
Unter anderen möchte ich meinen Dank und meine Wertschätzung ausdrücken gegenüber

Dr. Frank Stephan, der mir die Möglichkeit gab den Studien zu meiner Dissertation bei PITZ nachzugehen, für sein Vertrauen und die fortwährende Unterstützung.

Prof. Dr. Florian Grüner, der die Betreuung meiner Dissertation an der Universität übernahm, für sein Interesse und die Unterstützung beim Abschluss dieser Arbeit.

Dr. Anne Oppelt, meiner Betreuerin bei PITZ, für ihre Unterstützung, Rat, Aufmunterung und Rückendeckung, die es mir erlaubt haben meine Arbeit zum erfolgreichen Abschluss zu bringen.

Dr. Reinhard Brinkmann dafür den Anstoß zu dieser Arbeit gegeben zu haben und für die Bereitschaft Mitglied der Prüfungskommission zu werden.

Prof. Dr. Sven-Olaf Moch und *Prof. Dr. Wolfgang Hillert*, für ihr Engagement als Teil der Prüfungskommission dieser Arbeit.

Dr. Holger Huck für die großartige Büroatmosphäre, die vielen interessanten Diskussionen und dafür viel von- und miteinander über Physik und Physiker gelernt zu haben.

Meinen Kollegen bei PITZ Dr. Osip Lishilin, Gaurav Pathak, Dr. Matthias Groß, Johannes Engel, Dr. Yves Renier, Sebastian Philipp, Dr. Galina Asova, Gerald Koss, Dr. Georgios Kourkafas, Dr. Dieter

Richter, Dr. Mikhail Krasilnikov, Lutz Jachmann, Winfried Koehler, James Good, Dr. Ye Chen, Prach Boonpornprasert, Dr. Christian Koschitzki, Raffael Niemczyk, Dr. Igor Isaev und einigen mehr, für alle Hilfe, Beratung und Kurzweil, die diese Arbeit ermöglicht und erleichtert haben.

Meinen Kollegen in Hamburg Dr. Alberto Martinez de la Ossa, Dr. Jens Osterhoff, Dr. Lucas Schaper, Dr. Timon Mehrling, für die großartige Unterstützung und geduldige Hilfe in allen Fragen der Plasmabeschleunigung und numerischen Simulationen.

Martin Hochberg und *Dr. Martin Sack*, die mir in allen Angelegenheiten der Pulsleistungselektronik bereitwillig mit Rat und Tat zur Seite standen.

Prof. Dr. Joachim Jacoby für die gute Vorbereitung auf die physikalische Realität.

Valentin Wohlfarth und *Paul Weidemann* für ihr Vertrauen in mich als Betreuer ihrer Abschlussarbeiten und für die Arbeit, die beide geleistet haben. Mein Dank gilt an dieser Stelle außerdem *Dr. Atoosa Meseck*, *Prof. Dr. Andreas Jankowiak* und *Dr. Friedhelm Heinrich*, die die Betreuung der Arbeiten von Seiten der Hochschulen verantworteten.

Den Menschen der Bundesrepublik Deutschland und andernorts, die es mir ermöglicht haben in Frieden und Freiheit mein Studium zu absolvieren.

Meiner Familie, allen voran meinen Eltern und meiner Schwester, für kontinuierliche Unterstützung und Verständnis.

Carmen für alles, insbesondere die kleinen Dinge.

Eidesstattliche Versicherung

Hiermit versichere ich an Eides statt, die vorliegende Dissertationsschrift selbst verfasst und keine anderen als die angegebenen Hilfsmittel und Quellen benutzt zu haben.
Die eingereichte schriftliche Fassung entspricht der auf dem elektronischen Speichermedium.
Die Dissertation wurde in der vorgelegten oder einer ähnlichen Form nicht schon einmal in einem früheren Promotionsverfahren angenommen oder als ungenügend beurteilt.

Hamburg, den 03.05.2019

Gregor Loisch